Experimental Investigations into Interactions and Collective Behavior in Protein/Polymer Mixtures and Granular Rods

A Dissertation

Presented to

The Faculty of the Graduate School of Arts and Sciences

Brandeis University

Department of Physics

Dr. Seth Fraden, Advisor

In Partial Fulfillment
of the Requirement for the Degree
Doctor of Philosophy

by

Joshua David Bloustine

May 2006

The signed version of this signature page is on file at the Graduate School of Arts and Sciences at Brandeis University.

This dissertation, directed and approved by Joshua David Bloustine's Committee, has been accepted and approved by the Faculty of Brandeis University in partial fulfillment of the requirement for the degree of:

DOCTOR OF PHILOSOPHY

Adam B. Jaffe, Dean of Arts and Sciences

Dissertation Committee:

Dr. Seth Fraden,Chair

Dr. Robert B. Meyer

Dr. Bulbul Chakraborty

Dr. Arshad Kudrolli, Department of Physics, Clark University

ACKNOWLEDGEMENTS

Many people have enabled me to pursue my graduate work at Brandeis. First among these is my thesis advisor Prof. Seth Fraden, who brought me into his laboratory despite my utter lack of experimental skills. His direction and knowledge were an invaluable part of my time at Brandeis. He always encouraged and supported my experimental work and excursions to conferences and schools which allowed me to experience a world of wonderful scientific ideas and scientists. I admire his keen ability to quickly identify problems and their solutions, his candor about my weaknesses, and especially his belief in and practice of open collaboration with other scientists which I cherish as a model for the scientific community.

I would like to express my gratitude to the current and former members of Seth's laboratory with whom I had the pleasure of working: First of all to Dr. E. Belamie who's rude introduction to an American university was teaching me the very basics of laboratory protocols; to Dr. S. Berejnov who helped tremendously with the work on chromatography and measuring protein phase diagrams; to N. Ribeck for his help on various granular rod projects; and to Dr. E. Grelet, Dr. K. R. Purdy, J-U Shim and F. Huang for teaching me many interesting aspects of liquid crystal and colloidal physics, microfluidics and for various interesting cultural discussions in and out of the laboratory.

I am also grateful to the staff of the physics department, especially Greg Widberg, who provided invaluable assistance.

I sincerely thank the members of my thesis committee: Prof. Robert B. Meyer, Prof. Bulbul Chakraborty, and Prof. Arshad Kudrolli. I would also like to thank the collaborators from whom I had the pleasure of learning: Prof. George M. Thurston in the Department of Physics at the Rochester Institute of Technology for all his help in understanding protein/polymer mixtures and general discussions about the

thermodynamics of mixtures; Prof. C. Miller for providing all the materials for the ClC-ec1 expression and purification which was carried out in his lab and Dr. A. Accardi and the other members of the Miller lab for their patience and assistance in teaching me to working with membrane proteins.

I wish to thank my wife, Rebecca Wolff, and my family members for their support. They have always backed me and I treasure their help. Even though my studies often seem mysterious to them, they encourage me and inquire about my work with genuine interest, the sign of wonderfully curious minds.

ABSTRACT

Experimental Investigations into Interactions and Collective Behavior in Protein/Polymer Mixtures and Granular Rods

A dissertation presented to the Faculty of the
Graduate School of Arts and Sciences of Brandeis
University, Waltham, Massachusetts

by Joshua David Bloustine

Interactions and collective behavior are studied for two examples of protein/polymer mixtures and for dynamic and static ensembles of granular rods. Interactions in protein solutions and protein/polymer mixtures are investigated by measuring virial coefficients. First, a method is presented for measuring virial coefficients using chromatography. After measuring virial coefficients in protein solutions, binary soluble protein/polymer mixtures are investigated. Virial coefficients and effective interactions in these mixtures are determined using light scattering techniques and the results are compared with purely entropic models for binary mixtures. Liquid-liquid phase transition temperatures (cloud points) are measured in these mixtures as a probe of their collective behavior and show that adding large molecular weight polymers raises the cloud point and adding small molecular weight polymers lowers the cloud point. The results from light scattering measurements and liquid-liquid phase transitions temperatures are subsequently compared showing that indeed the interactions determined by light scattering can qualitatively explain the collective behavior seen in the phase transition temperatures. It is also demonstrated that these data are consistent

with attractions between protein and polymer molecules. Interactions in mixtures of a membrane protein associated with detergent moieties and polymer are investigated using the same light scattering techniques as for the soluble protein/polymer mixtures in conditions where these membrane protein/detergent complexes crystallize in order to determine whether or not the crystallizing additive induced attractions between the protein/detergent complexes. It is shown that the addition of polymer to a dispersion of protein/detergent complexes causes these complexes to aggregate and crystallize but does not induce attractions between the individual complexes on the virial coefficient level. It is demonstrated that no phase transition of the detergent moieties occurs in the protein/detergent complex crystallization conditions.

The collective dynamic behavior of vortex formation and spontaneous vertical alignment in assemblies of granular rods is investigated by varying the rod aspect ratio and the rods' material properties. It is shown that vortex formation occurs only for rods with aspect ratio larger than three and that the minimum packing fraction needed for vertical alignment decreases with increasing rod aspect ratio. Vortex formation is observed for rods of different densities and electrostatic charges. Discrete vertical excitations, or taps, cause rods to spontaneously align vertically as does shaking, but tapping does not induce vortex formation. Finally, the the co-ordination number of granular rods is measured as a function of aspect ratio in order to probe the structure of static granular rod assemblies and test a statistical model for piles of granular rods. The co-ordination number increases as a function of increasing aspect ratio, but much more slowly than predicted for ellipsoids. In these same piles the collective behavior is quantified by measuring the volume fraction occupied by rods in a pile. The volume fraction and co-ordination number data are combined to show the validity of an excluded volume model for the behavior of piles of granular rods in the long rod limit.

This thesis is partially based on the following publications:

• J. Bloustine, S. Berejnov and S. Fraden. Measurements of Protein-Protein Interactions by Size Exclusion Chromatography. *Biophysical Journal* **85** (2003) 2619-2623

• J. Bloustine, T. Virmani, G.M. Thurston and S. Fraden. Light Scattering and Phase Behavior of Lysozyme-Poly(Ethylene Glycol) Mixtures. *Phys. Rev. Lett.* **96** (2006) 087803

• J. Bloustine, S. Fraden. Membrane protein CLC-ec1 does not fall into the crystallization slot *In preparation*

• J. Bloustine, S. Fraden. The contact number distribution of granular cylinders *In preparation*

Contents

List of Tables

List of Figures

Chapter 1

Introduction

In the Section 1.1, the theoretical background and models motivating and underlying the experiments in this thesis are presented. In Section 1.2 an outline of this thesis is provided.

1.1 Background

1.1.1 Virial Expansion

The equation of state relating pressure and density for any sufficiently dilute gas has a universal form, the Van't Hoff or ideal gas law: $p/k_BT = \rho$ where p is the pressure, $\rho = N/V$ is the number of molecules per unit volume, k_B is Boltzmann's constant and T is the absolute temperature. In analogy with dilute gases, the osmotic pressure (Π) of many sufficiently dilute liquid solutions may be written in the same form $\Pi/k_BT = \rho$ where now ρ is the density of a dissolved solute. At higher solute concentrations the osmotic pressure can be expanded in a power series in the solute density, known as a virial expansion:

$$\frac{\Pi}{k_BT} = \rho + \sum_{n\geq 2} B_n \rho^n \tag{1.1}$$

The coefficients B_n have units of [volume^{n-1}] and are known as virial coefficients. The term B_2 must be included when interactions between two solute molecules are appreciable. Similarly, the B_3 term arises from simultaneous interactions between three solute molecules. Although the term "virial" would appear to have a connection to infectious agents, in this context it does not. It was first used to describe this expansion of the equation of state by H. K. Onnes in 1901 [1, 2] who borrowed the term from the virial theorem in thermodynamics by Clausius.

The collective behavior of an ensemble of molecules is described by a virial expansion as shown by Eq.(1.1), but what is the relationship between the virial coefficients and molecular interactions? This relationship is found by calculating the classical partition function for a dilute solution. In order to calculate the second virial coefficient, a density expansion of the partition function is made. The coefficients in the expansion of the partition function are then related to the virial coefficients. Examples of different techniques for calculating the second virial coefficient are given by Hill [3] and Reif [4]. The resulting relation between intermolecular interactions and the second virial coefficient is:

$$B_2(T) = -\frac{1}{2}\int_V \left[exp\left(-w(\vec{r},T)\,/k_BT\right) - 1\right] d\vec{r} \tag{1.2}$$

where $w(\vec{r},T)$ is the reversible work needed to bring two solute molecules together from infinitely far apart to the distance $\vec{r}$ in the presence of solute molecules, which is known as the potential of mean force (PMF). The PMF, and therefore B_2, depends explicitly on temperature because of the effect of the solvent on solute interactions. In general, the integral in Eq.(1.2) depends on the separation between solute molecules as well as their relative orientations. If the PMF depends only on the separation

between a pair of molecules then:

$$B_2(T) = -\frac{1}{2}\int_0^\infty [exp(-w(r,T)/k_BT) - 1]dr \tag{1.3}$$

A natural scale for virial coefficients is provided by considering the hypothetical case of hard spheres in solution which cannot overlap but have no other interactions

$$w(r) = \infty \quad r < d \tag{1.4}$$

$$= 0 \quad r \geq d \tag{1.5}$$

where d is the diameter of one sphere. The second virial coefficient for hard spheres becomes:

$$B_2^{\mathrm{HS}} = \frac{16\pi(d/2)^3}{3} = 4\upsilon_o \tag{1.6}$$

where υ_o is the volume of one sphere. For realizable experimental situations $w(\vec{r})$ takes on positive and negative values. If $B_2 > B_2^{\mathrm{HS}}$ then the interactions are more repulsive than attractive and the converse is true for $B_2 < B_2^{\mathrm{HS}}$. The theta temperature T_Θ is the temperature for which $B_2(T_\Theta) = 0$.

The second virial coefficients of protein solutions, as probes of protein interactions, have generated a great deal of interest since George & Wilson [5] showed a correlation between protein crystallisability and the second virial coefficient. Their work demonstrated that many proteins crystallize in conditions where the second osmotic virial coefficient becomes slightly negative, indicating net attractive interactions between protein molecules. George & Wilson identified values of $-8 \times 10^{-4} \leq B_2 \leq -0.8 \times 10^{-4}$ mL mol g^{-2} as the crystallization slot where soluble proteins crystallize. For less negative or positive B_2 values in their study, proteins remained as monomers in solution. For more negative B_2 values, examples of precipitation were found.

A virial expansion may also be made of the excess Gibbs' free energy (G) of the solution over that of the pure solvent.

$$g = \frac{G}{Vk_BT} = \rho \ln \rho + B_2\rho^2 + B_3\rho^3 + \ldots \tag{1.7}$$

This expansion may be extended formally to a system with an arbitrary number of distinct dissolved solutes. The case of a two component solution is relevant for Chapters 3 and 4 of this thesis and is therefore treated explicitly here. The two independent solutes are labelled with subscripts 1 and 2

$$g = \frac{G}{Vk_BT} = \rho_1 \ln \rho_1 + \rho_2 \ln \rho_2 + B_{11}\rho_1^2 + 2B_{12}\rho_1\rho_2 + B_{22}\rho_2^2 + C_{111}\rho_1^3 + 3C_{112}\rho_1^2\rho_2 + 3C_{122}\rho_1\rho_2^2 + C_{222}\rho_2^3 + \ldots \tag{1.8}$$

In Eq.(1.8) $\rho_i = N_i/V$ [Volume^{-1}] is the number density of component i; B_{ij} [Volume] are the second virial coefficients and C_{ijk} [Volume^2] are the third virial coefficients. The first two terms in Eq.(1.8) represent the ideal entropy of mixing for each component. The terms quadratic in density represent corrections to the mixture's free energy arising from two particles interacting and the terms proportional to the third power of density describe corrections due to three particles interacting. In multicomponent solutions $w(r)$ is the potential of mean force between molecules of the same component for B_{ii} but between different components for B_{ij}. Also B_2 in Eq.(1.2) has been relabelled as B_{ii}.

The third virial coefficient is given by:

$$C_{ijk} = -\frac{1}{3V}\int\int\int_V (e^{-u(r_{ij})/k_BT}-1)(e^{-u(r_{ik})/k_BT}-1)(e^{-u(r_{jk})/k_BT}-1)d\vec{r}_i d\vec{r}_j d\vec{r}_k \tag{1.9}$$

The osmotic pressure (Π) is found from the free energy by $\Pi/k_BT = -\partial(G/k_BT)/\partial V$.

Leibowitz [6] solved the Percus-Yevick equation for the equation of state in

a binary hard sphere mixture. The virial coefficients for a bidisperse hard sphere mixture are obtained by expanding the equation of state solved by Lebowitz in a power series of the densities and identifying the expansioncoefficients, which yields:

$$B_{ij}^{\mathrm{HS}} = \frac{2\pi}{3}(r_i + r_j)^3 \quad ; \quad B_{ii}^{\mathrm{HS}} = (16\pi/3)r_i^3 \tag{1.10}$$

$$C_{iii}^{\mathrm{HS}} = \frac{5}{16}(B_{ii}^{\mathrm{HS}})^2 \ ; \ C_{iij}^{\mathrm{HS}} = \frac{8\pi^2}{27}r_i^3(r_i^3 + 6r_i^2 r_j + 15 r_i r_j^2 + 8r_j^3) \tag{1.11}$$

where r_i are the hard sphere radii. The conversion of virial coefficients from volume units to experimentally convenient units is given by:

$$B_{ij}[\mathrm{mL\ mol/g^2}] = B_{ij}[\mathrm{mL}]\frac{N_A}{M_i M_j} \tag{1.12}$$

$$C_{ijk}[\mathrm{mL^2 mol/g^3}] = C_{ijk}[\mathrm{mL^2}]\frac{N_A^2}{M_i M_j M_k} \tag{1.13}$$

where $M_i[\mathrm{g\ mol^{-1}}]$ are the solute molecular weights and $N_A[\#\ \mathrm{mol^{-1}}]$ is Avogadro's number.

1.1.2 Depletion Attraction

The addition of small polymers to a dispersion of large colloids can result in precipitation or crystallization of the colloids. Even when the sole colloid/polymer interaction is steric repulsion, an attraction between a pair of colloids is generated by the exclusion of polymer molecules from the region between the colloids. If the polymer concentration is assumed to be larger than the colloid concentration and the polymers are considered to be effectively spherical particles, then the mixture's entropy is dominated by the polymers' entropy. The volume accessible to the polymers' centers of mass is greater if the average distance between the colloids' centers of mass is less than one polymer diameter than if the colloids are separated by distances greater than one polymer diameter. Therefore the entropy increases and the free energy is lowered

if the colloids come together. This entropic effect is known as depletion attraction [7, 8]. To model the depletion attraction Asakura & Oosawa [7] considered adding ideal polymers, or other macromolecules, to a dispersion of spherical colloidal particles. They noted that when two particles approach each other closely, then polymer molecules are excluded from a region near the surface of each particle. This region depleted of polymer has a lower osmotic pressure than the surrounding fluid with polymers. This osmotic pressure difference creates an attractive potential $u(r)$ between the particles, where r is the distance between particles. This attraction has the range $D \leq r \leq D + d$ where D is the colloid diameter and d is the polymer diameter. In the limit where the colloid is much larger than the polymer ($\beta = D/d \gg 1$) the depletion attraction simplifies to $u(r/D)/k_BT = -3/2\beta\phi(r/D)^2$ where ϕ is the polymer volume fraction and $0 \leq x \leq 1$ is the reduced inter-colloid distance. The strength of the attraction, as measured by the minimum value of $u(r)$, is linearly proportional to the polymer density. Gast *et al.* [8] and Hall & Mahadevan [9] employed Asakura & Oosawa's model to calculate the phase diagrams of colloid/polymer mixtures in the limit where the colloid is much larger than the polymer.

Meijer & Frenkel [10] and Eisenriegler *et al.* [11] extended this ideal polymer model of the depletion attraction to account for cases when the polymer is larger than the colloid. In that case polymer molecules can wrap partially around colloid particles thereby reducing the polymer/colloid excluded volume. This effect can be accounted for in the framework of an Asakura-Oosawa depletion theory by defining an ideal effective polymer radius (r_{eff}) which is smaller than the polymer's radius of gyration r_g and allowing the effective polymer radius to vary with the ratio of colloid to polymer size. Eisenriegler *et al.* found a closed formula for relating the effective sphere size (r_{eff}) to the protein (r_{pro}) and polymer (r_g) sizes (see Fig.6 of ref. [11]):

$$y = -x + \frac{x^{1/3}(3\sqrt{\pi} + 6x + x^2\sqrt{\pi})^{1/3}}{\pi^{1/6}} \tag{1.14}$$

Here $x = r_{\rm pro}/r_g$ and $y = r_{\rm eff}/r_g$. The case where the polymer molecules are much larger than the particles ($r \ll r_g$), has been referred to as the protein limit [12]. Tuinier *et al.* [12] used computer simulations to calculate the polymer concentration profile around colloids as a function of the colloid to polymer size ratio. They calculated effective colloid second virial coefficients and found that adding polymers induces an effective attraction only when $r > r_g$ but that adding polymers never induces repulsion between the colloids. Additionally, they compared their results to the Asakura-Oosawa model and found significant differences, especially when the colloid and polymer sizes are comparable, $r \sim r_g$. Most notably Tuinier *et al.* found that the Asakura-Oosawa model severely overestimates the attraction induced between colloids when $r \sim r_g$. Annunziata *et al.* [13] used scaled particle theories to calculate the free volume available to idea polymers in protein/polymer mixtures. Their procedure leads to the same results for the variation of the spinodal temperature with polymer concentration as found by using the effective polymer size, Eq.(1.14), as discussed in Section 3.2.2.

All the above mentioned models treat ideal, non-interacting polymers. These models are expected to be valid for polymers near their theta point but to be invalid for self-avoiding polymers. The protein/polymer mixtures dealt with in Chapters 3 and 4 are composed of self-avoiding polymers. Recently, progress has been made in predicting phase diagrams of colloid/polymer mixtures where the polymers self-avoid. Bolhuis *et al.* [14] calculated phase diagrams of colloid/polymer mixtures with computer simulations of self-avoiding polymers. Their results show that polymer interactions are more important when the polymer is larger than the colloid.

1.1.3 The Random Contact Model

Philipse [15] performed pioneering experiments on piles composed of elongated grains, granular rods. He found that the volume fraction occupied by rods depends inversely

on the rod aspect ratio. In order to model that data, he made a statistical model to describe piles of granular rods, which he termed the random contact model (RCM). The RCM predicts a relationship between ϕ, $\langle z \rangle$ and the ratio of the excluded volume between particles to the volume of a single particle, $V_{\rm ex}/V_{\rm p}$:

$$\phi(V_{\rm ex}/V_{\rm p}) = \langle z \rangle \tag{1.15}$$

Onsager [16] calculated the excluded volume between two right cylinders (rc) averaged over all possible mutual orientations for an isotropic orientational distribution of cylinders: $V_{\rm ex}^{\rm rc} = (\pi D/2)[L^2 + (\pi + 3/2)LD + \pi D^2/4]$ and therefore: $(V_{\rm ex}/V_{\rm p})^{\rm rc} = 2\pi + 3 + 2(L/D) + (\pi/2)D/L$. The ratio of excluded volume to particle volume in the limit of long rods ($L/D \gg 1$) is $(V_{\rm ex}/V_{\rm p})^{\rm rods} \sim 2L/D$ and in the limit of thin discs ($L/D \ll 1$) this ratio becomes $(V_{\rm ex}/V_{\rm p})^{\rm discs} \sim (\pi/2)D/L$. Therefore, the RCM predicts $\phi(L/D) = \langle z \rangle/2$ for long rods and $\phi(D/L) = 2\langle z \rangle/\pi$ for thin discs. In order to quantitatively test the predictions of the RCM, ϕ, $\langle z \rangle$ and L/D must be measured independently for a given granular pile.

1.2 Outline

The goal of this thesis is to enhance understanding of how interparticle interactions are related to collective behavior in protein/polymer mixtures and in granular rod systems.

In Chapters 2, 3 and 4 protein solutions and protein/polymer mixtures in thermodynamic equilibrium are investigated using chromatography and light scattering to measure virial coefficients and microscopy to look for phase transitions. In Chapters 5 and 6 interactions and collective behavior are investigated for non-equilibrium systems of granular rods.

Chapter 2 describes a novel chromatographic technique for measuring second

virial coefficients using size exclusion chromatography. This technique is implemented using pulse chromatography and commercially available chromatography instrumentation which makes it accessible to any laboratory equipped with chromatography instrumentation. This method also significantly reduces the time and amount of material needed to carry out virial coefficient measurements from the initial implementation. The efficacy of this technique is demonstrated by comparison of measurements of virial coefficients for the proteins lysozyme and bovine serum albumin (BSA) in various solution conditions to previous measurements using established light scattering and chromatography techniques.

In Chapter 3 further investigations into lysozyme interactions are made in lysozyme/polymer mixtures. Chapter 3 evaluates whether or not the water soluble polymer poly(ethylene glycol) (PEG) induces attraction between lysozyme molecules by the depletion mechanism. Light scattering measurements are used to quantify the protein/protein and protein/polymer interactions in lysozyme/PEG mixtures. The collective behavior of these mixtures is investigated by measurements of liquid-liquid phase transition temperatures, cloud points, in these mixtures.

Chapter 4 continues the investigations into the relation between protein/polymer interactions and the collective behavior of protein/polymer mixtures for mixtures of a membrane protein and PEG. A chloride channel integral membrane protein was expressed and purified in order to carry out these studies. Light scattering is used to quantify the interaction between proteins in solution and the effect of adding PEG. Since membrane proteins are soluble only in the presence of detergents, the detergent interactions are investigated.

In the final two chapters of this thesis, driven and static assemblies of granular rods are studied. These granular assemblies are far from thermodynamic equilibrium and so differ markedly from protein and polymer solutions in thermodynamic equilibrium. The same questions asked in Chapters 2-4 about macromolecular systems

are also posed in the context of granular rod assemblies: how do interparticle interactions effect the assembly's collective behavior and can a statistical description of the assembly be made which connects the interparticle interactions and the collective behavior.

In Chapter 5 the effect of varying interactions between granular rods on their collective dynamic behavior is investigated by examining how dynamic vortex formation is effected by changing the rod aspect ratio and the material properties of the rods. It is shown that the formation of dynamic vortices depends significantly on the rod aspect ratio but not on the specific material properties of the rods indicating that geometric factors change rod/rod interactions and therefore, their collective behavior.

Chapter 6 studies the interactions between granular rods in static piles by measuring the co-ordination number of granular rods as a function of the rod aspect ratio. The collective behavior of rods in these piles is also investigated by measuring how the density in these piles depends on the rod interactions as determined by the rod aspect ratio. The validity of the RCM to describe granular rod piles is tested.

An appendix detailing the protocols used to express and purify the membrane protein CLC-ec1 used in Chapter 4 is included.

Chapter 2

Measuring Protein/Protein Interactions with Chromatography

2.1 Introduction

The most prevalent experimental procedure for measuring B_2 is light scattering. Measuring B_2 with light scattering is accurate and fairly efficient but requires a specialized instrument not available to many biochemical researchers interested in measuring second virial coefficients of protein solutions. Additionally, sedimentation equilibrium [17], osmometry [18], neutron [19] and x-ray scattering [20], and self-interaction chromatography [21] have been employed to measure B_2.

Osmometry requires equipment which is not commercially available and longer than one day to measure B_2 [22]. X-ray and neutron scattering both require precious time on specialized beam lines which is not readily available. In separate studies we found that sedimentation equilibrium studies using an analytical centrifuge yield virial coefficient values which depend sensitively on the non-linear fitting parameters used to fit the equilibrium concentration profile. This makes the sedimentation equilibrium mode of analytical ultracentrifugation unreliable for virial coefficient measurements.

Chromatographic separations are used on a daily basis in biochemical separations and purifications. Therefore, a chromatographic method to measure virial coefficients would enable further studies of B_2. Tessier *et al.* [21] developed a method to measure second virial coefficients with self-interaction chromatography (SIC). The SIC technique involves immobilizing the solute molecule of interest on a chromatographic column and then flowing the same solute molecule through the column. Qualitatively, if the solute-solute interactions are more attractive than repulsive, the solutes spend a longer time in the column. We attempted to implement the SIC technique and found that it suffers from a number of technical problems. In order to quantitatively measure virial coefficients, the density of protein bound to the column must be known. In practice, measuring this concentration is difficult and unreliable. We found that protein retention on a column with protein bound depends on many experimental parameters including the injection volume which made quantitating virial coefficients difficult. Since SIC requires protein to be bound on a column it also suffers from the disadvantage that the binding could effect the interaction with free proteins in solution. Due to these technical difficulties with implementing SIC, we set out to look for another efficient chromatographic technique to measure virial coefficients of protein solutions.

In investigating chromatographic techniques we found that Winzor and coworkers [23] developed a method for measuring B_2 using size exclusion liquid chromatography (SEC) which is also known as gel filtration chromatography. In SEC the solute retention time on the column depends sensitively on the solute's size, although no universal calibration for SEC has yet been achieved because solute retention also depends on the nature of the porous beads in the column. In SEC thermodynamic non-ideality leads to concentration dependent retention times, which can be utilized to quantify the second osmotic virial coefficient, B_2.

Nichol *et al.* [23] showed the possibility of measuring B_2 with frontal elu-

tion liquid chromatography. Frontal elution chromatography involves saturating a chromatographic column with a given solute while measuring the profile of the concentration when saturating the column and when the saturated region flows out of the column. Although frontal chromatography [24] allows one to fix the solute concentration in the column directly, it requires a large amount of protein ($\sim 0.5\,g$) and long experiment times (about three hours per column run). In this chapter Nichol *et al.*'s method is extended to pulse size exclusion high pressure liquid chromatography (HPLC), where a small amount of protein is injected into and subsequently flows down the column. This adaptation drastically reduces the amount of protein ($< 25\,\mathrm{mg}$) and time needed (about 15 minutes per column run) to measure B_2 by SEC. Our results for B_2 obtained with size exclusion chromatography agree well with those from frontal chromatography and from light scattering measurements. It is also demonstrated that SEC can track the evolution of B_2 from positive to negative values.

2.2 Theory

SEC is used to separate and identify solutes of different sizes from a mixture. In SEC a solution is flowed through a chromatographic column made up of porous beads [25, 26]. Solute molecules are advected by the flow in the regions between the beads (inter-pore volume or mobile phase volume) and diffuse into the beads. Inside the porous beads (pore volume or stationary phase volume), there is virtually no flow. The beads have a distribution of pores of various sizes. A scanning electron micrograph of beads used for SEC, taken from ref. [27], is shown in Fig. 2.2. Solute molecules larger than the largest pore are unable to penetrate the porous beads and flow through the inter-pore volume. These largest molecules are said to be completely excluded by the column, hence the nomenclature size exclusion chromatography. Solute molecules

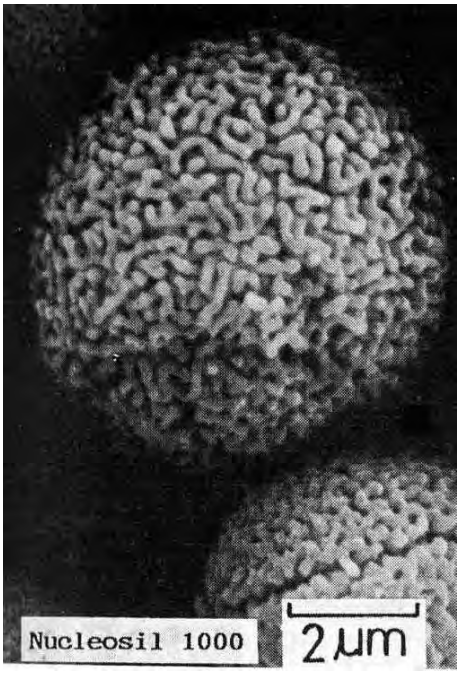

Figure 2.1: A scanning electron micrograph of porous silica beads used for size exclusion chromatography is shown. This micrograph was taken from ref.[27]

smaller than the smallest pore are able to penetrate into every pore and are said to be completely included by the column. Intermediate sized solute molecules penetrate a fraction of the pores depending on their size. Assuming that all solutes have the same energetic interactions with the porous medium, which is not always the case, then the time a solute molecule spends in the pore before diffusing back to the inter-pore volume depends on the volume accessible to the solute molecule inside the pore. Smaller molecules can access a larger volume and so will stay longer in the pores on average. Therefore, larger molecules will pass through the chromatographic column before smaller molecules.

In chromatography, solute passage through a given column is quantified in volume units. In practice, each given column has a useful range of sizes that can be separated using that column. That range of sizes is given by a calibration curve for a given column which plots the retention volume as a function of solute size, or typically solute molecular weight. A calibration curve for poly(ethylene glycol)

(PEG) dissolved in water eluting through the YMC column described in Section 2.3 is shown in Fig.2.3.2.

Nichol *et al.*'s [23]'s model of solute retention in SEC, describing how B_2 is measured with SEC, is discussed below. We assume a balance of the solute, i.e. protein, chemical potentials (μ_p and μ_i) between the stationary and mobile phases as the solute is transported through the column. The pore volume (i.e. stationary phase) is labelled with the subscript p, and the inter-pore volume (i.e. mobile phase) with the subscript i. Equilibrium requires $\mu_p = \mu_i$. We write these chemical potentials by including the standard part μ^o, the ideal term, and a term accounting for thermodynamic non-ideality through the activity coefficient γ:

$$\begin{aligned} \mu_p &= \mu_p^o + RT\ \ln(C_p\ \gamma_p(C_p)) \\ \mu_i &= \mu_i^o + RT\ \ln(C_i\ \gamma_i(C_i)) \end{aligned}$$

where $C_{i,p}$ are the local solute weight concentrations, R is the universal gas constant and $\gamma_p(C_p)$, $\gamma_i(C_i)$ are the thermodynamic activity coefficients of solute molecules in the pore and inter-pore volumes respectively. Rearrangement of these equations yields:

$$\begin{aligned} \ln(K_0) &= \frac{\mu_i^o - \mu_p^o}{RT} \\ \ln\left(\frac{\gamma_i}{\gamma_p}\right) &= \ln\left(\frac{C_p}{C_i}\right) - \ln(K_0) \end{aligned} \tag{2.1}$$

where K_0 is the partition coefficient of solute molecules between chromatographic phases in the limit of infinite dilution. The relation between weight concentration, C, and number density, ρ, is $\rho = C\frac{N_A}{M_w}$ where N_A is Avogadro's number and M_w is the solute molecular mass. Nichol *et al.* [23] made a virial expansion of the activity

coefficients

$$\ln \gamma(z) = 2B_2(N_A/M_w)C + \ldots \tag{2.2}$$

This consideration assumes no difference in the solute-solute interactions in the mobile and stationary phases. The local solute distribution coefficient is $K_D \equiv \frac{C_p}{C_i}$. If K_D is independent of concentration, as is the case for pulse chromatography with $B_2 = 0$, or if the concentration is constant as in frontal elution chromatography, then [23, 25]

$$K_D \equiv \frac{C_p}{C_i} = \frac{t_r - t_o}{t_T - t_o} = \frac{V_r - V_o}{V_T - V_o} \tag{2.3}$$

where t_r and V_r are the solute retention time and volume, t_0 and V_0 are the retention time and volume of completely excluded molecules (i.e. the "dead" volume), and t_T and V_T the retention time and volume of completely included molecules (i.e. the "total" volume). Inserting the definition of K_D(Eq. 2.3) and Eq. 2.2 into Eq. 2.1 and keeping only the first order terms in concentration one obtains a relation between K_D, B_2, and C_i valid for frontal chromatography where the concentration C_i is the plateau value of the solute concentration in the mobile phase:

$$\ln\left(\frac{K_D}{K_0}\right) = 2B_2\frac{N_A}{M_w}C_i(1 - K_D) \tag{2.4}$$

To adapt this to pulse chromatography we replace the plateau value with the average concentration $< C_i >$ of the mobile phase in the pulse:

$$\ln\left(\frac{K_D}{K_0}\right) = 2B_2\frac{N_A}{M_w} < C_i > (1 - K_D) \tag{2.5}$$

Since $< C_i >$ is not directly accessible in a HPLC experiment, it must be related to measurable parameters. The solute concentration passing through the

outlet of the column is measured as a function of volume. Each solute species passing the column appears in the detector as a peak in the concentration as function of volume curve. The mass of solute molecules in the pulse, or migration zone, (m_{zone}) is determined by integrating the concentration as a function of time over the zone volume, i.e. the peak (V_z). For columns in which there is no irreversible binding of protein molecules to the column, all the injected molecules are accounted for by integrating the peak. Therefore the total injected mass is the same as the total mass in the zone, $m_{\text{inj}} = C_{\text{inj}}V_{\text{inj}} = m_{\text{zone}}$, but the concentration of solute in the migration zone is much lower than the injected concentration because the pulse spreads as it is injected into the column. The condition for the conservation of mass of solute molecules in the migration zone (subscript z) is

$$m_i + m_p = m_{\text{inj}} \tag{2.6}$$
$$< C_i > V_i + < C_p > V_p = C_{\text{inj}}V_{\text{inj}} = m_{\text{inj}}$$

Here V_i and V_p are the mobile (inter-pore) and stationary (pore) portions of the zone volume V_z, with

$$V_p = (V_T - V_0)\frac{V_z}{V_T} \quad , V_i = (V_0)\frac{V_z}{V_T} \tag{2.7}$$

We measure the solute zone volume V_z from the full width Δt at half-maximum of the chromatogram peak using $V_z = \nu\Delta t$, where ν is the flow rate. After substituting the definition of the partition coefficient given in Eq. 2.3 and definitions Eq. 2.7 into Eq. 2.6, one obtains:

$$< C_i >= \frac{m_{\text{inj}}}{V_z(\frac{V_R}{V_T})} \tag{2.8}$$

In Eq. 2.8, the numerator is the total mass in the zone and the denominator is the volume of the zone accessible to the protein. Thus, the concentration $< C_i >$ is the

ratio of these terms. In this derivation we have assumed Eq. 2.3 holds, which is no longer the case when both $B_2 \neq 0$ and the concentration is changing during transport down the column. However, as we will show below, the changes in K_D with concentration are small, which may justify our approximation. Eq.(2.8) allows us to extend the method of ref. [23], originally developed using frontal elution chromatography, to pulse HPLC. Alternatively, one could use the maximum concentration $C_{\max}$ of eluted solute instead of $< C_i >$ in Eq. 2.5. As shown in Fig. 2.3 $C_{\max}$ and $< C_i >$ are approximately equal. Our procedure is then to inject different volumes of samples at various concentrations, measure K_D from the retention times as given in Eq. 2.3 and then plot $\ln K_D$ as a function of either $< C_i > (1 - K_D)$ or $C_{\max}(1 - K_D)$. The slope of that plot is then $2\, B_2\, N_A / M_w$ from which B_2 is extracted given the solute molecular weight M_w.

2.3 Materials & Methods

2.3.1 Materials

We obtained six times recrystallized, hen egg white lysozyme from Seikagaku America and bovine serum albumin (BSA), from Sigma. Both were used without further purification. All buffer components were obtained from Fisher Scientific. A Millipore Elix system purified water for all the experiments. We prepared potassium phosphate buffers by mixing 50mM solutions of K_2HPO_4 and KH_2PO_4, at various NaCl concentrations to adjust the ionic strength, to reach pH = 6.2 as measured by an Orion SA520 pH meter. The pH = 4.7 of sodium acetate buffers was adjusted by adding concentrated acetic acid to solutions of sodium acetate and NaCl. Additionally all buffers were passed through 0.45 μm nylon filters, also obtained from Millipore, prior to use. Protein concentrations were measured using a Varian instruments Cary 50Bio spectrophotometer at a wavelength of 278 nm. The extinction coefficient used for

lysozyme was $\epsilon_{278\text{nm}} = 2.64$ mL $(\text{mg}\,\text{cm})^{-1}$, and $\epsilon_{278\text{nm}} = .667$ mL $(\text{mg cm})^{-1}$ for BSA.

2.3.2 Chromatography

An 1100 series HPLC system from Agilent Technologies (Wilmington, DE) was used for all chromatographic measurements. Protein retention times were determined using an Agilent differential refractive index detector (RID) and an Agilent diode-array-detector (DAD) by absorbance at 278nm. A TSK-G2000SW (30cm x 0.75cm I.D.) column from TosoBiosep and a YMC-Diol-200AMP (30cm x 0.60cm I.D.) column from YMC were used in the chromatographic measurements. We used a flow rate of 1 mL/min for all measurements. These columns contain a packing of porous silica beads whose surfaces have been made hydrophilic. The manufacturers specified the diameter of a single bead to be 5μm for both columns. The average pore diameter is 125 Å for the TSK-G2000SW, and 200 Å for the YMC-Diol-200AMP. We determined the SEC calibration curve for these columns, as shown in Fig. 2.3.2, by using poly-ethylene-glycol (PEG) samples with molecular weights $200 \leq M_w \leq 10^5$ g/mol, obtained from Sigma and Fluka. For every run the eluent was the same as the sample buffer. The random run-to-run difference in retention times for our system was less than 0.1%. Any dependence of the dimensionless distribution coefficient K_D for protein molecules between the stationary and mobile phases on the average flow rate ν would indicate non-equilibrium effects. We found K_D to be independent of flow rate for the experimentally accessible values: $0.1\,\text{mL/min} \leq \nu \leq 1.3\,\text{mL/min}$. Additionally, stop flow experiments have shown that solute retention in SEC is unaffected if the flow is stopped for prolonged periods [26]. We therefore conclude that the solute molecules are in a thermodynamically equilibrated state as they flow through the chromatographic column.

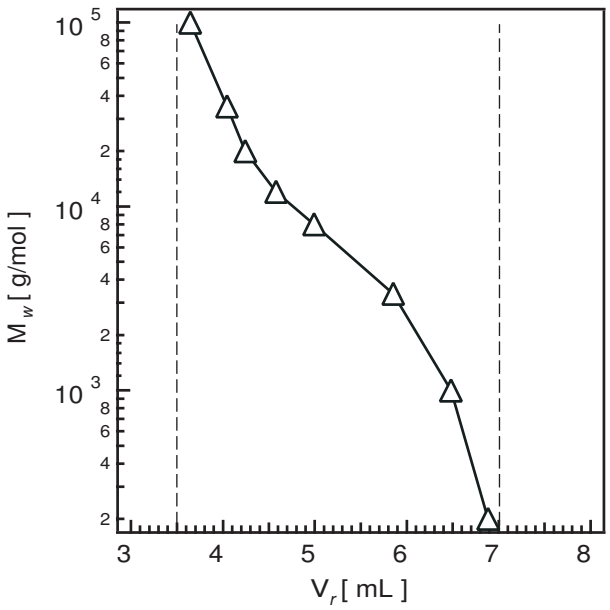

Figure 2.2: The calibration curve for PEG dissolved in water in the YMC Diol 200 column. The retention volume V_r is shown as versus the PEG molecular weight M_w. The dashed lines indicate the dead volume and the total volume.

2.3.3 Methods

For each solvent condition we performed a series of HPLC experiments varying solute (protein) injected concentration C_{inj} and using two injection volumes, $V_{\text{inj}} = 20\,\mu\text{L}$ and $100\,\mu\text{L}$. We identify the protein retention time t_r as the time of the maximum in the protein concentration as a function of time chromatogram (2.3), where the injection time is $t = 0$. We plot t_r as a function of C_{inj}, and find that t_r depends on V_{inj} as shown in Fig. 2.4. In order to apply our modification of Nichol *et al.*'s method to HPLC, we recalculate the average solute concentration in the pulse, $< C_i >$, according to Eq. 2.8, and find that this reassuringly collapses the multiple t_r vs. C_{inj} curves from Fig. 2.4 to a single curve as shown in the insert of Fig. 2.5. The slope of this collapsed curve is proportional to the second virial coefficient according to Eq. 2.4.

In order to calculate K_D according to Eq. 2.3 we must measure the total (t_T) and dead (t_0) times. We have measured the total time for each run using the solvent

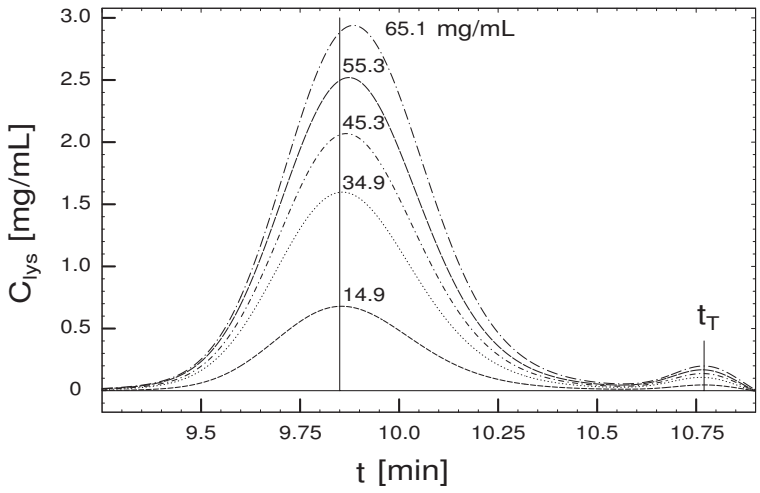

Figure 2.3: Lysozyme chromatograms for $V_{\rm inj} = 20\mu$L and different injected concentrations ($C_{\rm inj}$) as indicated next to each curve. The average concentrations $< C_i >$ used in the analysis in Fig. 2.5 are dash - 0.74 mg/mL, points - 1.72 mg/mL, dash and points - 2.20 mg/mL, long dash - 2.68 mg/mL, long dash and points - 3.08 mg/mL. The vertical line marks the retention time for the most dilute sample (not shown). The retention time t_r is the time corresponding to the peak of the concentration profile ($C_{\rm max}$) and increases with increasing concentration. The retention time of completely included molecules (the "total" volume) is marked as t_T. The peak at t_T is caused by the very small refractive index difference between the eluent and the solution buffer. The retention time of completed excluded molecules (the "dead" volume) was $t_0 = 6.07$ min (not shown in figure). Note that $C_{\rm max}$ and $< C_i >$ are similar. The buffer is Sodium Acetate, 50mM, pH 4.7.

peak (these are maximums of the second peaks (t_T) in Fig. 2.3). In order to measure the dead time, we used PEG with a molecular weight of 10^5 g/mol, which is totally excluded from the TSK and the YMC columns. We have measured the dead times for all solvent conditions and injection volumes. It is important to measure t_T and t_0 separately for all injection volumes to avoid any instrumental errors associated with precisely identifying the injection time.

Light scattering measurements were performed to determine B_2 independently for conditions where results were not found in the literature. Details concerning light scattering measurements are given in Section 3.3.

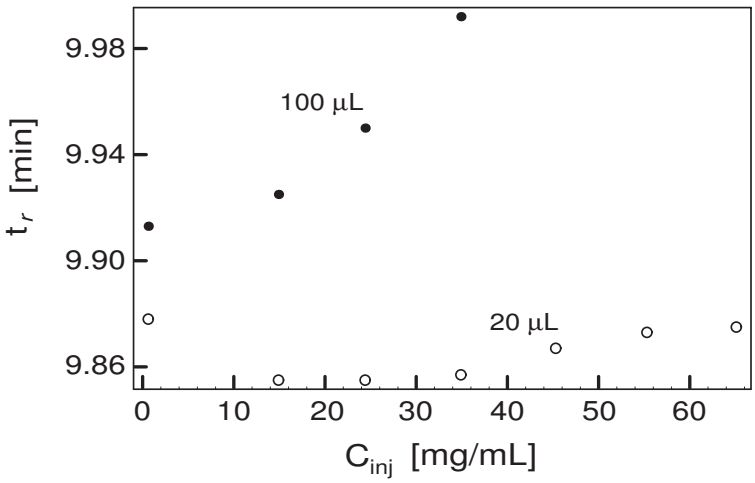

Figure 2.4: Lysozyme retention times are plotted versus injected concentrations for two injection volumes. Open circles: $V_{\mathrm{inj}} = 20\mu$L and filled circles: $V_{\mathrm{inj}} = 100\mu$L. Buffer : Sodium Acetate 50 mM pH 4.7.

2.4 Results

We measured the dependance of the retention factor K_D on C_{inj} and V_{inj} for lysozyme and BSA in the above mentioned buffers and columns. These buffer conditions were chosen to investigate the cross-over from positive to negative B_2 values and to compare with data available in the literature.

Fig. 2.3 shows the RID signal measuring the concentration of the eluted protein versus time for representative lysozyme chromatograms with $V_{\mathrm{inj}} = 20\,\mu$L. One can see the retention time increase with increasing protein concentration, while t_T remains constant.

In SEC the direction of the shift in the retention time with concentration depends on the sign of B_2. For conditions where $B_2 > 0$, t_r increases with increasing protein concentration and where $B_2 < 0$, t_r decreases with increasing concentration. If $B_2 = 0$, t_r is independent of concentration. Previous studies [19, 28, 29, 30] have shown that the sign of B_2 for protein solutions depends on the ionic strength of the solution.

Fig. 2.4 shows the dependence of lysozyme retention times on the injected

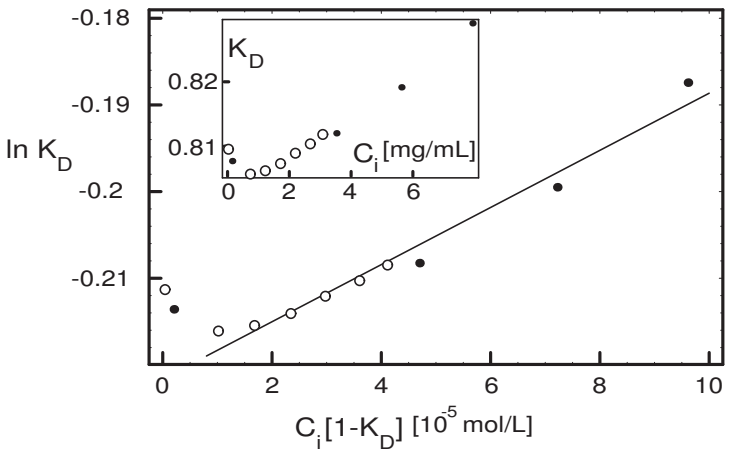

Figure 2.5: $\ln K_D$ vs. $< C_i > (1 - K_D)$(mg/mL) for lysozyme as in Eq. 2.4. The insert is a plot of K_D vs. $< C_i >$(mg/mL), where multiple curves from Fig. 2.4 with different injected volumes collapse after recalculating the solute concentration in the mobile phase of the migration zone as in Eq. 2.8. Buffer: Sodium Acetate 50 mM pH 4.7, black dots: $V_{\rm inj} = 100\mu$L, open circles: $V_{\rm inj} = 20\mu$L.

concentration $C_{\rm inj}$. The two sets of data correspond to different injection volumes ($V_{\rm inj}$): 20 μL and 100 μL. Following the procedure introduced above for determining the average solute concentration in the mobile phase of the migration zone $< C_i >$, we plot the dimensionless retention parameter, K_D, versus $< C_i >$ in the insert of Fig. 2.5. This procedure collapses the data from Fig. 2.4 onto a single curve from which $V_{\rm inj}$ has been removed as an independent parameter. At the smallest concentrations in the insert of Fig. 2.5, some non-linear dependence of K_D on $< C_i >$ can be observed. We attribute this behavior to errors introduced at the smallest signal to noise ratios. We have not included these points in our fits.

In order to extract B_2 from chromatographic data, $< C_i >$ is calculated by Eq. 2.8 and then $\ln K_D$ versus $< C_i > (1 - K_D)$ is plotted. As discussed in Section 2.2 the slope of the linear fit in Fig. 2.5 is proportional to B_2. Our results for B_2 for lysozyme solutions are listed in Table 2.1.

The protein concentration range typically used to measure B_2 by light scattering is approximately $0 < C_i < 30$ mg/mL [19, 28]. In our SEC measurements the protein concentrations $< C_i >$ eluting from the column, correspond to precisely

	B_2 [10^{-4} mL mol g^{-2}]	
NaCl (mM)	From SEC	From LS
0	2.4	1.8
50	1.6	-
150	-1.0	-1.4

Table 2.1: Comparison of size exclusion chromatography (SEC) and static light scattering measurements of the second virial coefficients B_2 [10^{-4} mL mol g^{-2}] for lysozyme in Potassium Phosphate Buffer 50 mM, pH=6.2, at various added NaCl concentrations.

the same range, although the injected concentrations are much higher as shown in Fig. 2.4. Even with these injected concentrations, the column was never saturated. Such high injected concentrations may not be accessible for other protein systems, and may be avoided by employing larger injection volumes, as shown by the $V_{inj} = 100\mu$L data in Fig. 2.4.

Fig. 2.6 compares our B_2 results for BSA from pulse SEC and those obtained by Nichol *et al.* using frontal chromatography. Our results show the same slope for $\ln K_D$ as a function of $< C_i > (1 - K_D)$ as those obtained by Shearwin & Winzor [31], which means the B_2 values are the same. The solution conditions for the two data sets differ, but other studies [5, 18] have shown that B_2 for BSA is insensitive to many changes in solution conditions until crystallizing conditions are approached. Therefore we expect to measure a similar value of B_2. We measured different values of K_D than those in ref. [31] because we used a different column.

In order to further validate the extraction of B_2 from SEC, our results are compared to those obtained by light scattering in Fig. 2.7, and in Table 2.1. Fig. 2.7 shows the dependence of B_2 on solution ionic strength (added NaCl concentration) for lysozyme. Our data agrees quantitatively with those previously obtained over a wide range of ionic strengths. Table 2.1 compares B_2 values obtained in a different buffer, Potassium Phosphate 50mM pH 6.2. For this buffer our SEC measurements of B_2 also agree with those from light scattering. The differences in magnitude can be attributed to systematic errors associated with light scattering and SEC measurements of B_2,

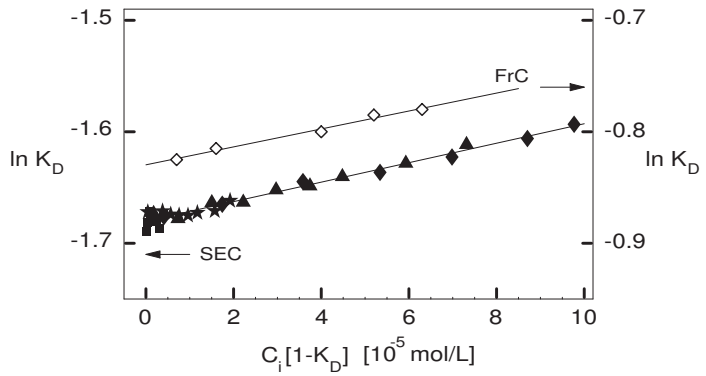

Figure 2.6: A comparison of size exclusion chromatography (SEC) and frontal chromatography measurements for BSA is shown. Open diamonds: BSA in Sodium Acetate 20mM, NaCl 0.18M, pH=4.6, $B_2 = 1.9 \times [10^{-4}$ mL mol g$^{-2}]$ [31]. Black points are for BSA in Potassium Phosphate 50mM, pH=6.2, $B_2 = 2.0 \times [10^{-4}$ mL mol g$^{-2}]$. Injected concentrations are 1.14, 4.85, 10.05, 15.0, 20.7, 25.27, 30.44, 40.72, 50.99 mg/mL. Injection volumes are for squares: 2μL ; stars: 10μL; triangles: 40μL; diamonds: 100μL.

not statistical variation. Note that previously published results for B_2 from various groups, as shown in Fig. 2.7, differ by as much or more than the values shown in Table 2.1. These results illustrate the ability of SEC to track the evolution of protein interactions from net repulsive $B_2 > 0$ to attractive $B_2 < 0$.

2.5 Conclusion

In the experiments described in this chapter we adapted the idea of Nichol *et al.* and presented measurements of protein second virial coefficients (B_2) using size exclusion liquid chromatography implemented with commercially available instrumentation, thereby reducing the cost in time and material of performing B_2 measurements for protein solutions. After calculating the protein concentration in the solute zone, our results agree with those previously obtained using the independent method of static light scattering.

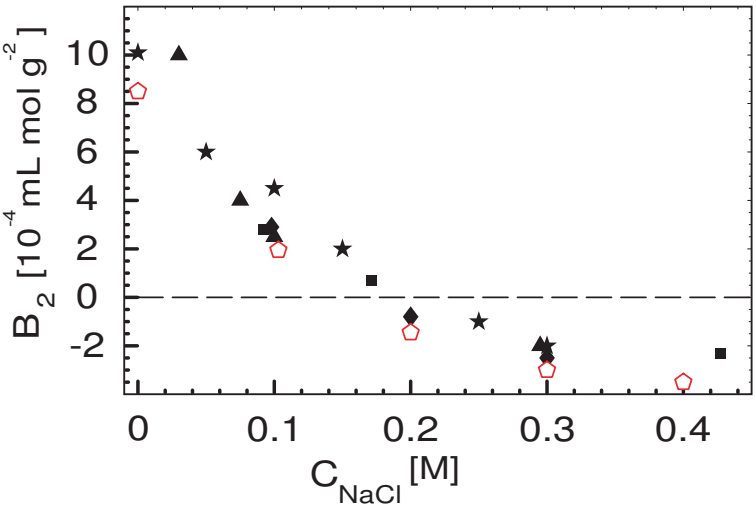

Figure 2.7: A comparison of size exclusion chromatography (SEC) and light scattering measurements of B_2 for lysozyme is shown. $B_2[10^{-4}$ mL mol $g^{-2}]$ is plotted as a function of NaCl concentration. Buffer: Sodium Acetate 50 mM pH 4.7. The SEC measurements are denoted by open pentagons. The data for 0, 100, 200, and 300 mM NaCl were taken on a TSK column, and the data for 400 mM NaCl was with a YMC column. The remaining data comes from published light scattering data. Black diamonds: Gripon *et al.*[29], black triangles: Velev *et al.* [19], black stars: Kulkarni *et al.* [30], black rectangles: Muschol *et al.* [28]

Chapter 3

Light Scattering and Phase Behavior of Lysozyme/PEG Mixtures

3.1 Introduction

The water soluble polymer poly(ethylene glycol)(PEG) has been utilized extensively to induce protein crystallization [32]. PEG is known to be almost completely inert meaning that it does not interact with proteins in solution. Low molecular weight (3350 g mol^{-1}) PEG is approved by the food and drug administration (FDA) for human consumption in low doses as a laxative. The FDA has approved numerous pharmaceutical products for therapeutic use which contain proteins with attached PEG moieties and PEG is used as an additive to consumer products such as toothpaste. If PEG is completely inert, then why does adding PEG to a protein solution often induce crystallization? The purely entropic depletion attraction discussed in Section 1.1.2 is one mechanism able to explain how inert PEG molecules could induce attraction between protein molecules subsequently leading to crystallization. Although

the soluble protein lysozyme crystallizes without the addition of PEG, adding PEG does increase the rate of lysozyme crystal nucleation [33]. This chapter addresses the question of whether or not PEG induces attraction between lysozyme molecules.

In addition to a liquid to crystal transition, protein solutions exhibit a metastable liquid-liquid phase transition when cooled [34, 35, 36]. This phase transition temperature is termed the *cloud point* (T_{cloud}) since at this temperature a transparent protein solution becomes turbid as liquid droplets of high protein concentration form in a liquid of lower protein concentration. In the protein crystallization literature liquid-liquid phase separation is referred to as "oiling-out". Numerical simulations by ten Wolde and Frenkel [37] suggested that this metastable liquid-liquid phase transition effects protein crystal nucleation. They predicted that the free energy barrier to crystal nucleation is lowered near a metastable liquid-liquid critical point. The effect of added PEG on T_{cloud} was studied for several of the γ-crystallin proteins by Benedek and co-workers who found that T_{cloud} of γS crystallin increases as PEG is added [36] in agreement with depletion attraction whereas for γD crystallin their results [13] indicate a departure from pure depletion. Galkin and Vekilov [33] studied lysozyme/PEG mixtures and found that the effect of PEG molecular weight on T_{cloud} depended on the solution's ionic strength so no clear evaluation of the depletion effect could be made. Because the cloud point depends on salt type and concentration [38], all our measurements were performed in constant solution conditions.

In this chapter the free energy of lysozyme/PEG mixtures is modelled by the two component virial expansion given in Section 1.1.1 by Eq.(1.7).

3.2 Theory

3.2.1 Equivalent Hard Sphere Radii

The ratio of lysozyme to PEG measured hydrodynamic radii, r_H, in our experiments varied in the range $3 \geq r_{\mathrm{H}}^{\mathrm{lys}}/r_{\mathrm{H}}^{\mathrm{PEG}} \geq 0.8$. Therefore we need to account for the fact that PEG molecules, which are nearly as large or larger than lysozyme molecules, can wrap partially around proteins thereby reducing the polymer/protein excluded volume. This is done by employing the effective polymer radius (r_{eff}) defined in Section 1.1.2. In order to use the results outlined in Section 1.1.2, the protein radius and PEG r_g are needed. Our procedure was to equate the protein's radius with its measured r_H. Our procedure to determine the PEG's r_g is described in the following paragraph.

The PEG radii of gyration for the molecular weights employed here were too small to measure with static light scattering because r_g is much less than the wavelength of light. In order to determine r_g we therefore first measured r_H of the polymers using dynamic light scattering (Section 3.2.4) and then used the relation

$$r_g/r_H = 1.484 M_w^{0.012} \tag{3.1}$$

which was found from static and dynamic light scattering experiments performed by Devanand & Selser [39] on large molecular weight PEGs $0.8 \times 10^5 \leq M_w \leq 10^6$ g mol^{-1}. This should be compared to the theoretical value, $r_g/r_H = 1.56$, for a polymer in a good solvent where the chains cannot interpenetrate [40]. Table 3.1 lists the measured hydrodynamic radii of lysozyme and PEG, the PEG radii of gyration and the PEG effective hard sphere radii. Our measurement of r_H for lysozyme falls within the range of previously reported values by Grigsby *et al.* [41].

	r_{H}[nm]	r_{g}[nm]	r_{eff}[nm]	$r_{\mathrm{H}}^{\mathrm{lys}}/r_{\mathrm{eff}}^{\mathrm{PEG}}$	r_2^+[nm]
Lysozyme	2.23	-	-	-	-
PEG1k	0.75	1.20	1.21	1.84	0.16
PEG8k	2.7	4.46	3.79	0.59	0.45
PEG12k	3.53	5.86	4.75	0.47	-0.24
PEG35k	6.0	10.1	7.25	0.31	-

Table 3.1: Hydrodynamic radii (r_{H}) of Lysozyme and PEG 1k, 8k, 12k and 35k calculated from single particle diffusion constants in the limit of zero concentration by the Stokes-Einstein relation as described in Eq.(3.12), PEG radii of gyration (r_{g}) and effective hard sphere radii (r_{eff}) of PEG determined as described in Section 3.2, Eqs.(1.14,3.1). r_{H} of PEG 1k, 8k and 35k were measured in the phosphate buffer and that of PEG 12k in the acetate buffer. The hydrodynamic radius of lysozyme was the same in both buffers. The radius of PEG needed to reproduce the measured values of B_{12} shown in Table 3.4 (r_2^+) is also shown. r_2^+ is found by equating the measured B_{12} with B_{12}^{HS} and solving for the polymer radius while holding the protein's radius fixed.

3.2.2 Cloud Point

In this section the variation of the spinodal temperature with added polymer concentration is calculated starting from the virial expansion for the free energy of a two component mixture given in Section 1.1.1. In what follows the subscript 1 refers to lysozyme and the subscript 2 refers to PEG. In a single component solution the stability limit is reached when the free energy as a function of density has an inflection point. Similarly, a two component mixture at fixed concentration becomes unstable and undergoes spinodal decomposition when the temperature reaches the spinodal temperature ($\mathrm{T_{sp}}$) defined by [42]:

$$f(\mathrm{T_{sp}}, \rho_1, \rho_2) = \frac{\partial^2 g}{\partial \rho_1^2}\frac{\partial^2 g}{\partial \rho_2^2} - (\frac{\partial^2 g}{\partial \rho_1 \partial \rho_2})^2 = 0$$

Imposing the constraint that the solution remains on the spinodal curve when polymer is added yields:

$$df = 0 = \frac{\partial f}{\partial T}dT + \frac{\partial f}{\partial \rho_1}d\rho_1 + \frac{\partial f}{\partial \rho_2}d\rho_2$$

We want to calculate the dependence of spinodal temperature on added polymer concentration at fixed protein concentration. This is done by adding the constraint $d\rho_1 = 0$ which yields:

$$\frac{\partial \mathrm{T_{sp}}}{\partial \rho_2} = -\frac{\partial f}{\partial \rho_2}(\frac{\partial f}{\partial \mathrm{T}})^{-1} \tag{3.2}$$

Inserting the virial expansion for the free energy density g ,Eq.(1.8), into Eq.(3.2) one obtains a relation between the virial coefficients and the dependence of the spinodal temperature $\mathrm{T_{sp}}$ on added polymer concentration in the limit of low polymer concentration:

$$\lim_{\rho_2 \to 0} \frac{\partial \mathrm{T_{sp}}}{\partial \rho_2} = \frac{-3C_{112} + 2(B_{12} + 3\rho_1 C_{112})^2}{\partial B_{11}/\partial T + 3\rho_1 \frac{\partial C_{111}}{\partial T}} \tag{3.3}$$

Note that in Eq.(3.3), the mixed virial coefficients have units B_{ij}[Volume] and C_{112}[Volume^2]. In all that follows we have set $\partial C_{111}/\partial T = 0$ since experimentally $C_{111} = 0$ at all temperatures (see Fig. 3.6).

We define the numerator of Eq.(3.3) to be

$$\gamma = -3C_{112} + 2(B_{12} + 3\rho_1 C_{112})^2 \tag{3.4}$$

The PEG molecular weight dependence enters Eq.(3.3) only through the virial coefficients. From Eqs.(1.10, 1.11, and 3.3) it can be shown that for a hard sphere mixture $\gamma > 0$ for all sphere sizes r_1 and r_2 and concentrations ρ_1. In the limit of small protein concentration ($\rho_1 \to 0$) the change in the spinodal temperature scales with the ratio of polymer to protein size ($q = r_2/r_1$) as:

$$\lim_{\rho_2 \to 0, \rho_1 \to 0} \frac{\partial \mathrm{T_{cloud}}}{\partial \rho_2} = (B_{11}^{\mathrm{HS}}/4)^2 \left(\frac{q^3}{2}(12 + 15q + 6q^2 + q^3) \right) / (\frac{\partial B_{11}}{\partial T}) \tag{3.5}$$

Annunziata *et al.* [13] used scaled particle models to calculate the free volume available to ideal polymer coils in protein/polymer mixtures. From that free volume, the variation of the spinodal temperature was calculated and found to have the same

scaling form as in Eq.(3.5).

For a binary mixture the sign of the spinodal temperature variation ($\lim_{\rho_2 \to 0} \partial \mathrm{T}_{\mathrm{sp}}/\partial \rho_2$) is set by the sign of the temperature variation of the protein second virial coefficient $\partial B_{11}/\partial \mathrm{T}$. Thus, if the protein/polymer interaction is due solely to depletion effects then the sign of $\lim_{\rho_2 \to 0} \partial \mathrm{T}_{\mathrm{sp}}/\partial \rho_2$ cannot change with molecular weight of the added polymer.

3.2.3 Static Light Scattering

In order to explore lysozyme/PEG mixtures further, virial coefficients were determined by light scattering and compared with depletion theory. Light scattering has been used to investigate protein solutions for more than fifty years [43]. Effective virial coefficients in mixtures of proteins and PEG have been measured by light [30, 44] and X-ray [45] scattering along with solubility [46] studies.

We follow the multicomponent fluctuation theory developed by Kirkwood & Goldberg [47] and independently by Vrij [48] to relate light scattering measurements from ternary water, lysozyme and PEG solutions to the virial coefficients of interest. This approach treats the scattering from all solutes on equal footing, thereby eliminating the need to make any assumptions concerning the scattering from a given component. Tong *et al.* [49] used a similar framework to study the light scattering from mixtures of colloids and polymers. Tong *et al.* showed that their system behaved qualitatively as a hard sphere mixture and found an expression for the effective second virial coefficient between colloids in the presence of added polymer. Prausnitz and co-workers [44] used light scattering to measure mixed second virial coefficients in lysozyme/PEG and lysozyme/dextran mixtures. Their data show that, depending on the type of salt present in solution, mixed second virial coefficients can increase or decrease with increasing polymer molecular weight. Other analyses of light scattering from protein/polymer mixtures [30] have employed an effective one component

analysis, thereby neglecting interference contributions from the polymers' scattering. A multicomponent approach to X-ray scattering data from protein/polymer mixtures has previously been made by Tardieu and co-workers [50] in order to extract the potential of mean force between the protein urate oxidase and PEG where the protein radius is at least twice as large as the largest PEG employed. Their data are qualitatively consistent with a purely entropic depletion model for the polymer's effect.

Kirkwood & Goldberg calculated the light scattering from a ternary system such as a mixture with two solute components and a solvent fluid. They showed that the excess light scattering of a two solute system (R_{1+2}) over that of a single solute system (R_2) can be written in a simple form:

$$\frac{Kc_1}{R_{1+2} - R_2} = \alpha + \beta \times c_1 \tag{3.6}$$

Here $K = 2(\pi n_o n_1)^2 / N_A \lambda^4$ where n_o is the solvent refractive index, $n_i = \frac{dn}{dc_i}$ is the refractive index increment, N_A is Avogadro's number, λ is the wavelength of the incident radiation in vacuum, c [mg mL^{-1}] is the weight concentration and R is the Rayleigh ratio, (Eq.(3.13)).

Experimentally, we find that the solution refractive index depends linearly on the solute concentrations as shown in Fig. 3.1, so that n_1 and n_2 are independent of concentration, although Kirkwood & Goldberg's treatment can also incorporate concentration dependent n_i. In Section 3.4 and Figures 3.4 & 3.6 we show experimentally the third virial coefficients for the single solute systems, i.e. protein or polymer alone in solution, are zero ($C_{iii} = 0$) which simplifies the analysis.

Eq.(3.6) has the same form as the equation for the excess scattered intensity

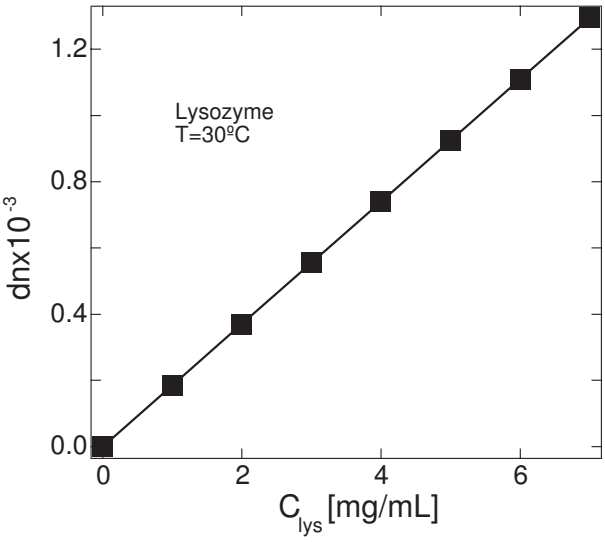

Figure 3.1: The refractive index increment $dn/dc = 1.85 \times 10^{-4}$ mL/mg for Lysozyme in the phosphate buffer at $T = 30°$C was found from the linear fit to these data points as shown. The refractive index change is linear in the solute concentration. The values of dn/dc listed in Table 3.2 were found from similar graphs for lysozyme in the acetate buffer and all PEGs.

of a single component solution over that of the solvent:

$$\frac{Kc_1}{R} = \frac{1}{M_1} + 2B_{11} \times c_1 \tag{3.7}$$

For a single solute system the intercept of Kc/R as a function of c is the inverse of the molecular weight and the slope is twice the solute's second virial coefficient. For the case of a 2 solute system α and β depend explicitly on the added polymer properties (M_2,n_2), the polymer concentration c_2, and the thermodynamic interaction between the protein and polymer molecules as represented by the mixed virial coefficients:

$$\alpha = 1/M_1 + 4c_2 m B_{12} \tag{3.8}$$

where $m = M_2 n_2 / M_1 n_1$. The mixed second virial coefficient B_{12}[mL mol g^{-2}] is obtained by measurements of the intercept α as a function of polymer concentration c_2 shown in Figure 3.8. In the limit of no added polymer ($c_2 = 0$) Eq.(3.8) simplifies to

the familiar one-component solution result, where the Rayleigh ratio is proportional to the solute molecular weight.

The coefficient β is given by

$$\beta = 2\left(B_{11}^{\text{eff}} + mc_2(3C_{112} + 2B_{11}B_{12}M_1)\right) \tag{3.9}$$

with $B_{11}^{\text{eff}} = B_{11} + c_2\left[(3C_{112} - 2B_{12}^2M_2)\right]$. Performing a linear fit to β as a function of c_2, as shown in Fig.3.9, we obtain the mixed third virial coefficient C_{112} since all the other quantities in Eq.(3.9) have been determined: B_{11} is found from light scattering experiments with component 1 alone; B_{12} is found from Eq.(3.8); the molecular weights M_i are measured by Eq.(3.7) one component at a time and the refractive index increments n_i are measured separately.

Adding polymers to a protein solution changes the potential of mean force between protein molecules. Changes in the effective protein interaction can be tracked by considering the following gedanken experiment. Add invisible polymers to the protein solution and ask what is the effect on the second virial coefficient between protein molecules. Experimentally, using an index matching solvent for all polymer concentrations would make the polymer invisible. As discussed by Vrij [51] and Tong *et al.* [49] in this case the polymer molecules do not scatter light ($n_2 = 0$) but still effect the protein interactions. Then

$$Kc_1/(R_{1+2} - R_2) = 1/M_1 + 2B_{11}^{\text{eff}} \times c_1 \tag{3.10}$$

. This effective second virial coefficient between protein molecules in the presence of polymers results from Eq.(1.2) with the potential of mean force $u(r)$ modified by the presence of polymers. Tong *et al.* [49] noted that de Hek & Vrij [52] calculated B_{11}^{eff} using the full Asakura & Oosawa depletion potential, which reduces to B_{11}^{eff} in the limit of low polymer concentration. For a hard sphere mixture Tong *et al.* [49]

found the expression for the effective second virial coefficient in terms of the polymer number density ρ_2

$$B_{11}^{\text{eff}} = B_{11}^{\text{HS}} \left[1 - \frac{\rho_2 \pi}{6} \frac{(r_1 + r_2)^6}{r_1^3} f(\delta) \right] \qquad 0 \leq f(\delta) \leq 1 \tag{3.11}$$

where $\delta = r_1/r_2$ and $f(\delta) = 1 - (8 + 15\delta + 6\delta^2 + \delta^3)\delta^3/(1 + \delta)^6$. Since $f(\delta)$ is positive, adding a small amount, ρ_2, of hard spheres of radius r_2 to a suspension of hard spheres with radius r_1 can only decrease the effective second virial coefficient of component 1. In other words, for hard spheres adding a second component always induces attractions. This is consistent with the depletion attraction discussed in Section 1.1.2. Only $3C_{112} > 2B_{12}^2 M_2$ will lead to induced repulsion or $\partial B_{11}^{\text{eff}}/\partial c_2$.

3.2.4 Dynamic Light Scattering

Hydrodynamic radii were measured by dynamic light scattering (DLS). DLS measures the intensity autocorrelation function $g_1(t) = \langle I(t_o) I(t_o + t) \rangle$ where $I(t)$ is the scattered intensity as a function of time. For a single solute diffusing the intensity autocorrelation function decays exponentially $g_1(t) = e^{-\Gamma t}$. The diffusion constant (D) is calculated from $D = \Gamma/q^2$ where $q =$ is the amplitude of the scattering vector [53]. r_{H} is calculated by the Stokes-Einstein relation for spherical particles in the infinitely dilute limit :

$$r_{\text{H}} = \lim_{c \to 0} r_{\text{H}}(c) = \lim_{c \to 0} \frac{k_B T}{6\pi\eta D(c)} \tag{3.12}$$

where η is the solvent viscosity.

3.3 Materials & Methods

Six times recrystallized and lyophilized hen egg white lysozyme was purchased from Seikagaku America (Falmouth, MA). The molecular weight of lysozyme based on its

amino acid sequence is 14,400 g mol^{-1}. We tested the lysozyme purity by size exclusion chromatography and dynamic light scattering and found pure protein existing as a monomer in solution. Lysozyme was used without further purification

Poly(ethylene glycol) (PEG) was purchased from Sigma (St.Louis, MO) and Fluka (Buchs, Switzerland). We designate the manufacturer's stated value for the PEG molecular weight with the nomenclature PEGnk, meaning PEG n$\times 10^3$ [g mol^{-1}]. The degrees of polymerization (N) for PEG 1k, 8k and 12k are listed in Table 3.4 and were calculated via $N = M_2/44$ where 44 g/mol is the molecular weight of the PEG monomer.

The protein and PEG were dissolved in two aqueous buffers: a phosphate buffer at pH 6.2 and an acetate buffer at pH 4.6. All buffer components were obtained from Sigma. The phosphate buffer was prepared by mixing solutions of sodium phosphate monobasic (NaH_2PO_4 0.2M+NaCl 0.5M) and dibasic (Na_2HPO_4 0.2M+NaCl 0.5M) to reach pH 6.2, where M $\equiv$ [mol L^{-1}]. The acetate buffer was prepared by adding concentrated acetic acid to solutions of Sodium Acetate (NaAc) 50mM + Sodium Chloride (NaCl) 150mM to adjust the pH to 4.6. The acetate buffer was chosen for comparison to previous light scattering studies [30, 28]. The phosphate buffer was chosen because the liquid-liquid phase separation temperatures for lysozyme fall in an experimentally convenient range for this buffer.

A Millipore (Billerica, MA) Elix system produced deionized water for use as the solvent. All solutions were centrifuged at $\sim 12000 \times g$ for 1 hour and then filtered through Millipore Millex 0.22μm syringe filters directly into precleaned, disposable scattering cuvettes obtained from Fisher Scientific (Pittsburgh, PA). The lysozyme concentrations were measured from these centrifuged and filtered solutions by UV absorption measurements on a Varian Instruments (Palo Alto, CA) Cary-50Bio spectrophotometer using an extinction coefficient $\epsilon_{280\text{nm}} = 2.64$ mL/mg cm.

Refractive index increments ($n_i = \partial n/\partial c_i$) of lysozyme and PEG in both

	n_i [10^{-4}mL mg^{-1}]
$\frac{\text{Lys}}{\text{(Phos Buff)}}$	1.85
$\frac{\text{Lys}}{\text{(Ac Buff)}}$	1.77
$\frac{\text{PEG}}{\text{(Phos Buff)}}$	1.34
$\frac{\text{PEG}}{\text{(Ac Buff)}}$	1.37

Table 3.2: Refractive index increments $n_i = \partial n/\partial c_i$ of lysozyme and PEG in the phosphate and acetate buffers, measured as described in Section 3.3. n_i was found to be independent of the PEG molecular weight and solution temperature for $15° \leq \text{T} \leq 40°$. These measurements of n_i are commensurate with previously published results [39].

buffers were measured using a Brookhaven Instruments (Holtsville, NY) differential refractive index detector at λ =620 nm. Although the refractive index of the solution depends sensitively on temperature, n_i was found to be independent of temperature for $15 \leq T \leq 40$°C. Table 3.2 lists the measured values of n_i used in all calculations which closely match previously published results.

Cloud point temperatures (T_{cloud}) of protein polymer mixtures were determined by optical microscopy as an approximation of the spinodal decomposition temperatures. Rectangular glass capillaries (0.1mm path length) obtained from VitroCom (Mt. Lakes., NJ) were filled with solution, flame sealed and then placed in a custom built temperature controlled microscope stage. The temperature at which homogeneous nucleation of dense droplets occurred was called the cloud point. The temperature of each solution was cycled up and down at approximately 1°C min^{-1} through the cloud point several times for each measurement. Little or no hysteresis (≤ 0.5°C) was observed when comparing cloud points obtained by cooling and heating. This suggests that the cloud point closely approximates the coexistence curve. The cloud point and coexistence curves were shown to agree for γ-B crystallin [35] protein solutions, when using a similar method.

The static and dynamic light scattering experiments were performed using an ALV (Langen, Germany) goniometer and correlator system with a 22mW HeNe (λ =

633 nm) laser and an avalanche photodiode detector. The temperature of samples in the goniometer system was controlled to within ±0.1°C. All of our light scattering experiments were performed using the *vu* mode in which vertically polarized light is incident upon the sample and all polarizations are detected. Absolute Rayleigh ratios of protein and polymer solutions were determined by using pure toluene as a standard whose Rayleigh ratio is known to be ($R_{\text{tol}} = 1.35 \times 10^{-5}\text{cm}^{-1}$) at this wavelength and T= 20°C [54]. The procedure was to first measure the scattered intensity of pure toluene (I_{tol}) filtered through 0.2μm PTFE membranes obtained from Fisher. Then the scattering of the buffer (I_{buff}) was measured before measuring the light scattering intensity of a protein solution (I_{sol}). The Rayleigh ratio of a protein solution was then determined by:

$$R_{\text{sol}} = \frac{I_{\text{sol}} - I_{\text{buff}}}{I_{\text{tol}}} R_{\text{tol}} (\frac{n_{\text{buff}}}{n_{\text{tol}}})^2 \tag{3.13}$$

using the refractive index correction factor [43]. The refractive index of toluene was taken to be: $n_{\text{tol}} = 1.496$ at T= 20°C and a wavelength of $\lambda = 633$ nm. The observed scattering volume varies as $1/\sin(\theta)$ where θ is the angle between the incident and scattered wave vectors. After correcting for this variation the scattering from toluene was angle independent for $30^\circ \leq \theta \leq 150^\circ$ to within $< 2\%$ which is within the manufacturer's recommendations for the alignment quality in order to carry out SLS experiments.

3.4 Results

3.4.1 Cloud Point Temperature Variation

Figure 3.2 shows the cloud point temperatures (T_{cloud}) of lysozyme solutions in the phosphate buffer. The measured dependence of T_{cloud} on lysozyme concentration qualitatively parallels that of previous investigations [55, 34]. These studies showed

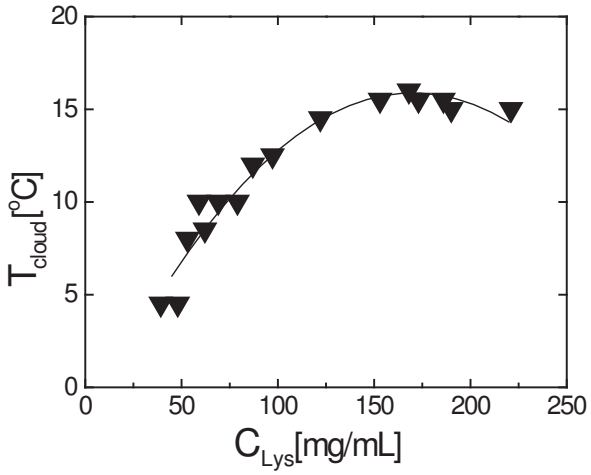

Figure 3.2: Cloud point temperatures (T_{cloud}) as a function of lysozyme concentration are shown for lysozyme in the phosphate buffer. The line is a guide to the eye.

that T_{cloud} depends on the solution pH, buffer conditions and added salt concentration. Therefore, the quantitative difference between these previous measurements of T_{cloud} and our cloud point temperature measurements is accounted for by the differences in solvent conditions.

The effect of adding PEG on the cloud point temperature is shown in Fig.3.3. We extracted the dependence of the cloud point on polymer concentration in the dilute polymer limit $\lim_{\rho_2 \to 0} \partial T/\partial \rho_2$ from these data. For dilute PEG concentrations, low molecular weight PEGs depress the cloud point, i.e. stabilize the solution, and higher molecular weight PEGs raise the cloud point, i.e. destabilize the solution.

3.4.2 Light Scattering Data

Static light scattering data for PEG 1k, 8k and 12k solutions at T=20°C are presented in Fig. 3.4. Table 3.4 shows the PEG molecular weights extracted from these data. These values differ from the manufacturer's stated molecular weights but are within the manufacturer's specifications that up to a 20% deviation from the stated mean molecular weight may be present in any given batch. Table 3.4 compares our measured second virial coefficients for PEG to those for hard spheres whose radii are taken to be

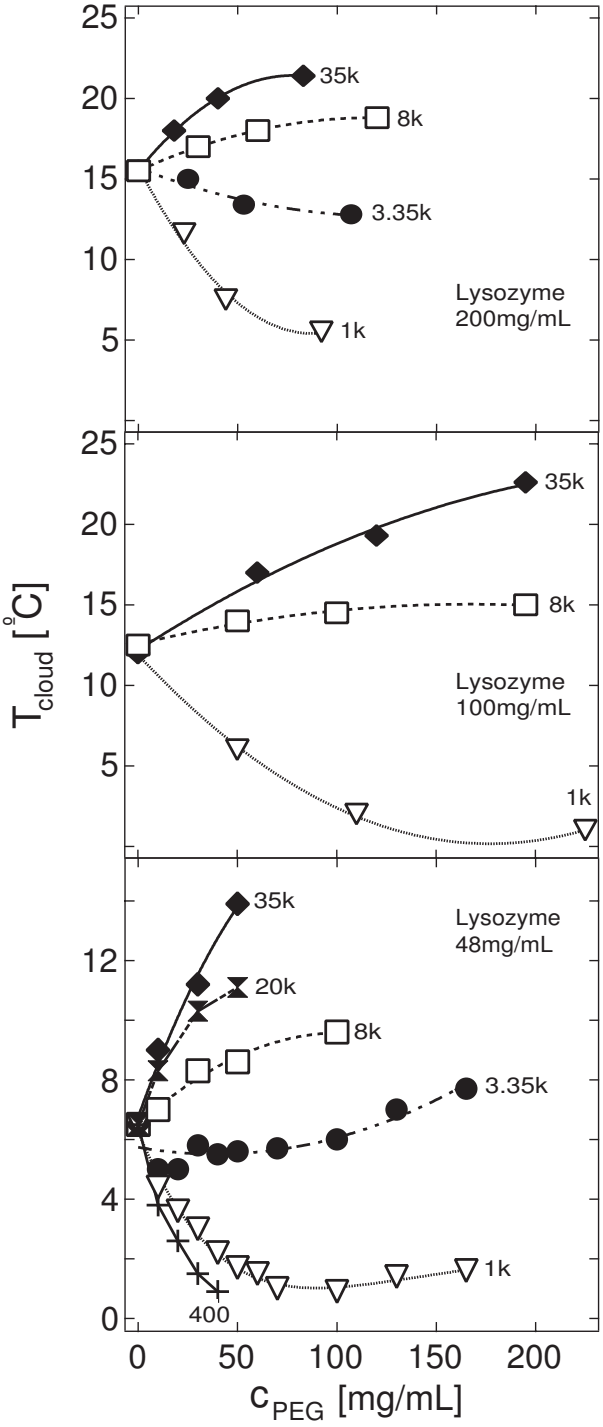

Figure 3.3: Cloud point temperatures (T_{cloud}) of lysozyme/PEG mixtures in the phosphate buffer are plotted as a function of PEG concentration for PEG molecular weights ranging from 400 to 35k g mol^{-1} at fixed lysozyme concentrations as labelled. The data in panel c) were measured by T. Virmani. The data in panels a) and b) were repeated by S. Berejnov for verification. The lines are guides to the eye.

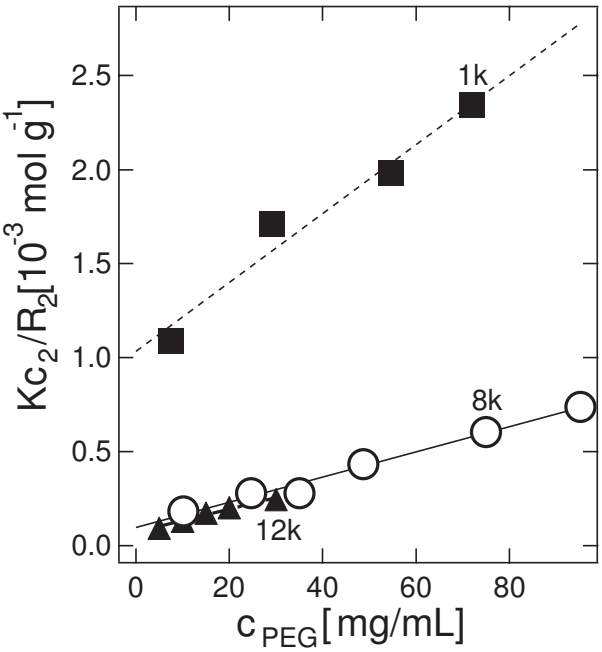

Figure 3.4: Static light scattering data for PEG1k and 8k solutions in the phosphate buffer and for PEG12k solutions the acetate buffer at T = 20°C. The filled squares (■) correspond to PEG1k, the open circles (○) to PEG8k and the filled triangles (▲) to PEG12k. The lines are fits to $Kc_2/R_2 = (1/M_2) + 2B_{22} \times c_2$, from which the PEG molecular weights (M_2) and second virial coefficients (B_{22}) are determined. The results are presented in Table 3.4 and agree well with previous results [39].

the PEG radii of gyration (r_g) listed in Table 3.1. Here r_g is used as the relevant length scale for PEG/PEG interactions. The measured PEG second virial coefficients are the same order as those for equivalent hard spheres, which shows that the phosphate and acetate buffers are both good solvents for PEG.

Figure 3.6 presents static light scattering data for lysozyme and lysozyme/PEG solutions with the scattering ratio $\frac{Kc_1}{R_{1+2}-R_2}$ plotted as a function of c_1. As outlined in Eq.(3.6), this ratio should depend linearly on c_1. From the fits to the data shown in Fig. 3.6 with no added PEG in the phosphate buffer, panels a) and b), we find M_1 =13800±500 g mol^{-1} and $B_{11} = -3.95 \pm 0.3 \times 10^{-4}$ mL mol g^{-1} $\approx -0.7 B_{11}^{\mathrm{HS}}$. For lysozyme in the acetate buffer, panel c), we find that M_1 = 13700±140 g mol^{-1} and $B_{11} = 4.87 \pm 0.2 \times 10^{-5}$ mL mol g^{-1} $\approx 0.1 B_{11}^{\mathrm{HS}}$. The mixed virial coefficients, B_{12} and C_{112}, are obtained from linear fits to α and β as functions of PEG concentration as

	M_2 [10^3g/mol]	N	B_{22} [10^{-3}mL mol/g^2]	$B_{22}/B_{22}^{\rm HS}$
PEG1k	0.97 ± 0.1	22	9.2± 1.0	0.5
PEG8k	10.4±0.5	236	3.35±0.12	0.4
PEG12k	14.1± 2.2	320	3.1± 0.3	0.3

Table 3.3: PEG molecular weights (M_2) and second virial coefficients (B_{22}) taken from the data shown in Fig. 3.4 at T= 20°C are shown in the first and third columns. The equivalent hard sphere values were obtained as described in Section 3.2 using $r_{\rm g}$ of PEG to determine $B_{22}^{\rm HS}$. The $r_{\rm g}$ values are listed in Table 3.1. The degree of polymerization $N = M_2/44$ is shown in the second column. The data for the PEG1k and 8k solutions was taken in the phosphate buffer and in the acetate buffer for PEG12k solutions.

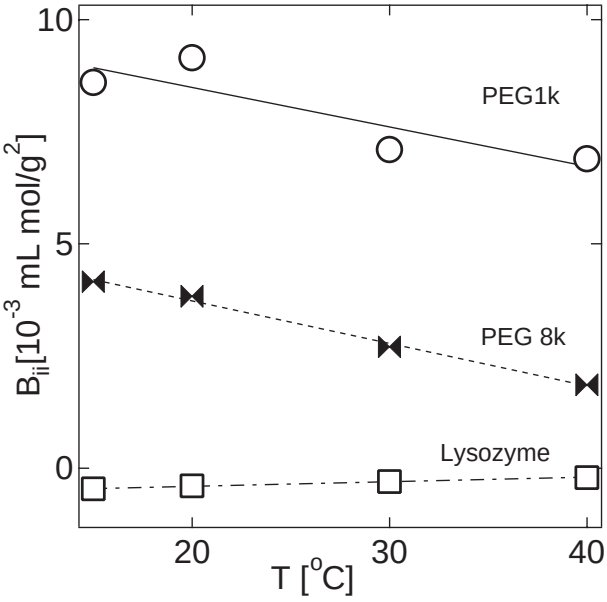

Figure 3.5: Temperature dependence of second virial coefficients B_{ii} [mL mol g^{-2}] vs T [°C] for lysozyme, PEG 1k and PEG 8k in the phosphate buffer. The variation of B_{11}(T) for lysozyme in the acetate buffer (not shown) is almost identical to that of lysozyme in the phosphate buffer. The lines are linear fits to the temperature variation of $B_{ii}(T)$: $\partial B_{11}/\partial T = 1.0 * 10^{-5}$ mL mol g^{-2} °C^{-1}; $\partial B_{22}^{\rm P1k}/\partial T = 8.8 * 10^{-5}$T mL mol g^{-2} °C^{-1}; $\partial B_{22}^{\rm P8k}/\partial T = 9.5 * 10^{-5}$T mL mol g^{-2} °C^{-1}.

described in Section 3.2 and shown in Figures 3.8 and 3.9. In the limit of no added polymer ($c_2 \to 0$) α is equal to $1/M_1$. However, Fig. 3.8 shows that we measured an $\sim$10% variation in α for different experiments. We attribute this variation to error in measuring the scattering from the buffer with no solute as a background, I_{buff} in Eq.(3.13), because the scattering from the buffer is so small. The results of the fits for B_{12} and C_{112} are shown in Table 3.4. We found B_{12} and C_{112} to be temperature independent within experimental uncertainty. This means that the slopes of the linear fits in Fig. 3.8 are parallel for all temperatures within the large experimental error bars. The slope of the linear fit to the T= 40°C data in Figure 3.8 panel c) is the only line that may indicate some temperature variation of B_{12} in the acetate buffer. The temperature variation of slopes of the linear fits in Fig. 3.9 with polymer concentration are accounted for by the temperature dependence of $B_{11}(T)$, according to Eq. (3.9). Table 3.4 also compares our measured values of the mixed virial coefficients, B_{12} and C_{112}, to those of an equivalent hard sphere mixture, B_{12}^{HS} and C_{112}^{HS}, calculated from Eqs.(1.10, 1.11). The lysozyme equivalent hard sphere has the radius r_{H} and the PEG equivalent hard spheres have the radii r_{eff} shown in Table 3.1.

Mixed second virial coefficients have previously been measured for lysozyme/PEG mixtures with light scattering by Prausnitz and co-workers [44] and with solubility experiments by Atha and Ingham [46]. The latter measured virial coefficients of lysozyme-PEG4k mixtures in 50mM Potassium Phosphate and 100mM Potassium Chloride pH=7.0 at T=23°C [46] and found that $B_{12}^{\text{Lys-P4k}} = 2 \times 10^{-4}$ mL mol g^{-2}. This value is comparable to our result for Lysozyme/PEG8k mixtures in a similar phosphate buffer, as shown in Table 3.4. Light scattering measurements by Prausnitz and co-workers [44] on lysozyme/PEG3.35k and PEG8k mixtures done in 50mM Potassium Phosphate Monobasic (KH_2PO_4) without fixing the pH found that [44] $B_{12}^{\text{Lys-P3.35k}} = 2.87 \times 10^{-4}$ mL mol/g^{-2} and $B_{12}^{\text{Lys-P8k}} = 3.4 \times 10^{-4}$ mL mol/g^{-2}. These values are also commensurate with our measurements (Table 3.4). Since virial coef-

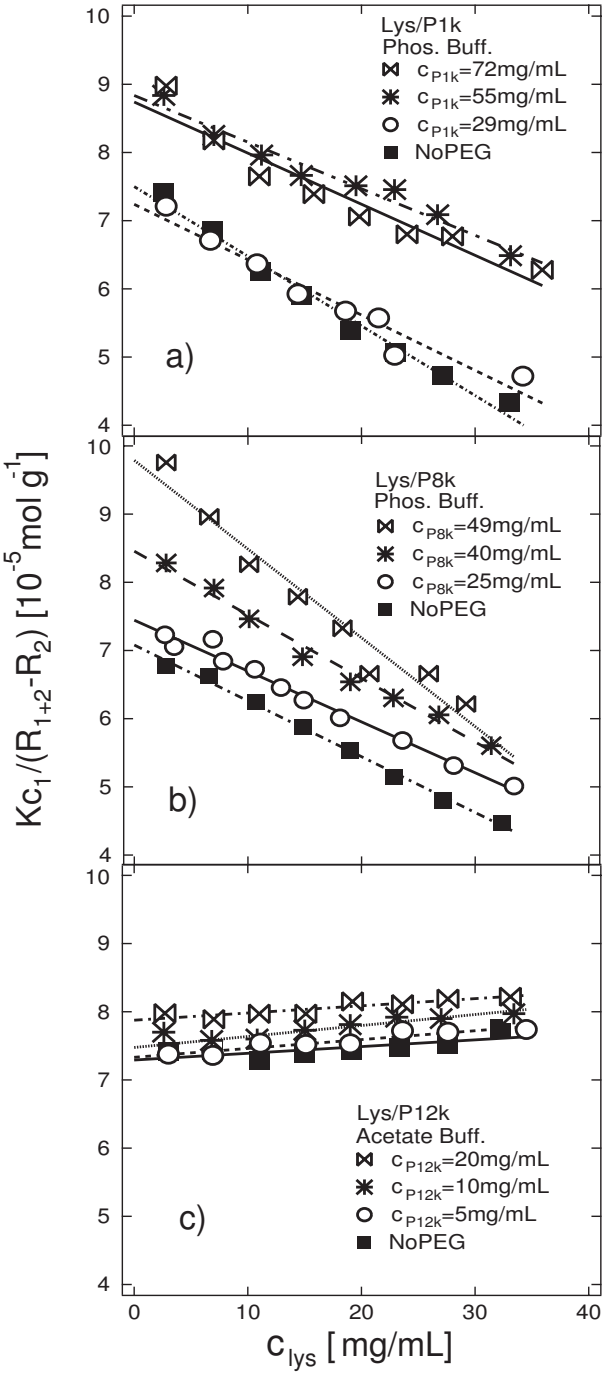

Figure 3.6: Static light scattering data is shown for lysozyme-PEG 8k and PEG 1k solutions in the phosphate buffer in panels a) and b), and for lysozyme-PEG 12k solutions in the acetate buffer in panel c), at T = 20°C. The lines are fits to Eq.(3.6) from which α and β are obtained.

ficients are sensitive to salt concentration and salt type the differences in the solvent conditions between our study and those employed by [44] can account for the quantitative difference in B_{12} in these different buffers.

The variation of β with PEG12k concentration in the acetate buffer is shown in Fig. 3.4.2 and compared with the data from Kulkarni *et al.* [30] taken in the same conditions. Our data do not display the non-monotonic variation of β with PEG concentration seen by Kulkarni *et al.* The multicomponent light scattering analysis given in Section 3.2.3 predicts a linear dependence of β on c_2 which is seen in our data. It is not known why our data differ so markedly from those of ref. [30]. Kulkarni *et al.* made two assumptions in their light scattering analysis which may contribute to the discrepancy between our data and theirs. First, they assumed that α was independent of PEG concentration and equal to the inverse of lysozyme's molecular weight. They used a fixed value of α to fit for the refractive index increment n_1 at different PEG concentrations. Secondly, they assumed that lysozyme/PEG mixtures could be treated as an effective one component solution and equated β with the effective second virial coefficient whereas the multicomponent analysis of light scattering given in Section 3.2.3 shows that this is not correct.

3.5 Analysis

3.5.1 Need for 3rd Virial

The measured dependence of β on PEG concentration shows that a virial expansion truncated at the B_{ij}'s is not sufficient. We see this from a contradiction arising by assuming $C_{112} = 0$ and examining the predictions of Eq.(3.9) regarding the light scattering data presented in Figures 3.8 and 3.9 with this assumption. In order to arrive at this contradiction set $C_{112} = 0$ in Eq.(3.9) assuming only pairwise interactions. We label the slope as β' to indicate our working assumption that $C_{112} = 0$. Then the

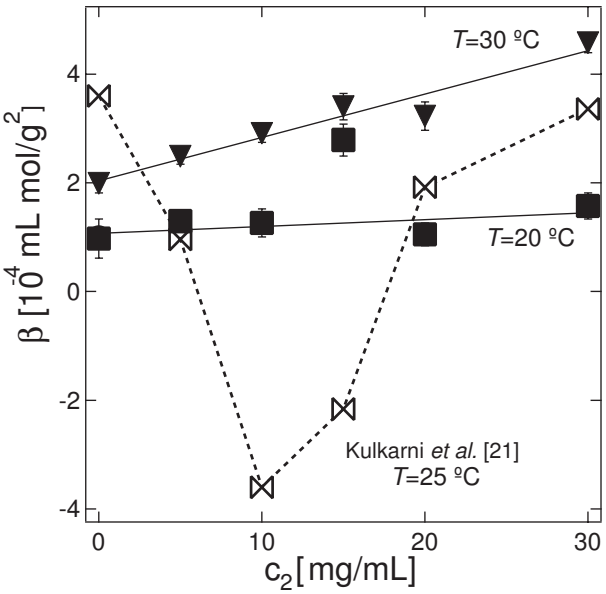

Figure 3.7: The variation of β as a function of added PEG12k concentration c_2 is shown by the filled symbols for $T = 20$, 30°C in the acetate buffer. The solid lines represent the linear fits to Eq.(3.9) used to obtain the values of C_{112} listed in Table 3.4. The open symbols were taken from Kulkarni *et al.* [30].

expression for polymer dependence of this quantity $(\partial\beta'/\partial c_2)$ becomes:

$$\frac{\partial\beta'}{\partial c_2} = -2B_{12}^2 M_2 + \frac{4B_{11}B_{12}M_1M_2n_2}{M_1n_1} \tag{3.14}$$

The second virial coefficient for lysozyme alone (B_{11}) in the Phosphate buffer is negative, as seen from Fig. 3.6. The mixed second virial coefficients (B_{12}) for lysozyme/PEG 1k and 8k mixtures are both positive as shown in Table 3.4. Therefore, the polymer concentration dependence of the slope should be negative for both lysozyme/PEG1k and lysozyme/PEG8k mixtures (i.e. $\partial\beta'/\partial c_2 < 0$). However, Figure 3.9 shows that experimentally $\partial\beta/\partial c_2 > 0$ for Lysozyme/PEG1k mixtures and $\partial\beta/\partial c_2 < 0$ for Lysozyme/PEG8k mixtures. This contradiction is shown graphically in Fig. 3.9. The double dashed line in Fig. 3.9 shows the prediction for $\partial\beta/\partial c_2$ assuming that $C_{112} = 0$ for the T=40°C data. The top panel shows that assuming $C_{112} = 0$ yields qualitatively the wrong slope for lysozyme/PEG 1k mixtures. This contradiction be-

tween the results of our assumption and experiments can be resolved by including the mixed third virial coefficient in calculating the scattered light from protein-polymer solutions.

One reaches the same conclusion by considering the polymer dependence of the cloud point temperature shown in Fig. 3.3. If we make the same assumption as above ($C_{112} = 0$) then we find for the polymer dependence of the cloud point temperature

$$\lim_{\rho_2 \to 0} \frac{\partial T}{\partial \rho_2} = \frac{2B_{12}^2}{\partial B_{11}/\partial T} > 0$$

Figure 3.5 shows that $\partial B_{11}/\partial T > 0$ for lysozyme in the phosphate buffer. So $\lim_{\rho_2 \to 0} \frac{\partial T}{\partial \rho_2} > 0$ for all PEG molecular weights assuming $C_{112} = 0$. However, Fig. 3.3 shows clearly that this slope is negative for low molecular weight PEG. Therefore we must conclude again that $C_{112} \neq 0$. Including only second virial terms in the free energy of lysozyme/PEG mixtures cannot account for either our light scattering or cloud point temperature measurements.

3.5.2 Depletion is Not Sufficient

We now compare our results to the depletion model's prediction for the effect of adding polymer to a protein solution. The Asakura & Oosawa model of ideal, penetrable polymers is not valid for PEG in our buffers because the PEG/PEG interactions are not negligible as shown by the values of B_{22} in Table 3.4. Therefore, we compare our results for the mixed virial coefficients in lysozyme/PEG mixtures to those of a binary hard sphere mixture [6].

In order to model PEG in our solutions as effective hard spheres the PEG molecules must exist as separated coils in dilute solution, not as overlapping chains in a semidilute solution. The semidilute cross-over concentration for PEG, c_2^*, is estimated as the concentration at which there is one polymer molecule per spherical

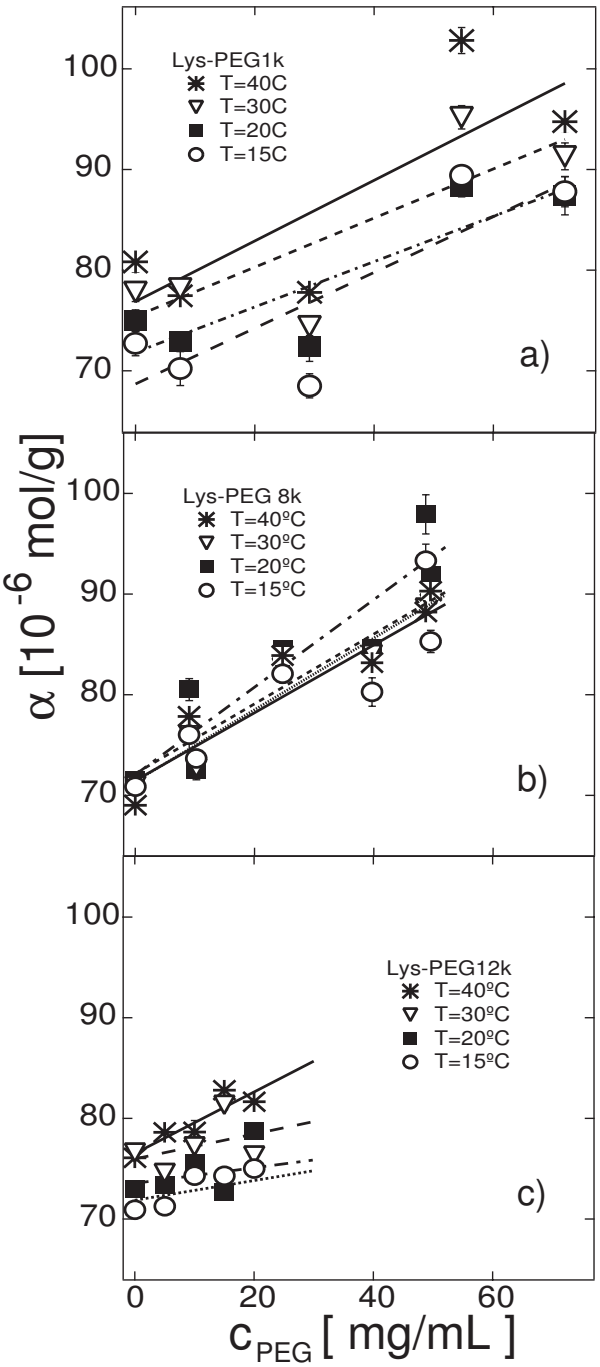

Figure 3.8: The variation of α, Eq.(3.8), as a function of PEG concentration (c_2) at different temperatures is shown for lysozyme/PEG1k and PEG8k solutions in the phosphate buffer in panels a) and b), and for lysozyme/PEG12k solutions in the acetate buffer in panel c). The lines indicate the linear fits to Eq.(3.8) used to find the B_{12} values presented in Table 3.4.

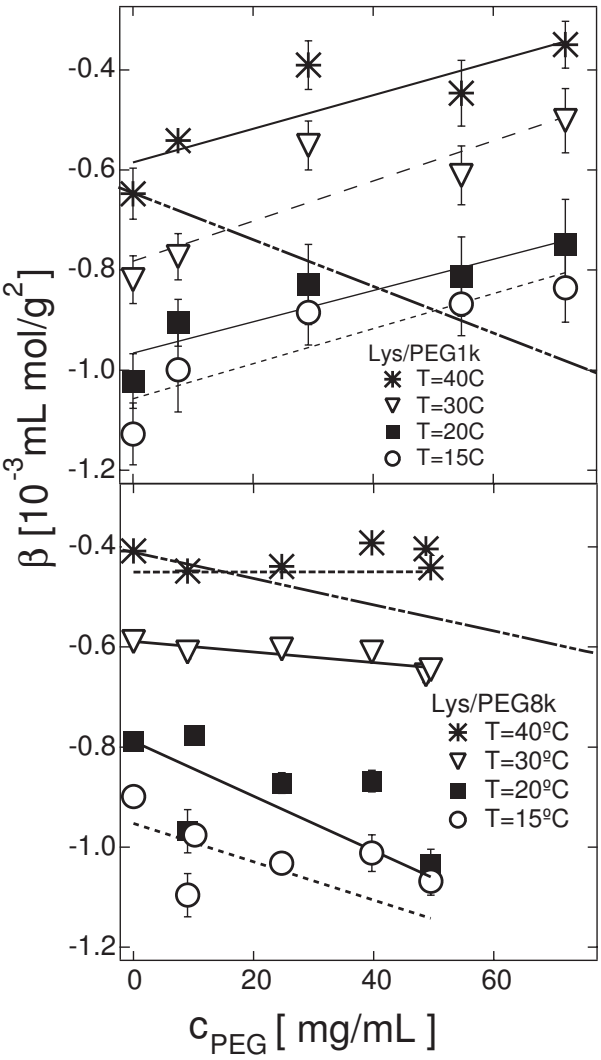

Figure 3.9: The variation of β with polymer concentration (c_2) at different temperatures is shown for lysozyme/PEG1k and PEG8k solutions in the phosphate buffer. The lines are linear fits used to obtain the values of C_{112}, Eq.(3.9), shown in Table 3.4. The double dashed line shows the dependence of β on PEG concentration assuming $C_{112} = 0$ for the T=40°C data as discussed in Section 3.5.1.

	B_{12} [10^{-4}mL mol/g^2]	$B_{12}/B_{12}^{\rm HS}$	C_{112} [10^{-4}mL^2 mol/g^3]	$C_{112}/C_{112}^{\rm HS}$
PEG1k	12.9±0.2	0.34	16.1±0.3	0.23
PEG8k	1.7±0.3	0.089	3.13±0.2	0.051
PEG12k	0.51±0.2	0.023	3.4±0.1	0.044

Table 3.4: Mixed virial coefficients (B_{12}, C_{112}) for lysozyme/PEG solutions obtained from fits to α and β, Eqs.(3.8) and (3.9) are shown. B_{12} and C_{112} were found to be independent of temperature. The equivalent hard sphere values were obtained as described in Section 3.2 using $r_{\rm eff}$ of PEG along with $r_{\rm H}$ of lysozyme to determine $B_{12}^{\rm HS}$ and $C_{112}^{\rm HS}$. The $r_{\rm eff}$ and $r_{\rm H}$ values are listed in Table 3.1. The error bars for the measured cross virial coefficients came from the linear least squares fits to the data in Figures 3.8 and 3.9 by Eqs.(3.8) and (3.9). The data for the Lysozyme/PEG1k and 8k mixtures was taken in the phosphate buffer and in the acetate buffer for Lysozyme/PEG12k mixtures.

volume defined by the polymer's radius of gyration [40]:

$$c_2^* = \frac{M_2}{N_A}\frac{1}{(4\pi/3)r_g^3} \tag{3.15}$$

The values of c_2^* are listed in Table 3.5. For the lysozyme/PEG1k mixtures, all the light scattering data and cloud point measurements were taken well below c_2^*. For the lysozyme/PEG8k and PEG12k mixtures, however, c_2^* falls in the concentration range used for light scattering measurements, but c_2^* is still larger than the PEG concentrations used to extract $\lim_{c_2\to 0}\partial {\rm T}_{\rm cloud}/\partial c_2$. Figure 3.4 shows that the light scattering data for all the PEG molecular weights and concentrations employed here are fit well by the one component light scattering equation, Eq.(3.7), which would not be true for significantly semidilute polymer solutions. These pieces of evidence, and the fact that this is only a crude estimate of c_2^*, indicate that our PEG solutions remain in the dilute concentration range where polymer coils do not overlap.

Table 3.4 list the measured mixed virial coefficients for the lysozyme/PEG mixtures. The lysozyme/PEG mixed virial coefficients (B_{12}) for all three PEG molecular weights are less than those of equivalent hard sphere mixtures. Therefore, attractive interactions must exist between the protein and polymer or the repulsion must be

	c_2^*[mg mL^{-1}]
PEG1k	223
PEG8k	45
PEG12k	28

Table 3.5: Semidilute cross-over concentrations (c_2^*) for PEG calculated from $c_2^* = M_2/N_A \times 1/(4\pi/3r_g^3)$.

softer than that between hard spheres.

Table 3.4 also lists values for the polymer radius (r_2^+) obtained by equating $B_{12}^{\rm HS}$, Eq.(1.10), to the measured value of B_{12} and solving for the polymer size holding the lysozyme size fixed at r_H. The values of r_2^+ are smaller than any reasonable measure of the polymer size. In the case of lysozyme/PEG12k mixtures $r_2^+ < 0$ demonstrating that purely repulsive interactions cannot account our measured mixed virial coefficients.

This result is consistent with previous work on lysozyme/PEG mixtures by Bhat and Timasheff [56], with Annunziata *et al.*'s [13] study of cloud point temperatures of bovine γD crystallin/PEG mixtures and with work by by Abbott *et al.* [57]. In a series of investigations, Abbott *et al.* [58, 57] studied the partitioning of various proteins in two-phase PEG/dextran systems and the neutron scattering from BSA/PEG mixtures. Their experimental data are consistent with the presence of weak attractive interactions between BSA and PEG in addition to the depletion effect. Analysis of Abbott *et al.*'s data leads to the conclusion that a 0.05 k_BT attractive interaction exists between PEG monomers and BSA. In an earlier investigation Abbott *et al.* [58] showed that protein partitioning data in two-phase PEG/dextran systems for a number of different proteins also lead to the conclusion that attractions exist between the proteins and PEG. Bhat and Timasheff's [56] densimetry studies of lysozyme/PEG solutions show that weak attractions compete with the depletion effect to determine the net protein/polymer interaction.

The measured virial coefficients shown in Table 3.4 allow us to calculate the

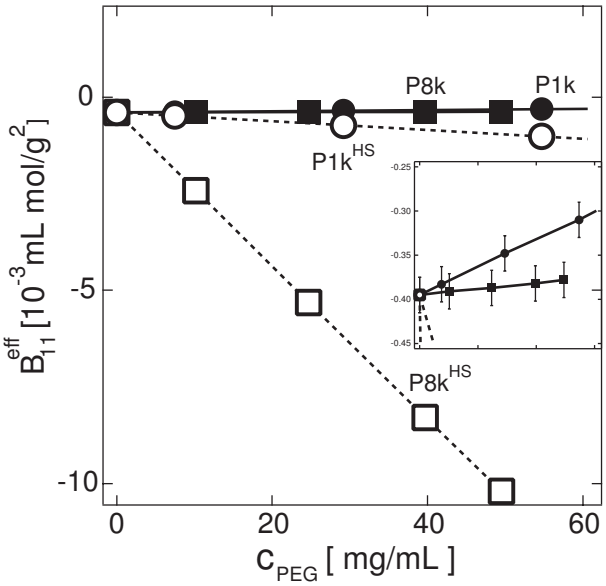

Figure 3.10: Variation of lysozyme's effective second virial coefficient, B_{11}^{eff} with polymer concentration (c_2), for lysozyme/PEG1k (•) and PEG8k mixtures (■) in the phosphate buffer. The closed symbols were obtained by using the measured values of the mixed virial coefficients listed in Table 3.4 to calculate B_{11}^{eff}. The open symbols represent the hard sphere values obtained as described in Section 3.2. The insert shows an expanded view of the lysozyme/PEG1k and PEG8k data. In this view one sees that lysozyme's effective second virial coefficient increases as a function of added polymer concentration.

variation of the effective lysozyme second virial coefficient with PEG concentration $\partial B_{11}^{\text{eff}}/\partial c_2$. Depletion theory predicts that adding PEG to a lysozyme solution induces attraction between lysozyme molecules leading to $\partial B_{11}^{\text{eff}}/\partial c_2 < 0$. Conversely, if $\partial B_{11}^{\text{eff}}/\partial c_2 > 0$ then PEG induces repulsion between lysoyzme molecules. The dependence of lysozyme's effective second virial coefficient ($\partial B_{11}^{\text{eff}}/\partial c_2$) on added PEG concentration is shown in Figure 3.10. $\partial B_{11}^{\text{eff}}/\partial c_2 > 0$ for both lysozyme/PEG1k and lysozyme/PEG 8k mixtures. We therefore conclude that adding PEG weakens the attraction between lysozyme molecules in contradiction to depletion theory.

3.5.3 Light Scattering vs. T_{cloud}

Now that the interactions in lysozyme/PEG mixtures have been determined by light scattering experiments and the collective behavior has been characterized by T_{cloud},

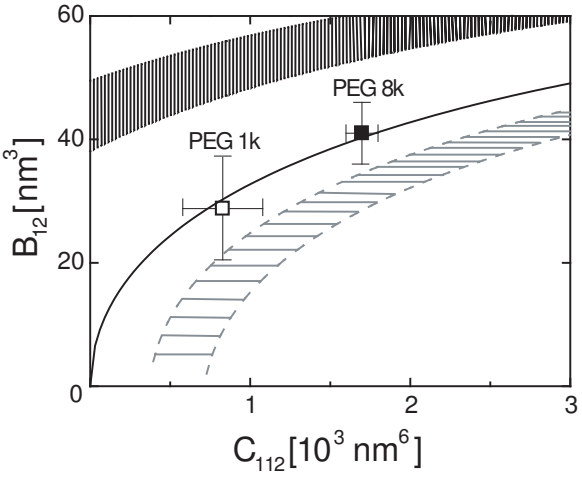

Figure 3.11: The symbols depict the mixed virial coefficients obtained by light scattering where the open square (□) corresponds to lysozyme/PEG1k mixtures and the closed square (■) to lysozyme/PEG8k mixtures in the phosphate buffer. The lysozyme concentration was fixed at $c_{\rm lys}$ =48 mg/mL. Cloud point measurements of $\lim_{\rho_2\to 0}\partial \mathrm{T}_{\rm cloud}/\partial\rho_2$ were determined from the data shown in Fig. 3.3. Sets of (B_{12}, C_{112}) were obtained by fitting the measured $\lim_{\rho_2\to 0}\partial \mathrm{T}_{\rm cloud}/\partial\rho_2$ to Eq.(3.3) using the value of $\partial B_{11}(T)/\partial T$ measured from Fig. 3.5. The solid line shows the contour $\gamma = 0$ and separates the parameter space such that $\lim_{\rho_2\to 0}\partial \mathrm{T}_{\rm cloud}/\partial\rho_2 > 0$ above the line and $\lim_{\rho_2\to 0}\partial \mathrm{T}_{\rm cloud}/\partial\rho_2 < 0$ below the line. The experimental $T_{\rm cloud}$ measurements are shown as the vertically hatched region for PEG8k, where $\gamma > 0$ Eq.(3.4), and the horizontally hatched region for PEG1k, where $\gamma < 0$. The measurements of $\lim_{\rho_2\to 0}\partial \mathrm{T}_{\rm cloud}/\partial\rho_2$ appear as regions rather than as lines due to experimental error.

we ask whether or not the interactions combined with thermodynamic theory accurately describe the collective behavior. Figure 3.11 compares the change in the spinodal temperature with added polymer ($\lim_{\rho_2 \to 0} \partial \mathrm{T_{sp}}/\partial \rho_2$) calculated from virial coefficients obtained from light scattering to the measured cloud point temperatures at $c_{\mathrm{lys}} = 48$ mg/mL. The virial coefficients obtained from light scattering correctly reproduce the sign of $\lim_{\rho_2 \to 0} \partial \mathrm{T_{cloud}}/\partial \rho_2$. However, the virial coefficients do not quantitatively agree with the range of cloud point variation. We attribute this discrepancy partly to the difference between the spinodal temperature ($\mathrm{T_{sp}}$) and the cloud point ($\mathrm{T_{cloud}}$). As discussed previously, $\gamma > 0$ for a hard sphere mixture for all values of r_1, r_2, and ρ_1, whereas Figs. 3.3 & 3.11 show that the sign of γ varies with PEG molecular weight. Therefore a hard sphere model cannot account for the experimentally observed variation of the cloud point on polymer concentration, but the virial coefficients measured from light scattering can do so qualitatively.

The combined effect of varying the protein and polymer concentrations on the cloud point temperature is now investigated. The variation of $\lim_{c_2 \to 0} \partial \mathrm{T_{cloud}}/\partial c_2$ with lysozyme concentration measured experimentally and predicted by Eq.(3.3) is shown in Fig. 3.12. Experimentally, $\lim_{c_2 \to 0} \partial \mathrm{T_{cloud}}/\partial c_2$ is nearly independent of lysozyme concentration. This suggests that the physical considerations that determine $\lim_{c_2 \to 0} \partial \mathrm{T_{cloud}}/\partial c_2$ are similar at high and low concentrations. The virial coefficients measured with light scattering predict the much larger variation for the spinodal temperature depicted by the lines in Fig. 3.12, especially for the lysozyme/PEG1k mixtures. The data for the cloud point temperature variation agree with the predicted dependence at the lowest protein concentration, but increasingly diverge as the protein concentration increases. We attribute this to the failure of a virial expansion to describe the free energy of protein/polymer mixtures at high protein concentrations. Therefore Fig. 3.12 demonstrates the need for a more complete thermodynamic model to describe lysozyme/PEG mixtures at all concentrations.

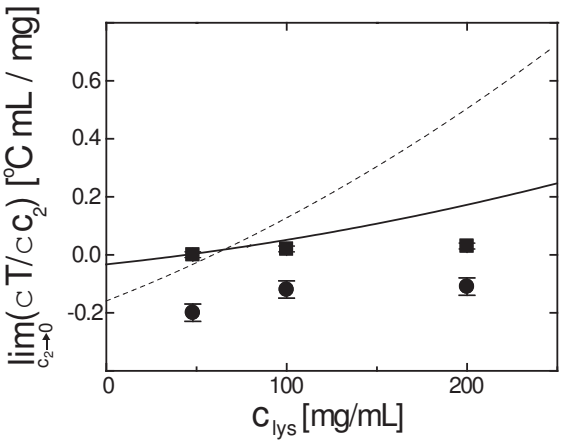

Figure 3.12: The dilute limit of the polymer dependence of the protein spinodal and binodal temperature is plotted vs. protein concentration for lysozyme/PEG mixtures in the phosphate buffer. The symbols depict $\lim_{c_2 \to 0} \partial T_{\rm cloud}/\partial c_2$ as measured from Fig.3.3, where the filled circles (•) correspond to PEG1k and the filled squares (■) correspond to PEG8k. The lines come from using the cross virial coefficients displayed in Table 3.4 in Eq.(3.2) to calculate $\lim_{c_2 \to 0} \partial T_{\rm spinodal}/\partial c_2$ as a function of c_1, where the dashed line corresponds to PEG1k and the solid line to PEG8k.

3.6 Conclusion

Adding low molecular weight PEG depresses T_{cloud} whereas high molecular weight PEG raises T_{cloud}. This observation cannot be accounted for solely by the depletion attraction. Lysozyme/PEG interactions were characterized by virial coefficients obtained from light scattering experiments. It is demonstrated that the free energy must include third virial terms to qualitatively explain the data presented in this chapter. Depletion models predict that adding PEG induces an attraction between lysozyme molecules whereas light scattering revealed the opposite: PEG induces repulsion between lysozyme molecules. The measured mixed virial coefficients are smaller than those predicted for an equivalent hard sphere mixture and are consistent with attractions between lysozyme and PEG. Therefore, a complete model of the phase behavior and light scattering of lysozyme/PEG mixtures must account for both the entropic depletion effect and an energetic attraction between protein and polymer. The measured virial coefficients, combined with thermodynamic theory, predict the observed behavior of the cloud point demonstrating the consistency of these two independent sets of experiments and that measured interactions from virial coefficients can be used to predict the collective phase behavior in these protein/polymer mixtures.

Chapter 4

Light Scattering from PDC/PEG Mixtures

4.1 Introduction

As mentioned in Section 2.1, the second virial coefficient of protein solutions, as a probe of protein interactions, has generated a great deal of interest since George & Wilson [5] reported a correlation between protein crystallisability and the second virial coefficient known as the crystallization slot. Is there a similar crystallization slot for membrane protein detergent complexes (PDCs)? The answer is unclear in part because far fewer membrane proteins have been crystallized than soluble proteins and only a limited number of studies have been performed to quantify membrane protein interactions in crystallization conditions.

Proteins often crystallize in the presence of additive solutes, such as precipitating polymers. Such precipitants modify protein interactions and therefore the virial coefficients, but it is still possible to speak of an *effective* protein second virial coefficient which describes protein, or PDC, interactions in solution as discussed in Section 3.2.3. However, care must be taken in obtaining the effective virial coefficient

from experimental data on solutions containing multiple distinct solute species. Light scattering is a common technique for measuring virial coefficients of protein solutions and in the case of multicomponent solutions of interest here one must consider the scattering from all components. Therefore simply subtracting the scattering from additive solutes is not correct, and in fact doing so yields the *apparent* virial coefficient, which in general is not the same as the effective virial coefficient. The distinction between the apparent and effective virial coefficients is described in detail below. Static light scattering has previously been used to measure the *apparent* second virial coefficients of protein/detergent complexes (PDCs) composed of OmpF porin associated with a binary detergent mixture as a function of added poly(ethylene glycol) (PEG) concentration [59]. This work showed that the apparent OmpF PDC second virial coefficient in crystallization conditions falls in roughly the same crystallization slot found for soluble proteins and that the apparent second virial coefficient of OmpF porin PDCs decreases as a function of added PEG concentration, although it did not address the distinction between apparent and effective virial coefficients.

In addition to static light scattering, dynamic light scattering, neutron scattering, NMR and chromatographic studies have been carried out to investigate the interactions between PDCs in solution and whether or not attractive PDC interactions and PDC aggregation are observed prior to crystallization. Neutron scattering studies on the reaction centers from *Rhodobacter sphaeroides* R-26 associated with the detergents lauryl-dimethylamine-N-oxide (LDAO) or *n*-octyl-β-glucoside (OG) [60] found that although the addition of PEG to a PDC solution induces crystallization, it does not lead to aggregation prior to crystallization. Tanaka *et al.* [61] performed dynamic light scattering studies of cytochrome bc_1 complex associated with sucrose monolaurate and found evidence that the addition of PEG induces attraction between bc_1 PDCs in crystallization conditions.

Detergents are needed to solubilize membrane proteins in aqueous solvents

due to the hydrophobic nature of the proteins' transmembrane domains. Therefore, PDC interactions should reflect the interactions between the detergent moieties in PDCs. Noting this, Rosenbusch [62] suggested that PDC crystallization should be favored in conditions where the detergent micellar interactions are attractive, which occurs when the detergent moieties alone show a phase transition, and therefore that PDC crystallization conditions could be pre-screened by investigating the solubilizing detergent interactions. Studies of OmpF porin [59, 63] show that its crystallization occurs near a detergent phase transition in conditions where the detergent micelle interactions are attractive. On the other hand cytochrome bc_1 complex crystallized although no phase transition of the detergent was observed in the PDC crystallization conditions [61]. Recently Berger *et al.* [64] used self-interaction chromatography and cloud point studies to demonstrate that bacteriorhodopsin/octyl-β-glucoside PDC interactions become more attractive as the detergent phase transition is approached and more generally that detergent micellar interactions and structure significantly influence PDC interactions. More data on different PDC systems is necessary to better understand the influence of detergents on PDC interactions.

The putative Cl^- channel protein, CLC-ec1, was first expressed and purified by Maduke *et al.* [65]. CLC-ec1 was crystallized in two-dimensions by Mindell *et al.* [66] who obtained a 6.5 Å resolution projection structure of CLC-ec1 from two-dimensional crystals. Single channel electrophysiological recordings of CLC-ec1 embedded in lipid bilayers have been obtained by Accardi *et al.* [67] who subsequently showed that CLC-ec1 functions as a H^+-Cl^- exchange transporter [68]. CLC-ec1 was crystallized in three-dimensions and its structure solved to 3.0 Å from x-ray scattering experiments by Dutzler *et al.* [69]. The CLC-ec1 crystal packing shows that crystal contacts between neighboring CLC-ec1 molecules in the crystal are made between the polar residues. Therefore, specific interactions between CLC-ec1 polar residues are important for crystallization.

In this chapter virial coefficients are measured for PDCs composed of the membrane protein, CLC-ec1, and the non-ionic detergent, n-octyl-β-maltoside (OM) to determine if CLC-ec1 falls in the crystallization slot, if the crystallizing precipitant PEG induces attractions and aggregation, and to determine the difference between the apparent and effective virial coefficients. We also investigate whether or not a detergent phase transition is associated with the crystallization of CLC-ec1 PDCs.

We treat PDC/PEG mixtures using the multicomponent virial expansion given in Eq.(1.7). The two component PDC/PEG solution may also be viewed as an effective one component PDC solution as was done in Chapter 3. Effective interactions between PDCs in solution in the presence of PEG are characterized by the effective second virial coefficient B_{11}^{eff}.

4.2 Materials & Methods

In this work CLC-ec1 was expressed and purified as described by Dutzler *et al.* [69]. The basic steps were to transform the DNA sequence encoding CLC-ec1 with a C terminal hexahistadine tag into competent cells. The transformed cells were then grown to a suitable level for expression. Protein expression was induced and cells were subsequently collected by centrifugation. The cells were disrupted by sonication in the presence of protease inhibitors, and the protein was extracted with the detergent n-decyl-β-maltopyranoside (DM). The initial protein purification was performed on a Cobalt column to which the C terminal hexahistidine tag preferentially binds. The protein was eluted from the Cobalt column with imidazole and reconcentrated. After cleavage of the hexahistidine tag by an endoprotease, the resulting product was loaded on an gel filtration column where the detergent was exchanged to n-octyl-β-maltopyranoside (OM). The resulting CLC-ec1 peak was fractionated into two aliquots corresponding to the rising and falling phase of the gel filtration elution

peak. The rising phase of this elution peak was then concentrated for use in light scattering experiments and crystallization trials. Typically 4-6 mg of pure CLC-ec1 was obtained from 6 L of bacteria culture.

DM (sol-grade) and OM (anagrade) were obtained from Anatrace. Poly(ethylene glycol) (PEG) of nominal molecular weight 400 g mol^{-1} was obtained from Sigma. The shorthand PEG400 is used to designate PEG 400 g mol^{-1}.

The protein, OM and PEG were dissolved in the published CLC-ec1 crystallization buffer [69] which consists of a (1:1) mixture of (75mM NaCl and 10mM Tris-HCl at pH 7.5 : 50 mM Na_2SO_4, 50 mM Li_2SO_4 and Tris 50mM at pH 8.5). The CLC-ec1 concentrations were measured by UV absorption at a wavelength of 280 nm using an extinction coefficient $\epsilon_{280\text{nm}} = 0.85$ mL mg^{-1} cm^{-1} calculated from the CLC-ec1 sequence [65]. The precise value of the extinction coefficient does not effect the value of β since β is a ratio of concentrations: $\beta = \frac{\partial(Kc/R)}{\partial c} = \frac{\partial(K[a\times c]/R)}{\partial[a\times c]}$

In order to verify that our light scattering experiments were performed in CLC-ec1 crystallization conditions, crystals of CLC-ec1 were grown in sitting drops at $T = 20$°C by equilibrating a 1:1 mixture of protein and reservoir solution against the reservoir. The protein solution consisted of 20mg mL^{-1} CLC-ec1 in 45mM OM, 75mM NaCl and 10mM Tris-HCl at pH 7.5. The reservoir solution consisted of 320 or 330 mg mL^{-1} PEG in 50 mM Na_2SO_4, 50 mM Li_2SO_4 and Tris 50mM at pH 8.5. As shown in Fig. 4.1 crystals were observed after one week. These were assumed to be protein crystals because control sitting drop trials without added PEG showed no crystals.

Refractive index increments were measured using a Brookhaven Instruments differential refractometer at $\lambda = 620$ nm. For PEG400 $\partial n/\partial c_{\text{PEG400}} = 1.33 \times 10^{-4}$ mL mg^{-1} independent of T for 10°C $\leq T \leq$ 40°C; for OM, $\partial n/\partial c_{\text{OM}} = 1.07 \times 10^{-4}$ mL mg^{-1}. For CLC-ec1/OM PDCs $\partial n/\partial c$ was not measured in order not to waste precious PDC sample. Instead, we set $\partial n/\partial c_{\text{PDC}} = 2 \times 10^{-4}$ mL mg^{-1}. This value

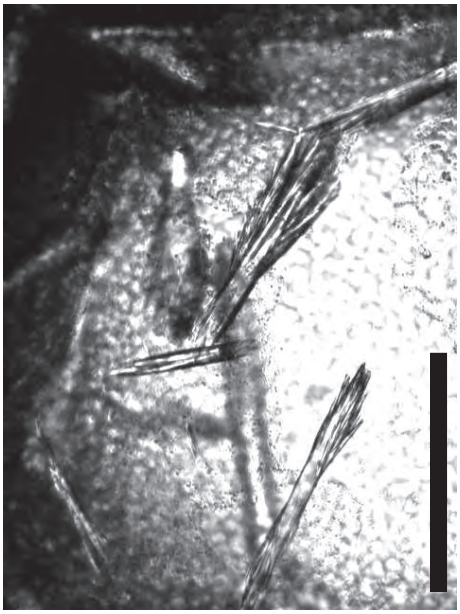

Figure 4.1: A bright field optical micrograph of CLC-ec1 crystals is shown. Crystallization trials were started approximately 12 hours after the final purification step. Crystals were observed after a one week incubation period at $T = 20^{circ}$C using reservoir PEG concentrations of 320 and 330 mg mL^{-1}.

of $\partial n/\partial c$ is a rough estimate based on the value of $\partial n/\partial c$ for soluble proteins such as lysozyme ($\partial n/\partial c_{\mathrm{lys}} = 1.85 \times 10^{-4}$) and BSA ($\partial n/\partial c_{\mathrm{BSA}} = 1.85 \times 10^{-4}$). Using $\partial n/\partial c_{\mathrm{PDC}} = 2 \times 10^{-4}$ mL mg^{-1} yields a PDC molecular weight of $M_1 = 1/\alpha = 1.11 \pm 0.04 \times 10^5$ g mol^{-1} and an apparent second virial coefficient of $B_{11} = 3 \times 10^{-4}$ mL mol/g^2. This procedure does not allow for measurement of PDC molecular weight and can only yield estimates of B_{11}. However, this procedure does not effect $\partial\alpha/\partial c_2$ or $\partial\beta/\partial c_2$, the necessary quantities for analyzing the effect of PEG on the PDC/PDC interactions.

The static and dynamic light scattering experiments (SLS & DLS) were performed as discussed in Chapter 3. DLS measures the intensity autocorrelation function $f_1(t) = \langle I(t_o)I(t_o + t)\rangle$ where $I(t)$ is the scattered intensity as a function of time at a given scattering angle. For a single diffusing solute species the intensity autocorrelation function decays exponentially $f_1(t) = ae^{-\Gamma t}$. The diffusion constant (D) is calculated from $D = \Gamma/q^2$ where q is the amplitude of the scattering vector.

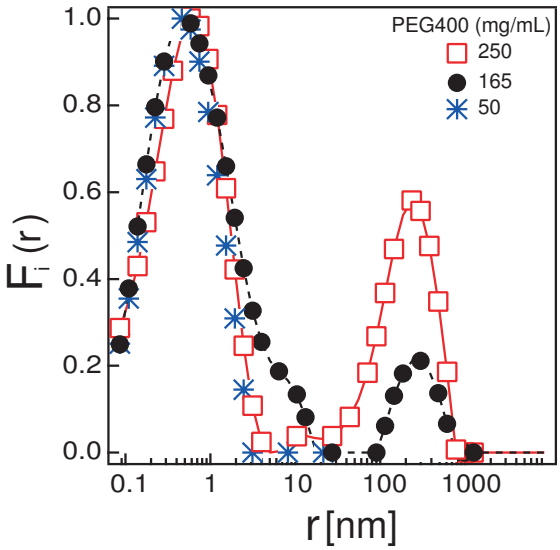

Figure 4.2: The DLS intensity weighted distribution function, Eq.(4.1), of hydrodynamic radii for PEG400 in the CLC-ec1 crystallization buffer at T=25°C is shown for different PEG400 concentrations as indicated. The slow mode corresponding to larger apparent hydrodynamic radii first appears at 165 mg mL^{-1}, which is the PEG400 concentration used to crystallize CLC-ec1.

All SLS and DLS experiments in this chapter were performed at a scattering angle of $\theta = 90°$ for which $q = 1.87 \times 10^7$ m^{-1}. When multiple diffusing species contribute to the time variation of the scattered intensity, the autocorrelation function becomes an integral of multiple exponentials:

$$f_1(t) = \int e^{-\Gamma t} F_{\mathrm{i}}(\Gamma) d\Gamma \tag{4.1}$$

where $F_{\mathrm{i}}(\Gamma)$ is the intensity weighted decay rate distribution function. The cumulant method is also used to analyze $f_1(t)$ [70]: $\ln(f_1(t)) = \ln a - \bar{\Gamma} t + \frac{\mu_2}{2} t^2 - \frac{\mu_3}{6} t^3 + \ldots$ Then the apparent diffusion constant is $\bar{D} = \bar{\Gamma}/q^2$. Hydrodynamic radii r_{H} were obtained from DLS measurements via the Stokes-Einstein relation 3.12. The intensity weighted distribution function may also be expressed in terms of the apparent hydrodynamic radii to find $F_{\mathrm{i}}(r)$. The distribution functions shown in Fig. 4.9 were calculated using the ALV-NonLin software which implements the CONTIN algorithm to calculate

$F_{\mathrm{i}}(r)$ via an inverse Laplace transform of $f_1(t)$. The mass weighted distribution function ($F_{\mathrm{m}}(r)$) is calculated from the intensity weighted distribution function assuming spherical particles by: $F_{\mathrm{m}}(r) = F_{\mathrm{i}}(r) \times r^3/(\sin(qr) - qr\cos(qr))^2$ and the number weighted distribution function is given by: $F_{\mathrm{n}}(r) = F_{\mathrm{i}}(r)/(\sin(qr) - qr\cos(qr))^2$.

4.3 Results

The critical micellar concentration (CMC) of OM was determined by SLS using the method described in ref. [59]. The scattered intensity was measured at a scattering angle of $\theta = 90°$ as a function of OM concentration. A linear fit was made to the concentration dependence of the scattering. The CMC was identified as the OM concentration where the scattered intensity was extrapolated to zero as shown in Fig. 4.4. The hydrodynamic radius (r_H) measured by DLS in the same OM samples was monitored simultaneously. r_H drops sharply to approximately zero at the CMC as shown in Fig. 4.5. The critical micellar concentration of OM in water is 9 mg mL^{-1} [71]. For OM in the CLC-ec1 crystallization buffer at $T = 20°$ C the CMC was found to be 10.4 mg mL^{-1} and 9.5 mg mL^{-1} for no added PEG and PEG400 165 mg mL^{-1} respectively. In order to measure the second virial coefficient of OM micelles, the micelle concentration is needed. The micelle concentration was taken to be the CMC subtracted from the bulk OM concentration: $c_{\mathrm{micelles}} = c_{\mathrm{OM}} - CMC$. From the cmc data, the free energy difference between a detergent molecule free in the bulk and in a micelle (ΔG) is calculated by:

$$\frac{\Delta G}{RT} = -\ln X_{\mathrm{cmc}} \tag{4.2}$$

where R is the gas constant, T is the absolute temperature and X_{cmc} is the cmc expressed as a mole fraction. As shown in Figure 4.3 panel a) the cmc of OM increases as a function of increasing PEG400 concentration whereas panel b) shows that the

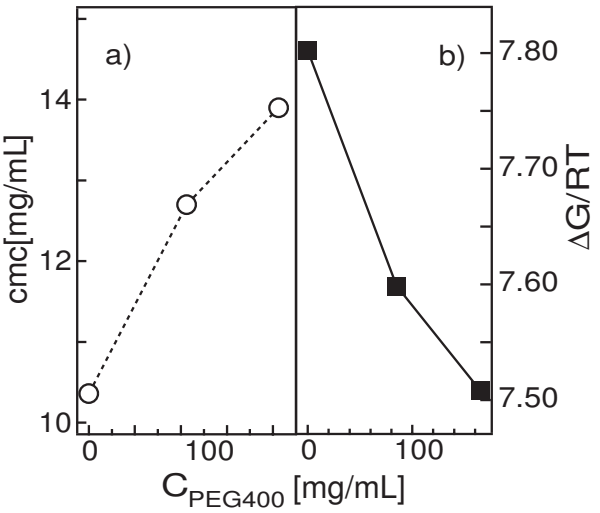

Figure 4.3: The critical micellar concentration (cmc) of OM is shown in panel a) as a function of added PEG400 concentration in the CLC-ec1 crystallization buffer at T=25°C. Panel b) displays the dimensionless free energy difference ($\Delta G/RT$) between an OM molecule in the bulk and in a micelle calculated via as a function of PEG400 concentration

free energy difference between a detergent molecule in the bulk and in a micelle decreases as PEG400 is added. These data indicate that the addition of PEG makes micelle formation less favorable and in effect destabilizes micelles with respect to free detergent monomers.

The detergent used to crystallize CLC-ec1, OM, shows no phase transition as a function of temperature up to concentrations of greater than 500 mg mL^{-1} when dissolved in pure water [71]. All detergent concentrations in this study were less than 50 mg mL^{-1}. Samples of OM at concentrations up to 50 mg mL^{-1} in the ClC-ec1 crystallization buffer with added PEG400 165 mg mL^{-1} were observed by bright field microscopy in the temperature range $2 \leq T \leq 95$ °C. No cloud point was observed indicating that no detergent liquid-liquid phase transition is associated with the crystallization conditions of CLC-ec1.

SLS experiments on PEG 400 g mol^{-1} show $M_2 = 400 \pm 100$ g mol^{-1}, $B_{22}(T = 20°\text{C}) = 0.013$ mL mol g^{-2} and $\partial B_{22}/\partial T = -1.6 \times 10^{-4}$ mL mol g^{-2} °C^{-1}. From dynamic light scattering experiments we measured $r_H = 0.7$ nm for PEG400 in the

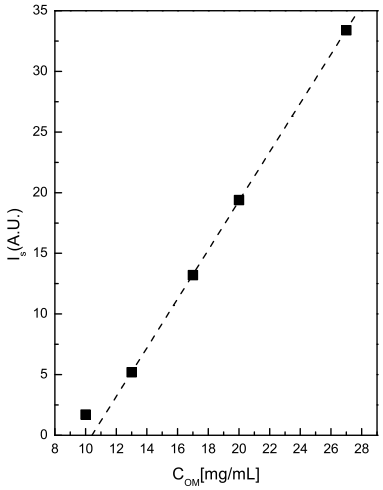

Figure 4.4: The scattered intensity I in arbitrary units at a scattering angle of ninety degrees from OM dissolved in the CLC-ec1 crystallization buffer with no added PEG at $T = 20°$ C is shown. The CMC was identified from a linear fit to I as a function of OM concentration as the extrapolated point where $I = 0$. The point shown at an OM concentration of 10 mg mL^{-1} is below the CMC and was not included in the linear fit.

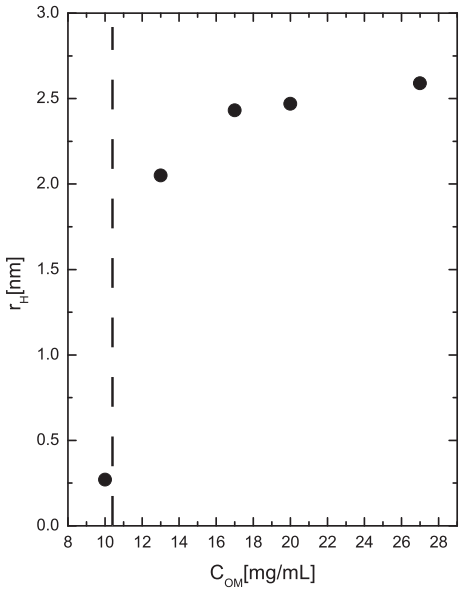

Figure 4.5: The hydrodynamic radius r_H of OM micelles in the crystallization buffer with no added PEG at $T = 20°$ C is shown. The CMC found from Fig. 4.4 and is shown as the dashed line.

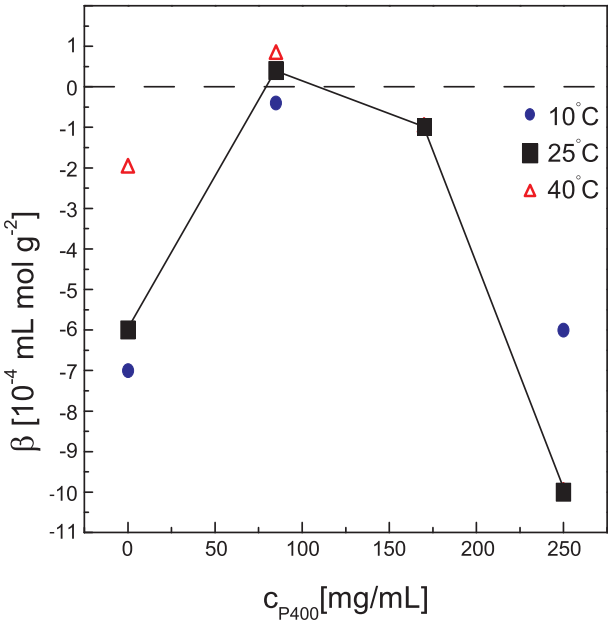

Figure 4.6: β for OM micelles is shown as a function of both temperature and PEG 400 g/mol concentration as indicated. β displays a non-linear dependence on PEG concentration.

dilute limit in the CLC-ec1 crystallization buffer. At PEG400 concentrations greater than 160 mg mL^{-1} a second, slower decaying mode appears in the DLS correlation function data, which is shown in Figure 4.2. The dependence of β for OM micelles on PEG concentration and temperature is shown in Figure 4.6. β does not vary linearly with PEG concentration indicating that Eq.(3.6) does not accurately capture the light scattering from these mixtures. The OM micelles' hydrodynamic radius as a function of PEG concentration shows a marked increase at $c_{\mathrm{P400}} = 250$ mg/mL in Figure 4.7 panel b) indicating that the OM micelles expand. At the same time, however, α shows a marked increase indicating that the OM micelles' molecular weight decreases as the micelles become less tightly associated at high added PEG concentration.

In order to determine whether or not the crystallization of CLC-ec1 occurs in the crystallization slot, the light scattering parameters α and β were measured for CLC-ec1 PDCs as shown in Figure 4.8. The values of α and β for CLC-ec1/OM PDCs are given in Table 4.1 with and without added PEG400 showing that $\beta > 0$

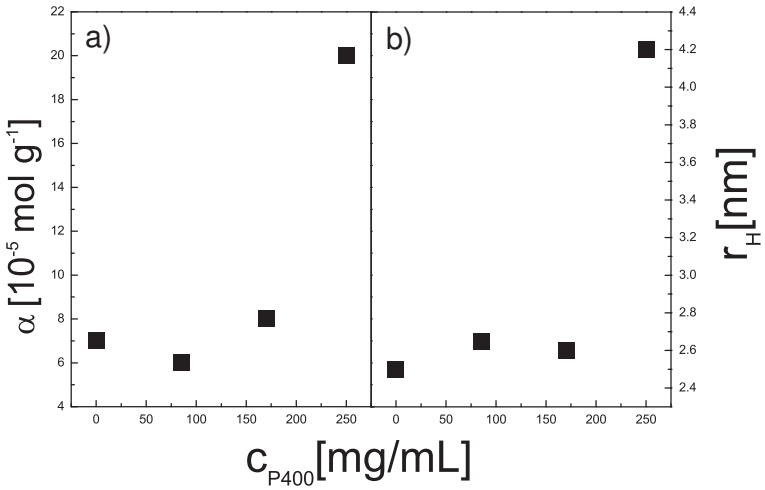

Figure 4.7: The PEG400 concentration c_{P400} dependence of α (panel a)) and r_H (panel b)) obtained from light scattering experiments are shown for OM micelles. Both show non-linear dependence on PEG concentration indicating the destabilization of OM micelles at high PEG concentration.

c_{P400} [mg/mL]	α [10^{-6}mol/g]	β [10^{-4}mL mol/g^2]
0	9	3
165	3	2

Table 4.1: α and β determined by light scattering for CLC-ec1/OM protein/detergent complexes at $T = 25°$C are shown without any added P400 and in the presence of P400 at crystallization conditions. Cross-virial coefficients were determined from these values using Eqs.(3.8,3.9).

and that β is essentially unchanged as PEG is added. In these measurements PEG400 was added to the PDC solution at $t = 0$. All static light scattering data was taken between $0 < t < 0.5$ hours. Since $\beta > 0$ without PEG, the PDC interactions as measured by the apparent virial coefficient are repulsive, which is expected in non-crystallizing conditions. β of just OM micelles in solution increases significantly as PEG is added in this PEG400 concentration range, while β of the PDCs remains constant as PEG is added. Therefore the apparent PDC virial coefficient, β, does not track the evolution of β for the OM micelles. For CLC-ec1/OM PDCs $\beta > 0$ in the crystallization conditions indicating that the crystallization of these PDCs occurs outside the crystallization slot found for soluble proteins and other membrane proteins.

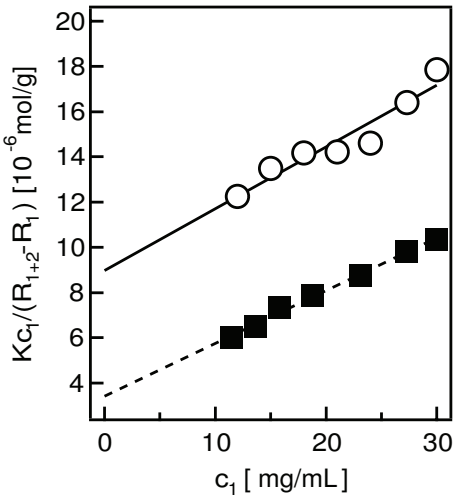

Figure 4.8: Light scattering from PDCs and PDC/PEG400 mixtures is shown. Here the subscript 1 refers to the PDCs and the subscript 2 refers to PEG400. The scattering ratio from Eq.(3.6), $\frac{Kc_1}{R_{1+2}-R_2}$, is plotted as a function of CLC-ec1 concentration, c_1 for no added PEG400 (○) and for PEG400 165 mg mL^{-1} (■). The lines are linear fits to Eq.(3.6) from which α and β listed in Table 4.1 are extracted.

Since β for CLC-ec1 PDCs remains constant, or slightly decreases as PEG is added, it would appear that PEG induces weak PDC attractions. However, β is the apparent virial coefficient and does not represent the PDC interactions. Therefore, it is necessary to calculate the variation of the effective PDC virial coefficient with PEG concentration $\partial B_{11}^{\text{eff}}/\partial c_2$ in order to conclude whether PEG induces PDC attraction or repulsion. In order to calculate $\partial B_{11}^{\text{eff}}/\partial c_2$ one must find the mixed virial coefficients B_{12} and C_{112}. From the values of α and β in Table 4.1 the mixed virial coefficient values are found from Eqs.(3.8 and 3.9): $B_{12} = -4.2 \pm 1.2 \times 10^{-3}$ mL mol g^{-2} and $C_{112} = 4.8 \pm 1.7 \times 10^{-3}$ mL^2 mol g^{-3}. For any net repulsive polymer/PDC interaction $B_{12} > 0$. The measured value of $B_{12} < 0$ indicates that the PDCs have a net attraction to PEG molecules. The values of B_{12} and C_{112} allow us to calculate the variation of the effective virial coefficient for CLC-ec1/OM complexes as a function of PEG concentration: $\partial B_{11}^{\text{eff}}/\partial c_2 = 2.9 \pm 1.3 \times 10^{-4}$ mL^2 mol g^{-3}. Since $\partial B_{11}^{\text{eff}}/\partial c_2 > 0$ the PDC interactions are becoming more repulsive as PEG is added contrary to the conclusion from considering only the apparent virial coefficient, β. The fact that

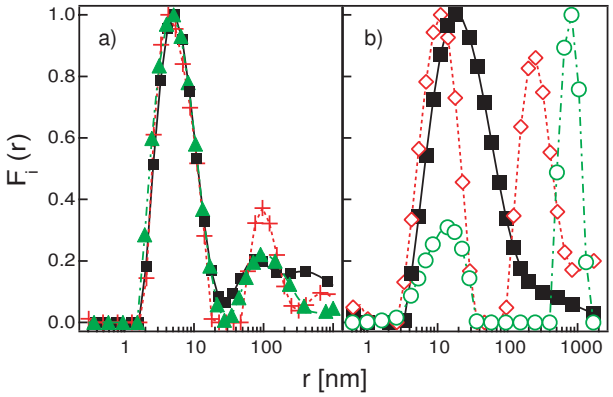

Figure 4.9: The PDC hydrodynamic radius distribution function obtained by dynamic light scattering, Eq.(4.1), for CLC-ec1/OM in the crystallization buffer at $T = 20°C$ is shown in panel a), with out added PEG, and in panel b) with PEG400 165 mg mL^{-1}, at different times. The initial time $t = 0$ is 12 hours after the final purification step when crystallization trials are started. Panel a) shows that the distribution function does not change from $t = 0$ (■) to $t = 15$ minutes (+) to t =14 hours (▲). Panel b) shows that adding PEG to a dispersion of CLC-ec1/OM PDCs induced PDC aggregation. In panel b) the decay time distribution is shown at $t = 0$ (■), $t = 2$ hours (◊) and $t = 4$ hours (○). As time progresses, the peak corresponding to large aggregates grows and the peak corresponding to individual PDCs shrinks indicating PDC aggregation.

$\partial B_{11}^{\text{eff}}/\partial c_2 > 0$ while $\partial\beta/\partial c_2 \simeq 0$ indicates the importance of using a multicomponent approach to analyze light scattering results in these mixtures.

In order to assay whether or not PDC aggregation occurs in crystallizing conditions prior to crystallization, DLS experiments were performed simultaneously with the virial coefficient measurements. The DLS results show that PEG induces PDC aggregation on the time scale of hours whereas crystallization occurs on the time scale of a number of days. The intensity weighted distribution function of hydrodynamic radii ($F_{\text{i}}(r)$) of PDC/PEG mixture is shown in Figure 4.9. The distribution function at the start of crystallization trials approximately 12 hours after the final purification step, but just before the PEG is added shows a single peak indicating single PDCs existing in solution. In the presence of PEG ($t = 0$) a peak corresponding to the PEG slow mode appears. This second peak grows with time as the first peak shrinks indicating that PDCs aggregate with added PEG. The data shown in Fig. 4.9 is weighted

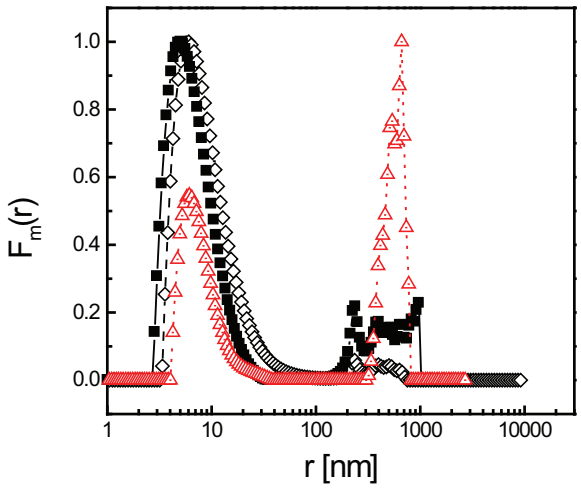

Figure 4.10: The mass weighted DLS distribution function $F_m(r)$ of CLC-ec1/OM PDCs in the crystallization conditions at $T = 20°C$ is shown as a function of time. The open diamonds correspond to $t = 0$, the filled squares to $t = 2$ hours and the triangles to $t = 4$ hours where $t = 0$ is the time of the start of crystallization trials and the addition of PEG400.

by the intensity of the scattered light and is therefore sensitive to large aggregates. Calculation of the mass weighted distribution function of the data shown in Fig. 4.9 reveals that the fraction of the total PDC mass in the aggregate peak increases to $50 \pm 3\%$ at $t = 4$ hours, although the number of PDC aggregates remains less than $1 \pm 0.5\%$ of the number of non-aggregated PDCs at $t = 4$ hours. The mass weighted DLS distribution functions are shown in Fig. 4.10 whereas the number weighted distribution functions are shown in Fig. 4.11. Therefore PEG induces the formation of a few, large PDC aggregates. With no added PEG the initial distribution function peak remains constant and no second peak appears. If the PEG concentration is removed after a period of aggregation, DLS shows that the aggregates remain intact (data not shown). Therefore the PEG induced PDC aggregation is irreversible.

It must be considered whether or not PDC aggregation in the presence of PEG can change the conclusion that PEG does not induce PDC attraction on the virial coefficient level, i.e. $\partial B_{11}^{\text{eff}}/\partial c_2 > 0$. The analysis of the virial coefficients presented above was based on the assumption that the PDC molecular weight remained

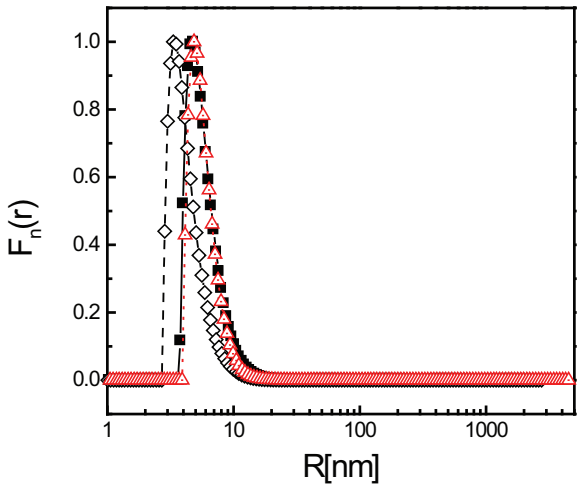

Figure 4.11: The number weighted DLS distribution function $F_n(r)$ of CLC-ec1/OM PDCs in the crystallization conditions at $T = 20°$C is shown as a function of time. The open diamonds correspond to $t = 0$, the filled squares to $t = 2$ hours and the triangles to $t = 4$ hours where $t = 0$ is the time of the start of crystallization trials and the addition of PEG400.

constant, which is clearly not the case in light of the PDC aggregation. The PDC aggregation shown in Fig. 4.9 means that the two component analysis of light scattering data presented above is not strictly applicable. However, the static light scattering data was measured between $0 < t < 0.5$ hours. At $t = 0.5$ hours the DLS data are consistent with an approximately 30% increase in the PDC molecular weight. If we assume such an increase in the PDC molecular weight along with the data in Table 4.1, we can use Eqs.(3.8,3.9) to calculate $\partial B_{11}^{\rm eff}/\partial c_2$. A 30% change in the PDC molecular weight leads to $\partial B_{11}^{\rm eff}/\partial c_2 = 2.8 \pm 0.8 \times 10^{-3}$ mL^2 mol g^{-3}. Alternatively, if we ask what increase in PDC molecular weight would be necessary to yield $\partial B_{11}^{\rm eff}/\partial c_2 = 0$, we find that the PDC molecular weight would have to increase by a factor of 2.6, which is inconsistent with the DLS data. Therefore, the amount of aggregation consistent with the DLS data does not change the qualitative conclusion from the static light scattering data that PEG does not induce PDC attraction.

The light scattering experiments on PDCs, therefore, result in two apparently contradictory conclusions: one, that PEG does not induce PDC attraction as mea-

sured by virial coefficients and two, that PEG causes PDC aggregation as measured by DLS. There are several explanations to rationalize this result. Firstly, the large aggregates strongly scatter in the forward direction and contribute weakly to scattering at ninety degrees where the measurements were made. Thus we are not sensitive to virial coefficients of the aggregates. Secondly, results from virial coefficient calculations on soluble proteins [72] showed that negative second virial coefficient values are caused mainly by specific interactions between complementary surfaces at close distances. If a few, strong CLC-ec1 interactions cause irreversible aggregation, these interactions would not contribute to the measured virial coefficient values, which reflect equilibrium properties. In light of this and our light scattering results, a qualitative hypothesis about the effect of PEG on CLC-ec1/OM PDCs can be made. PEG causes PDCs to aggregate irreversibly, possibly by destabilizing the detergent moieties on the PDCs thereby allowing short distance specific complementary PDC interactions to occu. The fact that PEG destabilizes the OM micelles supports this hypothesis that the dominant effect of PEG on PDCs is on the detergent moieties. In this picture, some PDCs remain unaggregated in solution with net repulsive interactions which is why the virial coefficients do not track the attraction associated with aggregation and subsequent crystallization. The PDC aggregates may then serve as crystal nuclei although the crystal growth process itself has not been investigated here.

4.4 Conclusion

Protein detergent complexes (PDCs) composed of CLC-ec1 and a non-ionic detergent, OM, were studied with static and dynamic light scattering experiments in conditions which yielded CLC-ec1 crystals. The apparent second virial coefficient of these PDCs in their crystallization conditions does not fall in the crystallization slot found for sol-

uble proteins. No phase transition of the detergent micelles was associated with PDC crystallization. Calculation of the effective interactions between PDCs shows that the addition of PEG400 induce repulsion, rather than attraction between non-aggregated PDCs. However, PEG was found to destabilize detergent micelle formation and to induce CLC-ec1 PDC aggregation prior to crystal growth.

Chapter 5

On the Mechanisms of Granular Rod Vortex Formation

5.1 Introduction

Driven granular materials form a variety of patterns and display a host of dynamic instabilities [73, 74, 75]. Many experimental studies of granular materials have focused on spherical or grain-like particles such as glass beads, sand and metal powders. Recently, a number of studies of anisometric granular materials have expanded the gamut of observed behaviors and generated interest in understanding the differences between the behavior of spherical and anisometric particles. As discussed in Section 1.1.3 and Chapter 6, Philipse [15] studied random granular rod packings and found that the aspect ratio controls the packing fraction. Villaruel *et al.* [76] investigated the packing of short rods in a narrow container and found that the walls induce vertical alignment and subsequently a layered packing. Stokely *et al.* [77] studied piles granular rods confined to two dimensions showing that jamming leads to voids on many length scales. As discussed in Chapter 6, random packings of granular ellipsoids were investigated by Donev *et al.* [78] who showed that ellipsoids can pack

to higher filling fractions than spheres and that such packings of ellipsoids have higher average co-ordination than sphere packings. Compaction of granular rods in very narrow containers was studied by Lumay & Vandewalle [79] who showed that the packing fraction of rods has a minimum for containers whose size is equal to the rod length and that long rods align along container walls much like spaghetti in a pasta box. The dynamic patterns formed by vertically vibrated single layers of rods in wide containers were studied by Blair *et al.* [80] who observed that rods spontaneously align vertically and undergo vortex motion. Blair *et al.* mapped the phase diagram of vertical alignment and vortex formation for aspect ratio twelve rods as a function of excitation strength and rod filling fraction. They measured the fraction of vertically oriented rods as a function of time, mapped out the velocity field of rods in a vortex and measured the phase diagram of rods for one aspect ratio as a function of excitation strength and rod filling fraction. A void filling mechanism for the spontaneous vertical alignment of rods was proposed by Blair *et al.* in which small voids can be filled by vertically aligned rods whereas large voids can be filled only by horizontally aligned rods. Blair *et al.* noted that if the initial number of voids decreases with void size, as it does in two-dimensions [77], then rods will spontaneously align vertically as a function of time filling the small voids. Following Blair *et al.*'s study of vortices Volfson *et al.* [81] performed detailed investigations of the motion of tilted rods in an annulus and found that the friction between a tilted rod and the driving plate leads to the vortex motion. In this chapter experimental investigations of the crucial role of rod geometry and material properties of the rods on vertical alignment and vortex formation are made.

5.2 Materials & Methods

Experiments were performed in a square container with 9.1 cm side lengths and a circular container with a 6 cm diameter. The ratio of container size (l_{cont}) to rod length (L) ratio was l_{cont}/L=30 for $L/D = 4$ rods and was l_{cont}/L=4 for $L/D = 48$ rods. D is the rod diameter. Granular rods were cut from round aluminum wire whose density is $\rho_{\text{Al}} = 2.6$ g mL^{-1} and nylon fishing line (Berkeley) whose density is $\rho_{\text{nylon}} = 1.25$ g mL^{-1}. A Schleuniger (RC 3250) cable cutter cut the wire into pieces of well defined length L. The measured polydispersity in length was $\Delta L/L \leq 1\%$. The rods were vertically excited by an electromagnetic shaker. A schematic of the experimental apparatus is depicted in Fig. 5.1. A key control parameter is the aspect ratio of the rods L/D. Another control parameter is the dimensionless filling fraction of rods $\phi = N/N_{\text{max}}$ where N is the number of rods in the container and N_{max} is the number of rods corresponding to one layer of triangularly packed, vertically aligned rods. For a cylindrical container $N_{\text{max}} = (\pi/\sqrt{12})(l_{\text{cont}}/D)^2$. An accelerometer (Analog Devices) measured the vertical acceleration of the container as a function of time. We denote the dimensionless acceleration as $\Gamma(t) = a(t)/g$ where g is the acceleration of gravity. The maximum downward acceleration is labelled as Γ_{max}

5.3 Results

We find that for $L/D < 4$ vertical alignment does not occur at any ϕ. For $L/D \geq 4$ we find that rods spontaneously align vertically. We tested alignment up to $L/D = 48$. Vortex formation occurs for all $L/D \geq 5$. No long lived vortices were observed for $L/D = 4$ and we were unable to determine whether or not transient vortices form at the highest densities for $L/D = 4$. The minimum rod packing fraction needed for vertical alignment is denoted by ϕ_{min}. Figure 5.3 shows that ϕ_{min} decreases as a power law with increasing L/D. This dependence was best fit by: $\phi_{\text{min}}(L/D) =$

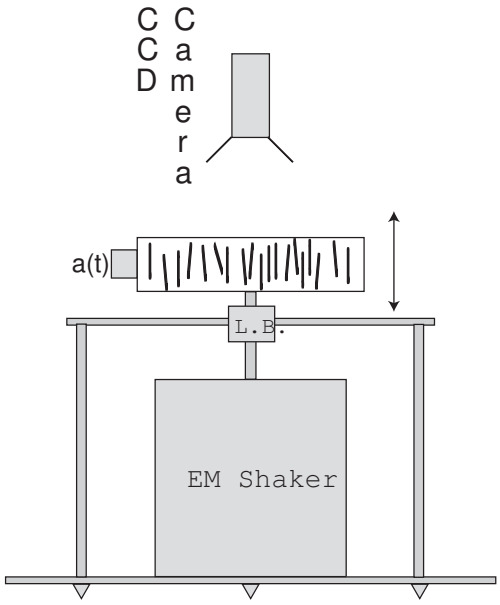

Figure 5.1: A schematic of the electromagnetic shaker used to vertically vibrate granular rods is shown. a(t) represents the accelerometer which measures the vertical acceleration as a function of time. L.B. represents a rigid linear bearing (Nippon Bearing) used to eliminate horizontal motion of the shaft connecting the shaker to the sample holder.

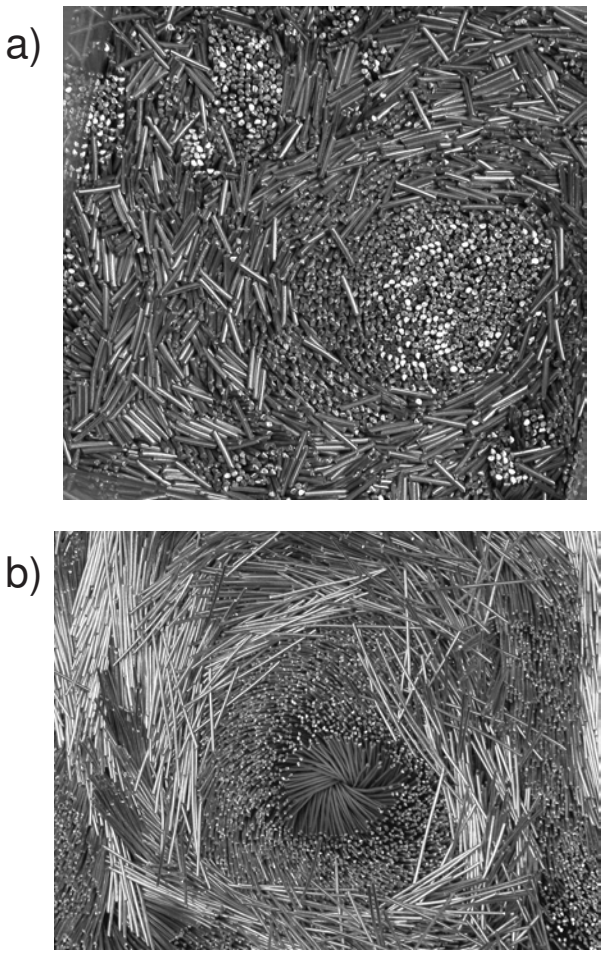

Figure 5.2: Pictures of vortices and vertically aligned rods for $L/D = 7$ at $\phi = 0.63$ in panel a) and for $L/D = 36$ at $\phi = 0.32$ in panel b).

$(L/D - 3)^{-1/3}$. We find no dependence of $\phi_{\min}$ on container size for two aspect ratios. The data points shown in Fig. 5.3 at $L/D = 6$ and 12 for two container sizes l_{cont}/L=10 and 15 showed the same $\phi_{\min}$ within experimental error demonstrating that $\phi_{\min}$ does not depend on l_{cont}/L when the container size is large enough. We expect $\phi_{\min}$ to depend on container size for small containers. Note that we find $\phi_{\min} = 0.48$ for $L/D = 12$ at $\Gamma_{\max} = 4$ whereas Blair *et al.* [80] found $\phi_{\min} = 0.35$ for the same L/D and Γ with oxidized copper rods. We attribute this to the difference between the friction coefficients of the aluminum rods in our experiments and the copper rods used by Blair *et al.*

All the rods we tested and those used by Blair *et al.* (copper, aluminum and

nylon) vertically align and form vortices but the rod packing fraction at which vertical alignment and vortex formation occur depend on the specific rod material. We performed experiments on $L/D = 12$ rods cut from nylon fishing line. We purposefully did not control for static charge and found that highly charged nylon $L/D = 12$ rods vertically aligned and formed vortices only at $\phi_{\min} = 0.8$, a higher value than for rods cut from aluminum or copper rods. However, the addition of bronze powder (Acupowder grade 61A) reduced the minimum packing fraction for vertical alignment for nylon rods to $\phi_{\min} = 0.6$. Therefore, friction between rods affects $\phi_{\min}$ in that decreasing the coefficient of friction between rods lowers $\phi_{\min}$. Additionally, we investigated vertical alignment in two binary rod mixtures of $L/D = 8$ and 16 and $L/D = 8$ and 24 rods. In these mixtures rods vertically align and form vortices and stay mixed. Blair *et al.* [80] showed that vertical alignment and vortex formation for $L/D = 12$ rods occurs in a narrow region of the Γ vs. ϕ phase space. The results presented in this chapter show that vertical alignment and vortex formation occur over a wide range of rod aspect ratios and rod properties.

Vertical vibration experiments were repeated using discrete vertical excitations, taps, in place of continuous vibration, shaking, to test whether or not continuous rod motion is necessary for vertical alignment and vortex formation. Accelerometer traces are shown in Fig. 5.4 for shaking in panel a) and tapping in panel b). Tapping was implemented using a single period of a sine wave followed by approximately thirty periods of no excitation. During the period of no excitation, all granular rods come to complete rest. After coming to rest, the rods are accelerated by the subsequent tap. We found that tapping induces vertical alignment of granular rods for the same values of L/D as for shaking. However, no vortex formation was observed when tapping. Tapping led to significantly more heaping and convection of the rods than shaking. However, it is unclear why this is so. Heaping is when the rods preferentially pile up on one side of the container. It was observed that heaping occurs even when

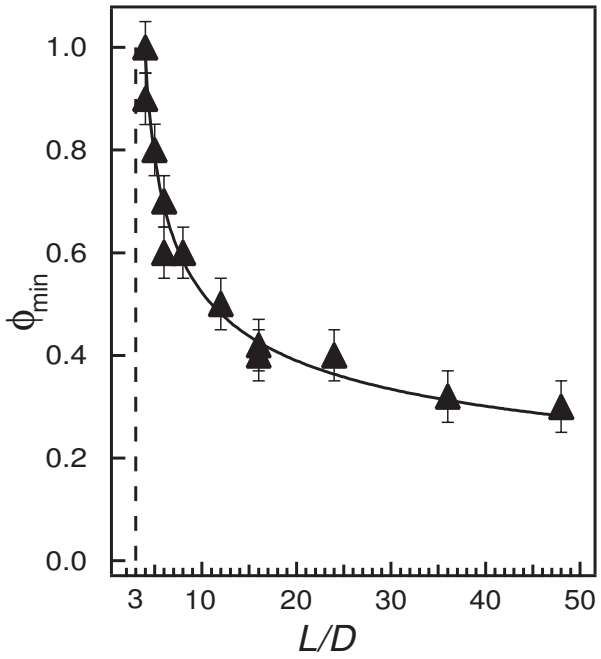

Figure 5.3: The minimum packing fraction needed for vertical alignment of granular rods $\phi_{\min}$ is plotted as a function of rod aspect ratio L/D. Rods were vertically vibrated at 50 Hz with $\Gamma_{\max} = 4$. The filled symbols indicate our experimental data and the solid line is the function: $\phi_{\min} = (L/D - 3)^{-1/3}$

the container is unlevelled so that movement to the heaped side is uphill. The term convection refers to situations where convection rolls form in the rod samples. In convection rods move primarily along these convection rolls. Small and transient regions containing approximately 10 rods appear which qualitatively resemble vortices when tapping but heaping and convection destroy these regions before they form fully developed vortices. We therefore conclude that the specific dynamics of vertical excitation do not affect the spontaneous vertical alignment of granular rods, but that competing affects do not allow vortex formation.

It was observed that tapping prepares samples of rods for vortex formation. Tapping aligns the rods vertically. If the form of excitation is subsequently changed from tapping to shaking we observe that the time between the initiation of shaking and vortex formation decreases significantly compared to when shaking is used with an initially unaligned rod sample. We therefore conclude that the specific dynamics of

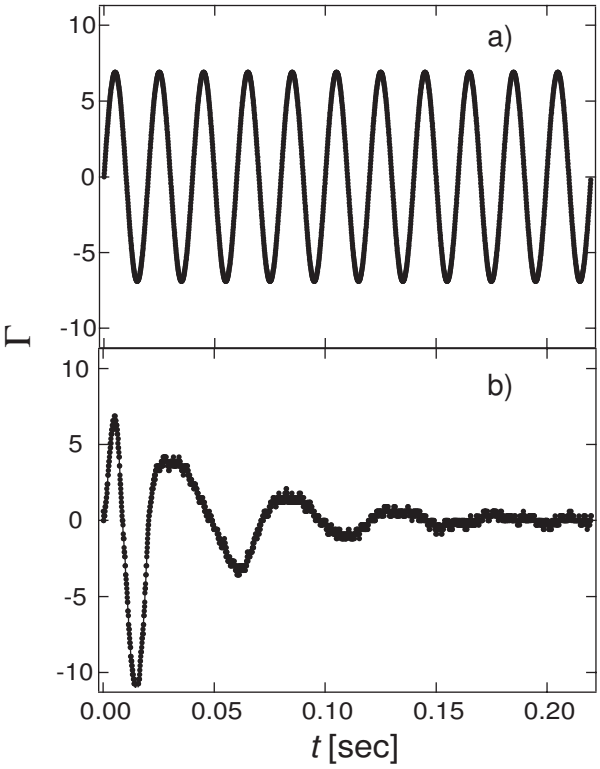

Figure 5.4: Accelerometer traces of the normalized acceleration as a function of time ($\Gamma(t)$) are shown for continuous shaking in panel a) and tapping in panel b).

vertical excitation do not affect the spontaneous vertical alignment of granular rods.

Air pressure can have a significant effect on driven granular systems [75, 82] which are many grain sizes deep. Experiments on size segregation in driven systems of spherical grains by Möbius *et al.* [75] show that the interstitial air between grains can play a large role due to the high pressures which are developed when grains impact the container and compact. In order to investigate whether or not air pressure has an effect on vortex formation, we repeated the experiments for $L/D = 12$ rods in the circular container after evacuating the container to a final air pressure of approximately 6 torr. Since all these experiments were performed on single layers of rods, we expect the interstitial air to play a much less significant role than for dense samples which are many layers thick. The lowered air pressure did not effect the vertical alignment of rods or the formation of vortices as expected.

5.4 Conclusion

Dynamic vortex formation and vertical alignment in single layers of granular rods were studied as a functions of rod aspect ratio, rod packing fraction and rod material. A minimum rod aspect ratio of $L/D = 4$ was found to be necessary for vortex formation and the minimum rod packing fraction needed for vertical alignment was found to decrease as a function of increasing rod aspect ratio. Vertical alignment and vortex formation were found to occur with rods of different densities, friction coefficients and charges. Air pressure was found not to effect vortex formation or vertical alignment. Additionally, it was found that continuous vibration was needed for vortex formation, but rods vertically align when all rods are allowed to come to rest between vertical excitations. Therefore, rods' geometry is shown to strongly influence the collective dynamic behaviors of spontaneous alignment and vortex formation whereas the specific nature of the rods' surfaces plays a secondary role.

Chapter 6

On the Co-ordination of Granular Rods

6.1 Introduction

In any random packing, the number of touching neighbors per particle, or the co-ordination number is an important quantity because contacts between particles provide the necessary mechanical constraints to ensure a stable pile. In this chapter the average co-ordination number for random packings of rods is measured as a function of the rod aspect ratio. A statistical theory of granular rods is needed in order to relate the co-ordination number to the collective behavior of the packing. The random contact model discussed in Section 1.1.3 provides this theoretical framework. The co-ordination number measurements along with measurements of the collective behavior of granular rod packings are used to evaluate the validity of the random contact model.

The average co-ordination number for a given pile is:

$$\langle z \rangle = \frac{\sum_z n_z z}{\sum_z n_z} \tag{6.1}$$

where n_z is the number of rods with z neighbors. The fraction of rods which have a given co-ordination number is $\gamma_z = n_z / \sum_z n_z$ so that the normalization condition $\sum_z \gamma_z = 1$ is met. γ_z as a function of z is the co-ordination number distribution function.

In an isostatic pile the number of constraints, or contacts per particle, equals the number of force and torque balance equations [83]. For an isostatic packing of frictionless spheres in d dimensions the number of contacts equals the number of force balance equations $\langle z \rangle = 2d$. For frictional spheres each contact determines two equations so that $\langle z \rangle = d + 1$ [84]. This result holds for frictional particles of any shape so that in 3 dimensions, the isostatic frictional limit yields $\langle z_f^{\text{iso}} \rangle = 4$ [85] although there is some debate about whether or not this argument is strictly valid for non-spherical particles [78] . For frictionless rods in 3 dimensions: $\langle z_n^{\text{rod-iso}} \rangle / 2 = 3 + 2$ so that $\langle z_n^{\text{rod-iso}} \rangle = 10$.

Bernal & Mason [86] measured $\langle z^{\text{sph}} \rangle = 6.4$ for a random packing of spheres. Their result for $\langle z^{\text{sph}}$ is close to the isostatic limit for frictionless spheres. Their method was to pour spheres into a container, pour paint into the container, drain the paint, allow the pile to dry and then count the number of spots on each sphere without any paint. Such spots represent touching neighbors. This is a tedious process. More than forty years later Donev *et al.* [78] made the subsequent experimental measurement of $\langle z^{\text{M\&M's}} \rangle = 9.8$ using Bernal & Mason's method on oblate ellipsoids with an aspect ratio of 2 (M&M's Candies [87]), which is near the isostatic limit for frictionless spheroids. Note that neither Bernal & Mason [86] nor Donev *et al.* [78] controlled for or varied friction experimentally. If piles of granular cylinders behave similarly to spheres and ellipsoids in approaching the isostatic limit then one expects $\langle z \rangle \sim 10$ independent of rod aspect ratio.

Donev *et al.* [78] also performed frictionless simulations of random packings of ellipsoids and showed that $\langle z \rangle$ has a minimum for spheres and increases sharply as

spheres are deformed into ellipsoids. Their simulations demonstrate that $\langle z \rangle \sim 10$ for maximally jammed random [88] packings of frictionless prolate and oblate ellipsoids at an aspect ratio of approximately two where the aspect ratio of an ellipsoid is defined as the ratio of its major to minor axes. Their simulation results show that although the symmetry of particles changes abruptly as the aspect ratio is changed from unity (spheres), the average contact number changes smoothly as a function of aspect ratio. The curvature of the contact number as a function of aspect ratio is not well understood.

Simulations of granular rods in two dimensions [77] show that $\langle z \rangle$ decreases as the rod aspect ratio increases towards an asymptotic value of $\langle z^{2d} \rangle = 3.2$. Philipse & Verberkmoes presented a frictionless and purely geometric argument for random packings of rods in three dimensions and calculated a lower bound of $\langle z \rangle = 5$ [89]. Williams & Philipse [90] performed frictionless monte carlo simulations of random rod packings in three dimensions and found that $\langle z \rangle$ decreased towards the frictional isostatic limit with increasing rod aspect ratio, which is opposite to our experimental measurements.

As mentioned in Section 1.1.3, Philipse [15] presented experimental data on compacted piles of granular rods showing that the product of the pile's volume fraction (ϕ) and the ratio of the rod's length (L) to the rod's diameter (D) is a constant $\phi \times (L/D) = c$, for long, thin rods ($L/D > 20$) meaning that low volume fractions can be achieved experimentally ($\phi \approx 0.06$ for $L/D = 96$). As discussed in Section 1.1.3 Philipse [15] showed that the random contact model, described in Section 1.1.3, predicts this scaling. In this chapter the RCM is experimentally tested by measuring $\langle z \rangle$, L/D and ϕ.

6.2 Materials & Methods

Compaction experiments were performed to measure ϕ as a function of L/D by pouring rods into a container and then compacting the pile by vertical excitation of the container with a single period of a 50 Hz sine wave at a maximum acceleration of five times gravity. The excitation was repeated at a rate of 1 Hz for 10^3 excitations. Cut pieces of tinned buss wire with diameters ranging from 0.25 mm to 1.4 mm were used for compaction experiments and for the co-ordination number experiment with $L/D = 3$. A Schleuniger RC 3250 cable cutter cut spools of round wire to make the rods. These wire pieces have $\Delta L/L = 1\%$ polydispersity in length. Each experiment was repeated three times and the volume fraction was taken to be the average of the three trials. A quasi-steady state was reached after typically 500-1000 excitations but further compaction was not systematically investigated. The evolution of the piles' volume fraction as a function of number of excitations is shown in Fig. 6.1. Note that the rods in these piles never aligned vertically in a layered packing as did the $L/D = 3$ rods in the experiments of Villaruel *et al* [76] who showed that typically 10^4 excitations were needed to align short rods after compaction of randomly oriented piles. Long rods form highly jammed piles in which local particle rearrangements are constrained. Rods in the bulk of such piles do not rearrange when the pile is vertically vibrated. Of course, even large aspect ratio rods will flow align when poured into very small containers as do pieces of spaghetti in a thin box [79]. The volume fraction of the compacted piles scales as $\phi_{\text{comp}}(L/D) = 5.4 \pm 0.3$ as shown in Fig. 6.3, which is consistent with previous results [15], and for uncompacted piles as $\phi_{\text{uncomp}}(L/D) = 4.2 \pm 0.2$ as shown in Fig. 6.2.

In order to measure $\langle z \rangle$ for random rod packings we followed Bernal & Mason's method. Wooden toothpicks and bamboo skewers with circular cross-sections were used as the granular rods in piles for which $\langle z \rangle$ was measured. The toothpicks measure 0.2 cm in diameter and 6.5 cm in length with pointed ends. The bamboo

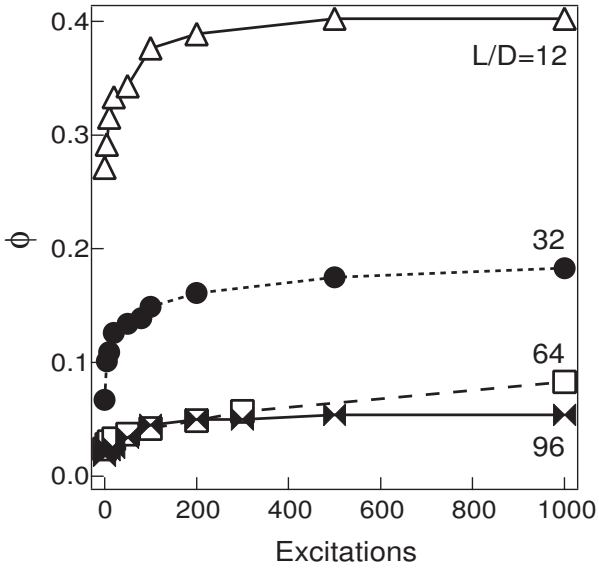

Figure 6.1: The volume fraction ϕ of piles of granular rods is shown as a function of the number of vertical excitations for L/D =12, 32, 64 and 96.

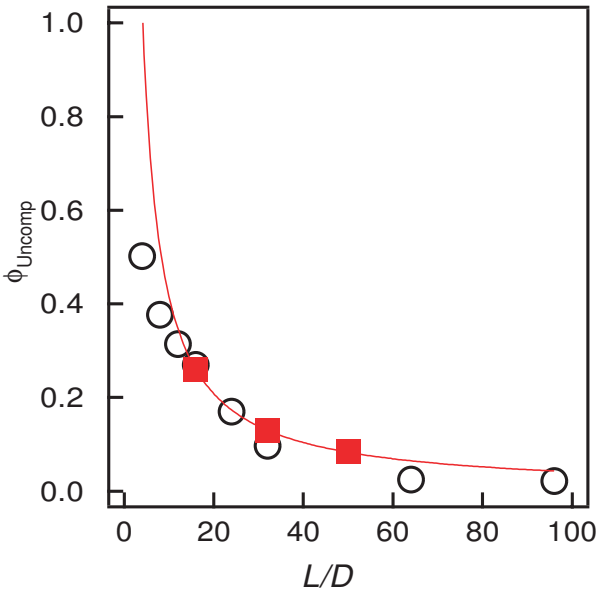

Figure 6.2: The dependence of the initally poured, uncompacted volume fraction (ϕ_{Uncomp}) as a function of L/D is shown. The data from bulk compaction experiments are shown as open circles and the data from co-ordination number experiments are shown as filled squares. The solid line is $\phi \times (L/D) = 4.2$.

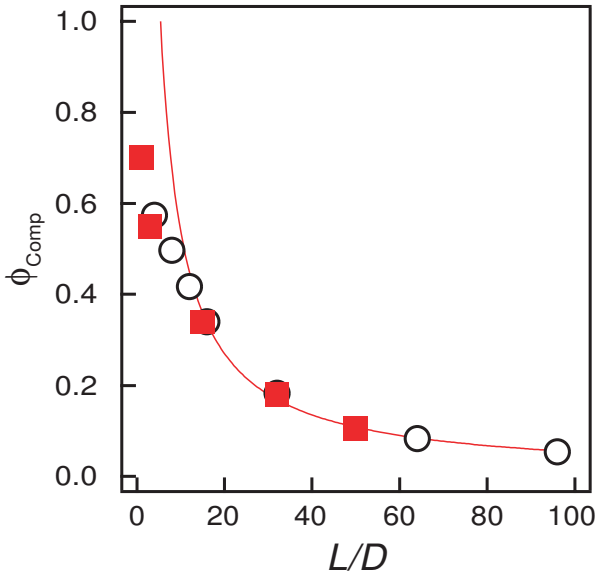

Figure 6.3: The dependence of the final, compacted volume fraction (ϕ_{Comp}) as a function of L/D is shown. The data from bulk compaction experiments are shown as open circles and the data from co-ordination number experiments are shown as filled squares. The solid line is $\phi \times (L/D) = 5.4$.

skewers measured 0.26 cm in diameter and were cut to 4 and 13 cm lengths to provide L/D=15 and 50 rods. The measured polydispersity in the toothpicks' length was approximately 2% and 3% for the bamboo skewers. We used Jujube candies [91] as L/D=1 rods. Jujubes approximate the shape of right cylinders of L/D=1. The polydispersity of Jujubes is $\Delta L/L = 20\%$ and $\Delta D/D = 10\%$. This large polydispersity leads to more contacts on average than for a monodisperse pile. Aluminum disks of 1.27 cm diameter were used as rods of aspect ratio $L/D = 0.4$. It must be noted that the compacted pile of disks displayed local parallel orientational ordering although the entire pile was isotropic [92]. 17% of disks aligned parallel to their neighbors in chains of 2-5 particles forming extended contacts across the circular faces of the disks. An extended contact between disk faces was counted as three contacts in the co-ordination number distribution. The fraction of chains of 2, 3, 4, and 5 particles was 0.74, 0.21, 0.03 and 0.02 respectively, showing that the vast majority of chains were made up of two or three particles. No extended cylindrical edge to face contacts

were observed. These aluminum disks had polydispersity of 2% both in length and diameter.

Those rods which contacted the container walls or exposed upper surface of the pile were categorized as boundary particles and those which did not were categorized as bulk particles. The compacted pile of toothpicks used to measure $\langle z \rangle$ after removal from the container is shown in Fig. 6.4. The boundary particles are clearly aligned whereas the bulk particles appear to be randomly oriented. The measured co-ordination number distribution for this pile of toothpicks is shown in Fig. 6.5. The co-ordination number distributions are qualitatively similar for all rod aspect ratios and pile volume fractions. The center of the distribution shifts as a function of aspect ratio but the width of the distribution remains constant within experimental error. As shown in Fig. 6.5, the co-ordination number distribution for boundary particles is shifted to a lower value of $\langle z \rangle$ relative to that for bulk particles and is slightly asymmetric due to the lower limit on z. Rods which contact the boundary must have fewer contacts with other rods than rods which do not contact the boundary which explains the shift to a lower $\langle z \rangle$ value. The asymmetry in the co-ordination number distribution for boundary rods is due to the presence of a lower cutoff: no rods were observed to have $z < 2$, whereas no upper cutoff independent of L/D was observed. Table 6.1 lists the measured values of $\langle z \rangle$ for compacted and uncompacted piles of different aspect ratio rods as indicated including only the bulk rods.

6.3 Results

The average co-ordination number for random right cylinder packings increases as a function of aspect ratio from $\langle z \rangle \sim 6$ for disks of aspect ratio $L/D = 0.4$ to an asymptotic value of $\langle z \rangle \sim 10$ for rods of $L/D > 30$, as shown in Fig. 6.6, demonstrating that the predictions of previous numerical simulations are incorrect [89]. The data

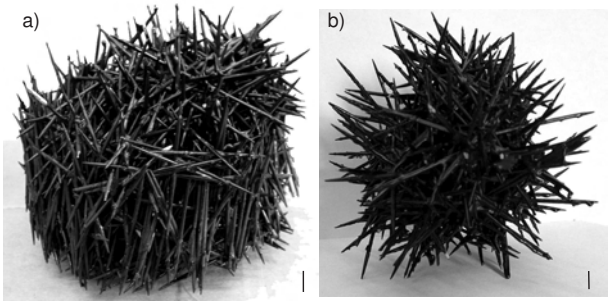

Figure 6.4: The compacted pile of $L/D = 32$ rods is shown after painting, drying and removal from the container. Panel a) shows the entire pile and panel b) shows the pile after the boundary rods have been removed. The scale bars indicate 1 cm.

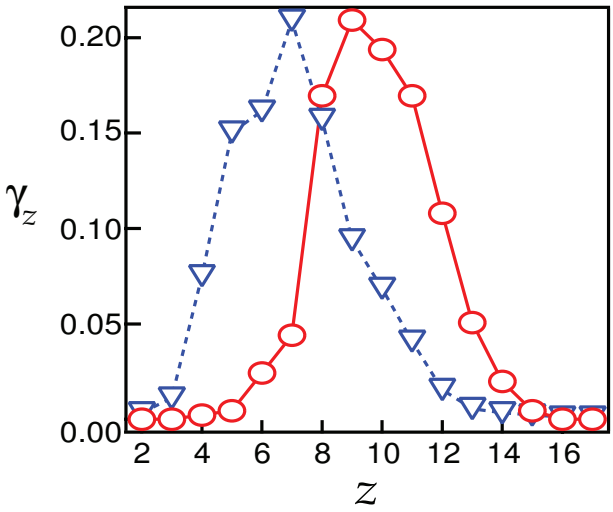

Figure 6.5: The co-ordination number distribution function of 454 bulk rods is shown as open circles alongside the distribution for the 904 boundary rods which is shown as open triangles, for a compacted pile of $L/D = 32$ rods.

on spheres [86] and on ellipsoids [78] is also displayed. As shown in Table 6.1 we find that $\langle z \rangle$ increases when a random packing of rods is compacted. For compacted piles of long aspect ratio rods the number of touching neighbors, $\langle z \rangle$, approaches the value for isostatic frictionless non-spherical particles, $\langle z_n^{\mathrm{iso}} \rangle = 10$. Fig. 6.6 shows that $\langle z \rangle$ for rods increases gradually as a function of aspect ratio without any singular behavior at $L/D = 1$, whereas Donev *et al.* [78] find that $\langle z \rangle$ is singular about $L/D = 1$. Furthermore, $\langle z \rangle$ increases approximately ten times more rapidly for ellipsoids than for cylinders. Why do packings of cylinders and ellipsoids behave so differently? Ellipsoids with aspect ratios different than one are not spherically symmetric while ellipsoids of aspect ratio equal to one are spherically symmetric. Therefore the steep variation in $\langle z \rangle$ as a function of aspect ratio seen by Donev *et al.* [78] arises due to the transition from spherical to ellipsoidal symmetry. However, cylindrical particles of different aspect ratios have the same symmetry and therefore no singular behavior of $\langle z \rangle$ as a function of aspect ratio is expected for rods. It is possible that friction between our experimental cylinders also contributes to the striking difference in the dependence of $\langle z \rangle$ as a function of aspect ratio for rods and simulated frictionless ellipsoids [78]. However, Philipse [15] showed that the bulk behavior of compacted piles of granular rods does not depend on the frictional properties of the rods. This leads us to conclude that the geometrical difference between cylinders and ellipsoids is responsible for the differences in co-ordination number, not friction. Simulations which could systematically vary the friction would be able to discriminate between these two hypotheses.

If the geometry of granular cylinders dominates their behavior in compacted piles, then the RCM's prediction should hold in the long rod limit, namely that $\frac{\langle z \rangle}{\phi(V_{\mathrm{ex}}/V_{\mathrm{p}})} = 1$. The data from Table 6.1 allow us to test this quantitative prediction. In Fig. 6.10 the quantity $\frac{\langle z \rangle}{\phi(V_{\mathrm{ex}}/V_{\mathrm{p}})}$ is plotted as a function of L/D for bulk particles in compacted piles and shows that the RCM limit is approached for high aspect ratio

	$\langle z \rangle \pm 0.3$		$\phi \pm 0.04$	
L/D	uncomp	comp	uncomp	comp
0.4	-	5.7	-	0.56
1	-	6.2	-	0.70
3	-	5.7	-	0.58
15	6.5	7.0	0.26	0.34
32	7.2	9.8	0.13	0.18
50	8.3	9.8	0.08	0.10

Table 6.1: The average number of touching neighbors $\langle z \rangle$ and the volume fraction of the pile occupied by rods ϕ are listed as a function of rod aspect ratio L/D. Only the bulk rods are included. The column labelled as "uncomp" corresponds to the uncompacted random rod packings whereas the column labelled as "comp" corresponds to the compacted packings.

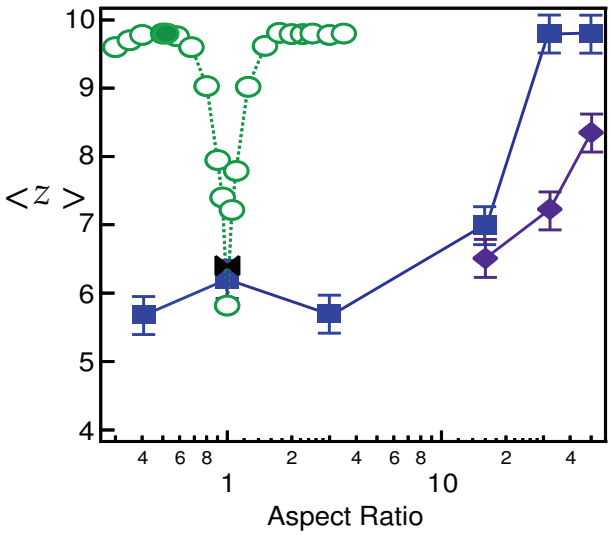

Figure 6.6: The average number of touching neighbors $\langle z \rangle$ is shown as a function of the aspect ratio (L/D) on a logarithmic scale. The squares (■) represent our compacted rod piles and the diamonds (♦) our uncompacted rod piles. The bowtie (⋈) represents spheres and is taken from Bernal & Mason [86]. The circles represent data on ellipsoids taken from Donev *et al.* [78]; the solid circle (•) is for M&Ms and the open circles (○) are from simulations.

cylindrical particles. This is further evidence that particle geometry and not friction determines piles of granular rods. The RCM assumes that contacts between rods are uncorrelated, that the excluded volume is given by the value for a pair of particles and is independent of volume fraction, and that rods are randomly oriented. Fig. 6.10 shows deviation from the RCM scaling for short rods and disks implying that some of these assumptions break down. Qualitatively, at least, the assumption of an isotropic angular distribution of rods is borne out experimentally, but we were not able to ascertain whether or not the two other assumptions were valid.

Philipse [15] noted that random packings of sufficiently high aspect ratio rods form solid-like plugs. One of the original motivations for performing the experiments described in this chapter was to test whether or not the value of the co-ordination number is related to plug formation. We observed plug formation only for compacted piles composed of rods with $L/D > 44$ as shown in Fig. 6.7. The plugs become more rigid as the aspect ratio of the rods increases. For all the plugs it was observed that rods are free to translate along their long axis. Rotation of a plug results in many rods falling out along the direction of their long axis. We measured $\langle z \rangle$ for the plug forming pile of bamboo skewers at $L/D = 50$ shown in Fig. 6.8. The data in Table 6.1 show that $\langle z \rangle$ is larger for the plug forming pile at $L/D = 50$ than for the uncompacted pile which did not form a solid-like plug. However, this value of $\langle z \rangle = 9.8$ was observed for the compacted pile at $L/D = 32$ which did not form a plug and for M & M's with aspect ratio of two [78] which shows that a certain value of $\langle z \rangle$ is necessary but not sufficient for plug formation. The co-ordination number distribution functions for the compacted piles at $L/D = 32$ and 50 are compared in Fig. 6.9. These distribution functions are almost identical with the only difference between the plug forming pile at $L/D = 50$ and the non-plug forming pile at $L/D = 32$ being the appearance of a second peak in the distribution function for $L/D = 50$. The distribution functions shown in Fig. 6.9 are similar to the

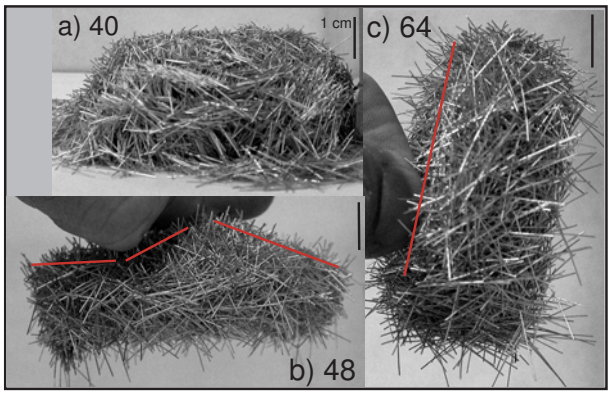

Figure 6.7: Piles of granular rods of sufficiently large aspect ratio ($L/D > 44$) form solid-like plugs as mentioned by Philipse [15]. Panel a) shows a compacted pile of $L/D = 40$ rods which does not form a plug. Panel b) shows a compacted pile of $L/D = 48$ rods which does form a plug which displays extensional rigidity. Note that in panel b) the surface normal of the plug deforms with mild applied stress as indicated by the lines. Panel c) shows a compacted pile of $L/D = 64$ rods which forms a more rigid plug than the pile of $L/D = 48$ rods. The pile of $L/D = 64$ rods can be rotated as a solid body as shown and the surface normal does not deform under mild applied stress.

distribution function measured for M&M's [78] so the appearance of this second peak in $\gamma(z)$ for $L/D = 50$ is likely not significant. These observations prove that a high value of $\langle z \rangle$ alone is not sufficient for plug formation. The mechanism leading to plug formation of granular rods remains unknown, but probably friction and flexibility of the cylinders are important physical variables.

6.4 Conclusion

In conclusion, we measured the average co-ordination number $\langle z \rangle$ for random piles of granular cylinders. $\langle z \rangle$ increases as the aspect ratio grows from $L/D = 1$. The increase in $\langle z \rangle$ was markedly slower for frictional cylinders than for simulations of frictionless ellipsoidal particles [78]. Furthermore frictional cylinders show no singular behavior at $L/D = 1$, in contrast to the frictionless simulated ellipsoids [78]. The co-ordination number of frictional cylinders reaches $\langle z \rangle \sim 10$ in the large aspect ratio

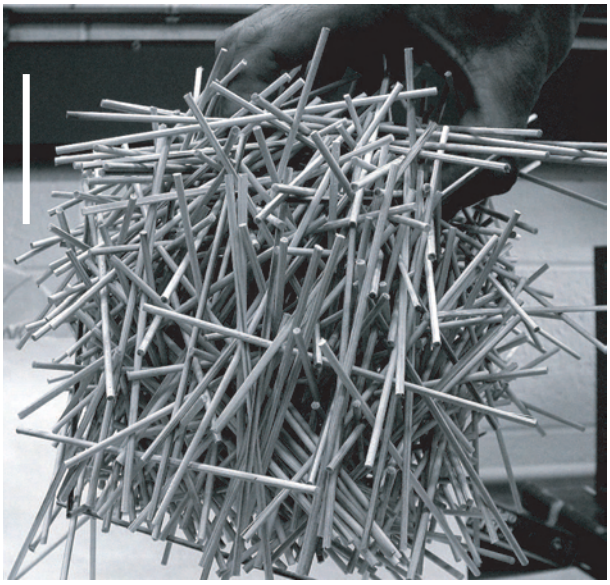

Figure 6.8: The compacted pile of $L/D = 50$ rods forms a solid plug. The pile is shown before $\langle z \rangle$ was measured. The white scale bar indicates 5cm.

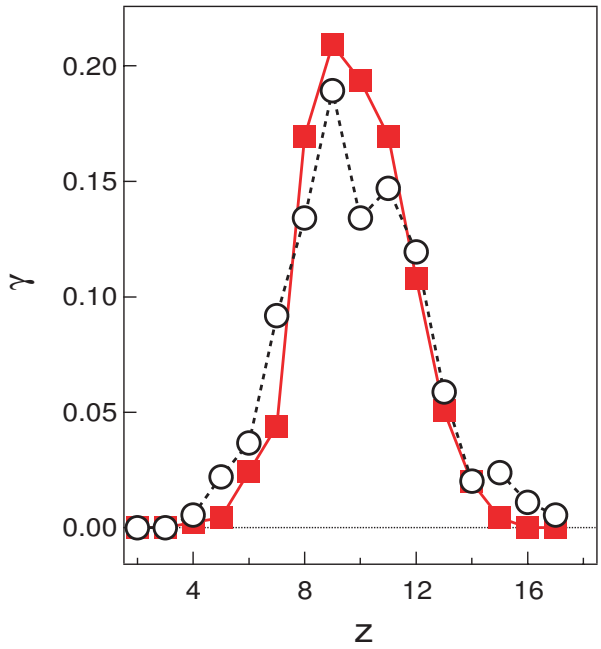

Figure 6.9: The co-ordination number distribution function $\gamma(z)$ is shown for the compacted pile of $L/D = 32$ rods (filled squares) and for the compacted, plug forming pile of $L/D = 50$ rods (open circles). As shown in Table 6.1, the measured value of $\langle z \rangle$ is the same for these two piles. Comparing their co-ordination number distribution function shows only one statistically significant difference: the appearance of a second peak in $\gamma(z)$ for $L/D = 50$. The small increase at $\gamma(z = 15)$ for $L/D = 50$ is not statistically significant.

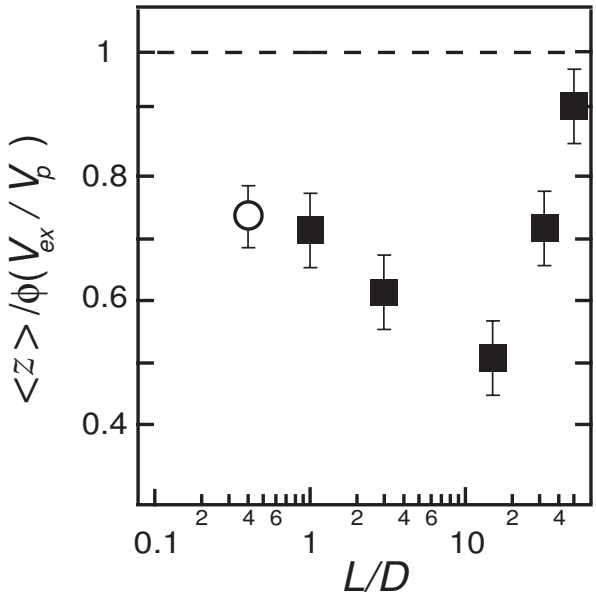

Figure 6.10: The measured data are shown along with the RCM's prediction for Eq. (1.15). The data for rods (■) and discs (○) from co-ordination number experiments is shown as a function of L/D for compacted piles. In the long rod limit the experimental data tend toward the RCM prediction; $\frac{\langle z \rangle}{\phi(V_{\rm ex}/V_{\rm p})} = 1$.

limit, $L/D \geq 30$, in compacted, random piles. Independent measurements of the volume fraction (ϕ) for these random rod packings coupled with measurements of the co-ordination number show that the random contact model is within a factor of two of experiment, and that theory and experiment approach each other in the long rod limit.

Appendix A

Expression and Purification of CLC-ec1

In this appendix the procedure used to express and purify the membrane protein CLC-ec1 is stated. These protocols were developed in Professor C. Miller's laboratory at Brandeis University following the protocols developed by R. Dutzler in Professor R. MacKinnon's laboratory at Rockefeller University. These protocols require three days to complete. The protocol for the first day should be commenced in the afternoon and requires approximately 1.5 hours. The second day's protocol begins in the morning and requires most of the day but not constant attention. The third day should be started early in the morning and requires the entire day and constant work. The third day is busy. Make sure to read through the entire protocol carefully before beginning as many of the steps are time sensitive.

A.1 Day1 - Transformation and Plating

A.1.1 Transformation

1. Transform competent D3 cells according to protocol given by the cells' provider using approximately 10ng of DNA (C terminal His tag eriC Wild Type) for 50μL of cells. Cells stored in $T = -80$°C freezer.

1b. Alternatively, use pretransformed cells stored in glycerol stocks. These cells may be obtained from members of C. Miller's laboratory.

A.1.2 Plating

1. Plate approximately 200 μL of suspended cells in LB or TB on each LB-Ampicillin agar plate. Use one plate per liter of cell growth media.

2. Incubate plates at $T = 37$°C about 12 hours, but not more than 16 hours.

A.2 Day2 - Cell Growth and Protein Expression

A.2.1 Cell Growth

1. Check the plates from Day1 to make sure that the cell colonies have grown on the agar plates. Use 1L of TB in 2L flasks for cell growth.

2. Inoculate TB by adding 2mL of Ampicillin (50 mg/mL) solution to each 1L of TB. Preheat TB flasks in $T = 37$°C incubator.

3. Scrape cell colonies from plates using TB or LB making sure to suspend cell colonies homogenously in media. Place equal amount of suspended cells into each TB flask.

4. Measure absorbance in each flask. Grow cells until the absorbance is $1.6 \leq abs \leq 1.9$. Cell growth usually takes approximately 3 hours. Note that cell growth is exponential so monitor absorbance closely near the end of the growth period.

A.2.2 Protein Expression

1. When cells have grown to the proper absorbance, induce with 1mL of αTC (0.2mg/L) and again add Ampicillin as before.

2. Induce for 3 hours. Measure absorbance again after induction. Absorbance should stay at the same level as after growth or decrease slightly indicating that cells have not grown during induction. If absorbance increases during induction it means that protein was not expressed properly because cells continued to grow instead of expressing protein.

3. After expression, spin cells down at 5000 r.p.m. for 20 minutes.

4. Discard supernatant and remove pellet from centrifugation bottles with a metal spatula into 100 mL steel beaker or just leave in centrifugation bottles. Place pellet in $T = 4°$C environment overnight.

A.3 Day3 - Protein Extraction and Purification

Stocks: 200 mM Tris-HCl pH 7.5 5M NaCl 4M Imidazole-HCl pH 7.5 pepstatin and leupeptin (0.1 mg/mL each in 95% Ethanol

Buffers: Breaking Buffer (BB) 50mL 50mM Tris-HCl / 100mM NaCl (spatula each of lysozyme and DNase I

2X Cobalt Wash Buffer (2XWB) 50mL 40mM Tris-HCl / 200mM NaCl / 20mM sol-grade decyl-maltoside (DM) pH 7.5

Cobalt Wash Buffer (WB) 50mL Dilute 2XWB with equal volume of water

Cobalt Imidazole 30mM Buffer (Im30) 40mL Make this from 4M Im stock ,2XWB and water

Cobalt Imidazole 400mM Buffer (Im400) 15mL Make this from 4M Im stock, 2XWB and water

FPLC Buffer (FB) 150 mL 10mM Tris-HCl / 150mM NaCl / 45mM octyl-maltoside

(high-grade, not sol-grade)

A.3.1 Extraction

1. Lift the soft pellet from the centrifuge tubes with metal spatula and place into 100 mL steel beaker which is resting on ice. Scrape and wash the remainder of the pellet off the bottle with 20mL BB.

2. Make smooth suspension of pellet with a 25mL stereological pipette and electric pipetter. Then add the remainder of the BB and the lysozyme and DNase. Record the total volume which should be about 60-70mL.

3. Sonication - high-intensity ultrasound is used to break the cell membranes. Check that the sonicator is tuned properly. Before sonication make add 4mg of PMSF protease inhibitor to 0.5mL of the pepstatin-leupeptin stock and ready it to add into the beaker during sonication. Place sonicator tip so that it stays near the bottom of the beaker without contacting the beaker. Make sure beaker is well surrounded by ice to avoid heating. Sonicate for 1 minute intervals, 5 times stopping between each interval to allow the suspension to cool completely. During the first interval add the 0.5mL of pepstatin-leupeptin-PMSF. Sonication should not cause much foam to appear but should visibly disturb the suspension's surface. If foam appears, readjust sonicator tip.

4. Weigh out sol-grade DM for 50mM final concentration in suspension. Place sonication suspension into rhomboid tubes and add the weighed out DM into these tubes.

5. Extract by gentle shaking for 2 hours. It will take a few minutes for the dry DM to fully dissolve.

A.3.2 Purification I - Cobalt Column

1. After extraction, pour the mixture into JA-20 rotor tubes (or others) and centrifuge at 16,000 r.p.m. for 45 minutes.

2. While the extraction mixture is spinning, prepare the Cobalt column: Use approximately 1mL of Cobalt chromatography slurry per liter of bacteria growth media so 6mL for a 6L preparation. Pour column by hand and flush with water. Also flush absorbance detector with water.

3. Equilibrate Cobalt column with 5-10 column volumes of WB with DM.

4. When the extraction mixture has finished the centrifugation step, pour the supernatant off which contains the protein. Discard the pellet.

5. Load the supernatant from extraction onto the Cobalt column at $\tilde{2}$mL/minute flow rate. When the entire supernatant volume is on the column, switch back to flowing WB.

6. When the brown color clears from the eluted flow, start flowing into the absorbance detector and start the chart recorder to measure the absorbance at 280nm wavelength.

7. When the absorbance settles down to a baseline value switch to Im30. Run 30-40 mL of Im30 through at a flow rate of 2mL/min. You should see a peak of nonspecific protein eluting. ClC-ec1 will remain bound to the column.

8. Now elute the CLC-ec1 by switching to Im400 and collect the peak of CLC-ec1 into a prewashed (with WB) 15mL centricon 50K cutoff centrifugal concentrator tube.

9. Centrifuge the centricon tube at 3200 rpm for 20-60min until the protein volume is reduced to $\tilde{0}$.4mL.

10. While the protein solution is concentrating flush the column and absorbance detector with water, then a 20% ethanol mixture. Leave the column apparatus in air and close off the absorbance detector with the 20% ethanol solution inside.

A.3.3 Purification II - His-tag Cleavage

Add LysC protease, 0.5U total (100μL) from aliquot in freezer. Let the protease cut for 1 hour at room temperature. Sample is now ready to load on the FPLC Superdex 200 column to separate CLC-ec1 from any remaining contaminants including the C

terminal histadine tag cleaved by the LysC protease.

A.3.4 Purification III - FPLC

1. Make sure to follow all the Miller lab protocols associated with the FPLC. Someone from the Miller lab should guide you through the FPLC usage in order to ensure proper procedures are followed.

2. Before Cobalt column step start flushing Superdex 200 column with water and then equilibrate the column with filtered and degassed FB.

3. Inject no more than 0.25mL of sample for each run. Run sample through column at a flow rate of 1mL/min

4. Main CLC-ec1 peak elutes at 11-13 mL. Collect the rising phase of the peak and the falling phase of the peak in different tubes. Use only the rising phase to ensure maximum purity.

5. Flush column according to prescribed FPLC running procedures.

6. Concentrate final, purified CLC-ec1 sample using a 50K cutoff centrifugal filter to reduce the volume to less than 0.5mL. Sample is now ready for crystallization or light scattering studies.

7. If PEG is to be added, this may be done by dialyzing overnight against a buffer containing PEG with an appropriate dialysis membrane. If PEG is added light scattering studies must be carried out as soon as possible as PEG causes irreversible aggregation of the CLC-ec1/OM complexes.

Bibliography

[1] H. K. Onnes. *Arch. neerlandaises des Sci. exactes & nat.*, 874, 1901.

[2] The Oxford English Dictionary. *http://dictionary.oed.com/cgi/entry/50278033*. Oxford University Press, oed online edition, 1989.

[3] T. L. Hill. *An Introduction to Stastistical Thermodynamics*. Addison-Wesley, Reading, MA, 1960.

[4] F. Reif. *Fundamentals of statistical and thermal physics*. McGraw-Hill, Inc., 1965.

[5] A. George and W. W. Wilson. Predicting protein crystallization from a dilute solution property. *Acta Cryst.*, D50:361–365, 1994.

[6] J. L. Lebowitz. Exact solution of generalized Percus-Yevick equation for a mixture of hard spheres. *Phys. Rev.*, 133(4A):A895–A899, 1964.

[7] S. Asakura and F. Oosawa. Interaction between particles suspended in solutions of macromolecules. *J. Poly. Sci.*, 33:183–192, 1958.

[8] A. P. Gast, C. K. Hall, and W. B. Russell. Polymer-induced phase separations in nonaqueous colloidal suspensions. *J. Coll. Interf. Sci.*, 96:251–267, 1983.

[9] H. Mahadevan and C. K. Hall. Experimental analysis of prtoein precipitation by polyethylene glycol and comparison with theory. *Fluid Phase Eq.*, 78:297–321, 1992.

[10] E. J. Meijer and D. Frenkel. Colloids dispersed in polymer solutions. a computer simulation study. *J. Chem. Phys.*, 100(9):6873, 6887 1994.

[11] E. Eisenriegler, A. Hanke, and S. Dietrich. Polymers interacting with spherical and rodlike particles. *Phys. Rev. E*, 54(2):1134–1152, 1996.

[12] R. Tuinier, G. A. Vliegenthart, and H. N. W. Lekkerkerker. Depletion interaction between spheres immersed in a solution of ideal polymer chains. *J. Chem. Phys.*, 113(23):10768–10775, 2000.

[13] O. Annunziata, N. Asherie, A. Lomakin, J. Pande, O. Ogun, and G. B. Benedek. Effect of polythylene glycol on the liquid-liquid phase transition in aqueous protein solutions. *Proc. Nat. Acad. Sci. USA*, 99(22):14165–14170, 2002.

[14] P. G. Bolhuis, A. A. Louis, and J-P. Hansen. Influence of polymer-excluded volume on the phase-behavior of colloid-polymer mixtures. *Phys. Rev. Lett.*, 89:123802, 2002.

[15] A. P. Philipse. The random contact equation and its implications for (colloidal) rods in packigs, ruspensions, and anisotripic powders. *Langmuir*, 12:5971, 1996.

[16] L. Onsager. The effects of shape on the interaction of colloidal particles. *Ann. N.Y. Acad. Sci.*, 51:627, 1949.

[17] J. Behlke and O. Ristau. Analysis of the thermodynamic non-ideality of proteins by sedimentation equilibrium experiments. *Biophys. Chem.*, 76:13–23, 1999.

[18] Y. U. Moon, R. A. Curtis, C. O. Anderson, H. W. Blanch, and J. M. Prausnitz. Protein-protein interactions in aqueous ammonium sulfate solutions. lysozyme and bovine serum albumin (BSA). *J. Sol. Chem.*, 29(8):699–717, 2000.

[19] O. D. Velev, E. W. Kaler, and A. M. Lenhoff. Protein interactions in solution characterized by light and neutron scattering: comparison of lysozyme and chymotrypsinogen. *Biophys. J.*, 75:2682–2697, 1998.

[20] F. Bonneteé, S. Finet, and A. Tardieu. Second virial coefficient: variations with lysozyme crystallization conditions. *J. Cryst. Growth*, 196:403–414, 1999.

[21] P. M. Tessier, A. M. Lenhoff, and S. I. Sandler. Rapid measurement of protein osmotic second virial coefficients by self-interaction chromatography. *Biophys. J.*, 82:1620–1631, 2002.

[22] J. Wu and J.M. Prausnitz. Osmotic pressures of aqueous bovine serum albumin solutions at high ionic strength. *Fluid Phase Eq.*, 155:139–154, 1999.

[23] L. W. Nichol, R. J. Siezen, and D. J. Winzor. The study of multiple polymerization equilibria by glass bead exclusion chromatography with allowance for thermodynamic non-ideality effects. *Biophys. Chem.*, 9:47–55, 1978.

[24] P. R. Wills, L. W. Nichol, and R. J. Siezen. The indefinite self-association of lysozyme: consideration of composition-dependent activity coefficients. *Biophys. Chem.*, 11:71–82, 1980.

[25] W. W. Yau, J. J. Kirkland, and D. D. Bly. *Modern size-exclusion chromatography.* J. Wiley, N.Y., 1979.

[26] M. Sadao and H. G. Barth. *Size exclusion chromatography.* Springer, 1999.

[27] I. Novák and D. Berek. Structural inhomogeneities in wide-pore silica gels. *J. Chrom. A*, 665:33–36, 1994.

[28] M. Muschol and F. Rosenberger. Interactions in undersaturated and supersaturated lysozyme solutions: Static and dynamic light scattering results. *J. Chem. Phys.*, 103(22):10424–10432, 1995.

[29] C. Gripon, L. Legrand, I. Rosenman, O. Vidal, M. C. Robert, and F. Boué. Lysozyme-lysozyme interactions in under- and super-saturated solutions: a simple relation between the second virial coefficients in H_2O and D_2O. *J. Cryst. Growth*, pages 575–584, 1997.

[30] A. M. Kulkarni, A. P. Chatterjee, K. S. Schweizer, and C. F. Zukoski. Depletion interactions in the protein limit: Effects of polymer density fluctations. *Phys. Rev. Lett.*, 83:4554, 1999.

[31] K. E. Shearwin and D. J. Winzor. Thermodynamic nonideality in macromolecular solutions. *Eur. J. Biochem*, 190:523–529, 1990.

[32] A. McPherson. *Crystallization of biological macromolecules*. Cold Spring Harbor Lab. Press, Cold Spring Harbor, NY, 1999.

[33] O. Galkin and P. G. Vekilov. Conrol of protein crystal nucleation around the metastable liquid-liquid phase boundary. *Proc. Nat. Acad. Sci. USA*, 97(12):6277–6281, 2000.

[34] M. Muschol and F. Rosenberger. Liquid-liquid phase separation in supersaturated lysozyme solutions and associated precipitate formation/crystallization. *J. Chem. Phys.*, 107(6):1953–1962, 1997.

[35] J. A. Thomson, P. Schurtenberger, G. M. Thurston, and G. B. Benedek. Binary liquid phase separation and critical phenomena in a protein/water solution. *Proc. Nat. Acad. Sci. USA*, 84:7079–7083, 1987.

[36] O. Annunziata, O. Ogun, and G. B. Benedek. Observation of liquid-liquid phase separation for eye lens γS-crystallin. *Proc. Nat. Acad. Sci. USA*, 100(3):970–974, 2003.

[37] P. R. ten Wolde and D. Frenkel. Enhancement of protein crystal nucleation by critical density fluctuations. *Science*, 277:1975–1978, 1997.

[38] M L. Broide, T M. Tominc, and M D. Saxowsky. Using phase transitions to investigate the effect of salts on protein interactions. *Phys. Rev. E*, 53:6325, 1996.

[39] K. Devanand and J. C. Selser. Asymptotoic behavior and long-range interactions in aqueous solutions of poly(ethylene oxide). *Macromolecules*, 24:5943–5947, 1991.

[40] I. Teraoka. *Polymer Solutions*. John Wiley & Sons, N.Y., 2002.

[41] J. J. Grigsby, H. W. Blanch, and J. M. Prausnitz. Diffusivities of lysozyme in aqueous MgCl2 solutions from dynamic light scattering data: Effect of protein and salt concentrations. *J. Phys. Chem. B*, 104:3645–3650, 2000.

[42] I. Prigogine and R. Defay. *Chemical Thermodynamics*. Longman, London, 1954.

[43] J. T. Edsall, H. Edelhoch, R. Lontie, and P. R. Morrison. Light scattering in solutions of serum albumin: effects of charge and ionic strength. *J. Am. Chem. Soc.*, 472:4641–4656, 1950.

[44] R. S. King, H. W. Blanch, and J. M. Prausnitz. Molecular thermodynamics of aqueous two-phase systems for bioseparations. *AIChE J.*, 34(10):1585–1593, 1988.

[45] S. Finet and A. Tardieu. α-crystallin interaction forces studies by small angle X-ray scattering and numerical simulations. *J. Cryst. Growth*, 232:40–49, 2001.

[46] D. H. Atha and K. C. Ingham. Mechanism of precipitation of proteins by polyethylene glycols. *J. Bio. Chem.*, 256(23):12108–12117, 1981.

[47] J. G. Kirkwood and R. J. Goldberg. Light scattering arising from composition fluctuations in multi-component systems. *J. Chem. Phys.*, 18:54–57, 1950.

[48] A. Vrij. Influence of polydispersity on the light scattering of concentrated dispersions of spherical particles. *Chem. Phys. Lett.*, 53(1):144–147, 1978.

[49] P. Tong, T. A. Witten, J. S. Huang, and L. J. Fetters. Interactions in mixtures of colloid and polymer. *J. Phys. France*, 51:2813–2827, 1990.

[50] D. Vivarès, L. Belloni, A. Tardieu, and F. Bonneté. Catching the PEG-induced attractive interaction between proteins. *Eur. Phys. J. E*, 9:15–25, 2002.

[51] A. Vrij. Polymers at interfaces and the interactions in colloidal dispersions. *Pure & Appl. Chem.*, 48:471–483, 1976.

[52] H. De Hek and A. Vrij. Interactions in mixtures of colloidal silica and polystyrene molecules in cyclohexane. 1. Phase separations. *J. Colloid Interface Sci.*, 84:409, 1981.

[53] B. J. Bern and A. Pecora. *Dynamic Light Scattering*. Wiley, NY, 1976.

[54] W. Kaye and A. J. Havlik. Low angle laser light scattering-absolute calibration. *Applied Optics*, 12(3):541–550, 1973.

[55] V. G. Taratuta, A. Holschbach, G. M. Thurston, D. Blankschtein, and G. B. Benedek. Liquid-liquid phase separation of aqueous lysozyme solutions: effects of pH and salt identity. *J. Phys. Chem.*, 94:2140–2144, 1990.

[56] R. Bhat and S. N. Timasheff. Steric exclusion is the principal source of the preferential hydration of proteins in the presence of polyethylene glycols. *Prot. Sci.*, 1:1133–1143, 1992.

[57] N. L. Abbott, D. Blankschtein, and T. A. Hatton. Protein partitioning in two-phase aqueous polymer systems. 3. A neutron scattering investigation of the polymer solution structure and protein-polymer interactions. *Macromolecules*, 25:3932–3941, 1992.

[58] N. L. Abbott, D. Blankschtein, and T. A. Hatton. Protein partitioning in two-phase aqueous polymer systems. 1. Novel physical pictures and a scaling-thermodynamic formulation. *Macromolecules*, 24:4334–4348, 1991.

[59] C. Hitscherich Jr., J. Kaplan, M. Allaman, J. Wiencek, and P. J. Loll. Static light scattering studies of OmpF porin: implications for integral membrane protein crystallization. *Protein Sci.*, 9:1559–1566, 2000.

[60] P. A. Marone, P. Thiyagarajan, A. M. Wagner, and D. M. Tiede. The association state of a detergent-solubilized membrane protein measured during crystal nucleation and growth by small-angle neutron scattering. *J. Cryst. Growth*, 191:811–819, 1998.

[61] S. Tanaka, M. Ataka, K. Onuma, and T. Kubota. Rationalization of membrane protein crystallization with polyethylene glycol using a simple depletion model. *Biophys. J.*, 84:3299–3306, 2003.

[62] J. P. Rosenbusch. The critical role of detergents in the crystallization of membrane proteins. *J. Struc. Biol.*, 104:134–138, 1990.

[63] C. Hitscherich Jr., V. Aseyev, J. Wiencek, and P. J. Loll. Effects of PEG on detergent micelles: implications for the crystallization of integral membrane proteins. *Acta Cryst.*, D57:1020–1029, 2001.

[64] B W. Berger, C M. Gendron, C R. Robinson, E W. Kaler, and A M. Lenhoff. The role of prtoein and surfactant interactions in membrane- protein crystallization. *Acta. Cryst.*, D61:724–730, 2005.

[65] M. Maduke, D. J. Pheasant, and C. Miller. High-level expression, functional reconstitution, and quaternary structure of a prokaryotic CLC-type chloride channel. *J. Gen. Physiol.*, 114:713–722, 1999.

[66] J. A. Mindell, M. Maduke, C. Miller, and N. Grigorieff. Projection structure of a CLC-type chloride channel at 6.5 $\AA$ resolution. *Nature*, 409:219–223, 2001.

[67] A. Accardi, L. Kolmakova-Partensky, C. Williams, and C. Miller. Ionic currents mediated by a prokaryotic homologue of CLC Cl^- channels. *J. Gen. Physiol.*, 123:109–119, 2004.

[68] A. Accardi and C. Miller. Secondary active transport mediated by a prokaryotic homologue of clc cl channels. *Nature*, 427:803–807, 2004.

[69] R. Dutzler, E. B. Campbell, M. Cadene, B. T. Chait, and R. MacKinnon. X-ray structure of a CLC chloride channel at 3.0 $\AA$ reveals the molecular basis of anion selectivity. *Nature*, 415:287–294, 2002.

[70] D E. Koppel. Analysis of macromolecular polydispersity in intensity correlation spectroscopy: the method of cumulants. *J. Chem. Phys.*, 57:4814–4820, 1972.

[71] B. J. Boyd, C. J. Drummond, I. Krodkiewska, and F. Grieser. How chain length, headroup polymerization and anomeric configuration govern the thermotropic and lyotropic liquid crystalline phase behavior and the air-water interfacial adsoprtion of glucose-based surfactants. *Langmuir*, 16:7359–7467, 2000.

[72] B L. Neal, D Asthagiri, O D. Velev, A M. Lenhoff, and E W. Kaler. Why is the osmotic second virial coefficient related to protein crystallization? *J. Cryst. Growth*, 196:377–387, 1999.

[73] F. Melo, P. B. Umbanhowar, and H. L. Swinney. Hexagons, kinks, and disorder in oscillated granular layers. *Phys. Rev. Lett.*, 75:3838, 1995.

[74] S. G. K. Tennakoon and R. P. Behringer. Vertical and horizontal vibration of granular materials: coulomb friction and a novel switching state. *Phys. Rev. Lett.*, 81:794, 1998.

[75] M. E. Möbius, X. Cheng, G. S. Karczmar, S. R. Nagel, and H. M. Jaeger. Intruders in the dust: Air-driven granular size separation. *Phys. Rev. Lett.*, 93:198001, 2004.

[76] F. X. Villarruel, B. E. Lauderdale, D. M. Mueth, and H. M. Jaeger. Compaction of rods: relaxation and ordering in vibrated, anisotropic granular material. *Phys. Rev. E*, 61(6):6914–6921, 2000.

[77] K. Stokely, A. Diacou, and S. V. Franklin. Two-dimensional packing in prolate granular materials. *Phys. Rev. E*, 67:051302, 2003.

[78] A. Donev, I. Cisse, D. Sachs, E. A. Variano, F. H. Stillinger, R. Connelly, S. Torquato, and P. M. Chaikin. Improving the density of jammed disordered packings using ellipsoids. *Science*, 303:990–993, 2004.

[79] G. Lumay and N. Vandewalle. Compaction of anisotropic granular materials: experiments and simulations. *Phys. Rev. E*, 70:051314, 2004.

[80] D. L. Blair, T. Neicu, and A. Kudrolli. Vortices in vibrated granular rods. *Phys. Rev. E*, 67:031303, 2003.

[81] D. Volfson, A. Kudrolli, and L. S. Tsimring. Anisotropy-driven dynamics in vibrated granular rods. *Phys. Rev. E*, 70:051312, 2004.

[82] M. Klein, L. L. Tsai, M. S. Rosen, T. Pavlin, D. Candela, and R. L. Walsworth. Interstitial gas and density-segregation of vertically-vibrated granular media. *cond-mat/0506085*, 2005.

[83] L. E. Silbert, D. Ertas, G. S. Grest, T. C. Halsey, and D. Levine. Geometry of frictionless and frictional sphere packings. *Phys. Rev. E*, 65(3):1, 2002.

[84] S. Alexander. Amorphous solids: their structure, lattice dynamics and elasticity. *Phys. Rep.*, 296:65–236, 1998.

[85] S. F. Edwards and D. V. Grinev. Statistical mechanics of stress transmission in disordered granular arrays. *Phys. Rev. Lett.*, 82:5397–5400, 1999.

[86] J. D. Bernal and J. Mason. Co-ordination of randomly packed spheres. *Nature*, 188:910–911, 1960.

[87] M &M's Candies are a registered trademark of Mars Inc.

[88] S Torquato, T. M. Truskett, and P. G. Debenedetti. Is random close packing of spheres well defined. *Phys. Rev. Lett.*, 84:2064–2067, 2000.

[89] A. P. Philipse and A Verberkmoes. Statistical geometry of caging effects in random thin-rod structures. *Physica A*, 235:186–193, 1997.

[90] S. R. Williams and A. P. Philipse. Random packings of spheres and spherocylinders simulated by mechanical contraction. *Phys. Rev. E*, 67:051301, 2003.

[91] Jujubes are a registered trademark of The Hershey Company.

[92] J. A. C. Veerman and D Frenkel. Phase behavior of disklike hard-core mesogens. *Phys. Rev. A*, 45:5632–5648, 1992.